HIGH RESOLUTION LASER SPECTROSCOPY OF RADIOACTIVE ISOTOPES USING A RFQ COOLER-BUNCHER AT CERN-ISOLDE

A thesis submitted to the University of Manchester for the degree of Doctor of Philosophy in the Faculty of Engineering and Physical Sciences

2009

ERNESTO BATISTA MANÉ JÚNIOR

School of Physics and Astronomy

CONTENTS

LIST OF FIGURES

LIST OF TABLES

ABSTRACT

At CERN, the European Organization for Nuclear Research, radioactive nuclear beams are produced at the On-Line Isotope Mass Separator facility, ISOLDE. This facility provides a variety of exotic nuclear species for multidisciplinary experiments including nuclear physics. A gas-filled linear Paul trap was commissioned off-line and on-line and now is fully integrated at the focal plane of the high resolution separator magnets of ISOLDE. Ion beams with reduced transverse emittance and energy spread are now available for all experiments located downstream the separator beam line. This device is also able to accumulate the ion beam and release the collected sample in short bunches. Typical accumulation times are 100 ms and the released bunch width is $5-20$ μs. Such bunching capabilities has substantially increased the sensitivity of collinear laser spectroscopy with fluorescence detection by reducing the background from laser scatter by up to four orders of magnitude. The spectroscopic quadrupole moments of ^{44,46}K isotopes, as well as the ground-state spins of ^{73,76,78,79}Ga isotopes and the magnetic dipole moments and spectroscopic quadrupole moments of ^{73,75,76,77,78,79}Ga isotopes were determined for the first time. The sign of the quadrupole moment of ^{67}Ga was also unambiguously determined for the first time.

DECLARATION

No portion of the work referred to in this thesis has been submitted in support of an application for another degree or qualification of this or any other university or other institute of learning.

COPYRIGHT STATEMENT

ACKNOWLEDGEMENTS

I am profoundly indebted to Professor Jonathan Billowes for having accepted me as his student and for having given me such an inspiring and life-changing project that kept me busy for the past 4 years. Although it was hard at times, I enjoyed every little progress I made! I can see for myself that my understanding of the subject went from nothing to something. Thank you Jon for everything.

I am also grateful to Pierre Delahaye and Valentine Fedosseev, for looking after me during the year I spent at CERN, multitasking between the commissioning of ISCOOL and the shifts at RILIS. Those were wonderful times, when I met very nice people and some lasting friendships developed. A warm thanks to all of you.

I would like to thank the former and present members of the COLLAPS collaboration, especially to Deyan, Kieran and Mark, for their hard work and dedication. I did learn a lot from all of you. I wish you all the best.

Back in the UK, it was a pleasure to work with the other students of the Manchester-Birmingham laser groups: Benjamin, Bruce, Frances, Malamatenia, Katarzyna and Mareike. A special thanks goes to Paul, Bradley and David for their support. I would also like to thank Stephen Hopkins from the PSI for his invaluable teachings on non-linear optics and lasers, and Craig for the help with C++.

In Brazil, I would like to thank Professors Dr. Christiano and Dr. Teruya from UFPb, for their encouragement and support.

Last, but not least, I want to thank my family and friends, who have been giving me the necessary strength to bring this work to completion. For those on the other side of the Atlantic I can say “Valeu galera!”

Ernesto Batista Mané Júnior
Manchester, August 2009.

Para Solange,

CHAPTER 1

INTRODUCTION

1.1 Motivation

The current knowledge of nuclear structure has been mostly based on the measurements of observables belonging to stable isotopes. One of the cornerstones of nuclear theory is the nuclear shell model. Being a model, it has had remarkable success in accounting for the ground state properties of most stable nuclei. However, the recent advances in the research of exotic nuclei have highlighted new aspects of nuclear structure and nuclear dynamics, which challenge the models developed so far. Extensions of nuclear theory to explain these features require a deeper understanding of the nuclear force, and the accumulation of a robust body of experimental data, which pushes the technological frontiers on the production, separation and manipulation of radioactive beams.

Key aspects of nuclear structure

That certain numbers of protons (Z) and neutrons (N) confer an extra stability to the nucleus is a fact corroborated by experimental evidence taken from a vast number of

isotopes. For instance, trends on quantities such as the binding energies and relative abundances show discontinuities at the numbers N (or Z) $= 2, 8, 20, 28, 50, 82, 126$ [1]. For this reason, these specific N (or Z) values are called "magic numbers". These numbers make a strong case for hypothesising the existence of an underlying shell structure in the nucleus in which the nucleons occupy single-particle orbitals. The shell structure can be understood in terms of successive energy gaps between clusters of orbitals as they are filled. According to this idea, these orbitals ought to be eigenstates of the Schrödinger equation:

$$\hat{H}\Psi_k = E_k\Psi_k, \tag{1.1}$$

where $\hat{H}$ is the Hamiltonian operator of the many-body system, Ψ_k is the total wave function of protons and neutrons in a particular orbital (state) labelled by k, and E_k is the eigenvalue of the Hamiltonian operator associated with Ψ_k and describes the energy of the state k. Ignoring the Coulomb interaction between the protons inside the nucleus, and only considering the strong force between the nucleons, the Hamiltonian may be written as [2]

$$\begin{aligned} \hat{H} &= \hat{T} + \hat{V} \\ &= \sum_i \frac{\hat{\mathbf{p}}_\mathbf{i}^\mathbf{2}}{2m_i} + \sum_{i<j} \hat{V}_{ij} + \sum_{i<j<k} \hat{V}_{ijk} + \cdots, \end{aligned} \tag{1.2}$$

where m_i is the mass of each nucleon (proton or neutron) and $\{\hat{V}_{ij}, \hat{V}_{ijk} \ldots\}$ are the many-body potentials. Equation 1.2 already suggests that the nucleus is a system sub-

ject to interactions of intricate nature. Determining these interactions and how the shell gaps arise and change across the nuclear chart is a problem which lies at the core of nuclear structure theory. The first ingredient for the theory is the so-called nucleon-nucleon (NN) interaction, which corresponds to the $\hat{V}_{ij}$ term in equation 1.2. In the 1930's Yukawa made the first attempts to treat the NN interaction analytically [3]. He proposed that the interaction between the nucleons were mediated by the exchange of massive bosons (mesons $\pi, \rho \ldots$). The *meson hypothesis* was indeed for many years thought to be the fundamental theory of the nuclear force. Along these lines, phenomenological potentials were proposed in the years that followed in order to describe the existing NN scattering data. Examples of such potentials is the one proposed by Hamada and Johnston in 1962, which is of the form [4]

$$\hat{V}_{ij} = \hat{V}_C(r) + \hat{V}_T(r)\hat{S}_{ij} + \hat{V}_{LS}(r)\hat{\mathbf{L}}\cdot\hat{\mathbf{S}} + \hat{V}_{LL}(r)\hat{L}_{ij}, \tag{1.3}$$

where $V_C(r)$ is the central part; $V_T(r)$ is the tensor part; $V_{LS}(r)$ and $V_{LL}(r)$ are the linear and quadratic spin-orbit components. The analytical expressions for those parts can be found in the original paper. Modern versions of these phenomenological NN potentials include the CD-Bonn potential and Argonne AV18. Details can be found in [5]. However, the practical implementation of these NN phenomenological potentials in shell-model calculations are limited to cases with a reduced number of nucleons ($N \approx 10$). Exact and general solutions, which should also include the other many-body terms (NNN, for example) might take several years to come. This is fundamentally owing to the fact that protons and neutrons are not indivisible constituents of nucleonic

matter. They are made of quarks which interact via the exchange of gluons. The current theory which governs these processes is *quantum chromo dynamics* (QCD) [6]. Nevertheless, to date, working on the low-energy regime of QCD (< 300 MeV) in order to extract the NN interaction is too difficult a problem due to the many internal degrees of freedom of the quark-gluon system [5]. Recent lattice QCD calculations for the NN interaction have been performed by Ishii and collaborators [7] and show promising future prospects since it was the first time that such calculations produced results in agreement with the phenomenological models used to describe the NN interaction.

As mentioned in the previous paragraph, it becomes computationally difficult to use the phenomenological NN interactions with an increase in the number of nucleons in nuclear matter. Therefore, instead of trying to solve equation 1.2 from first principles, the concept of a single-particle effective interaction is introduced.

Effective interaction and spin-orbit coupling

The concept of effective interaction arises from the assumption that the nucleons move independently in an average field. In other words, it is assumed that the nucleons do not interact with each other, but are bound by an effective single-particle potential $V(\mathbf{r})$. This potential can be envisaged as the net result of all the interactions between the nucleons. The many-body terms which appear on equation 1.2 are regarded as "residual" interactions, which may or may not be treated perturbatively. The extent to which the residual interactions can be reliably treated as a perturbation will depend upon the accuracy of the effective potential, and assuring that the the many body terms have a

vanishing contribution. By introducing the single-particle potential, the Hamiltonian operator will assume the form:

$$\hat{H} = \underbrace{\sum_i \left[\frac{\hat{\mathbf{p}}_\mathbf{i}^2}{2m_i} + \hat{V}_i(\mathbf{r}) \right]}_{single-particle} + \underbrace{\sum_{i<j} \hat{V}_{ij} + \cdots - \sum_i \hat{V}_i(\mathbf{r})}_{\text{“}residual\text{”}} \tag{1.4}$$

In the late 1940's, Maria Goeppert Mayer [8, 9] and Otto Haxel *et al.* [10] were the first to independently reproduce the sequence of the "standard" magic numbers by assuming a central mean-field potential in addition to assuming a strong spin-orbit coupling. Examples of mean-field potentials include the harmonic oscillator potential, the finite square well and the more realistic Woods-Saxon potential. The latter has the form given by equation 1.5 [11],

$$V(r) = \frac{V_0}{1 + \exp\left((r - r_0)/a\right)}, \tag{1.5}$$

where V_0 is the well depth and is empirically taken as $V_0 \approx 50$ MeV [11]. The quantities r and a are the nuclear radius and the diffuseness parameter, respectively. The latter quantity, a, reflects the idea that the nucleus has a rather diffuse matter distribution. The nuclear radius and the diffuseness parameter are empirically [11] determined as $r_0 = 1.22\, A^{-1/3}$ fm and $a = 0.5$ fm. The shape of the Woods-Saxon potential can be seen in comparison with the finite square well and harmonic oscillator potentials in Figure 1.1. For a more detailed discussion of these potentials in the context of the nuclear shell model, see for example reference [12]. On the extreme left of Figure 1.2, the single-particle occupancies for the nucleons are given in terms of the harmonic

oscillator states, labelled as Nl, where N is the major oscillator quantum number and l is the orbital quantum number. Note that the states are degenerate with respect to the orbital quantum number for this choice of potential. The degeneracy of these states is lifted with the Woods-Saxon potential.

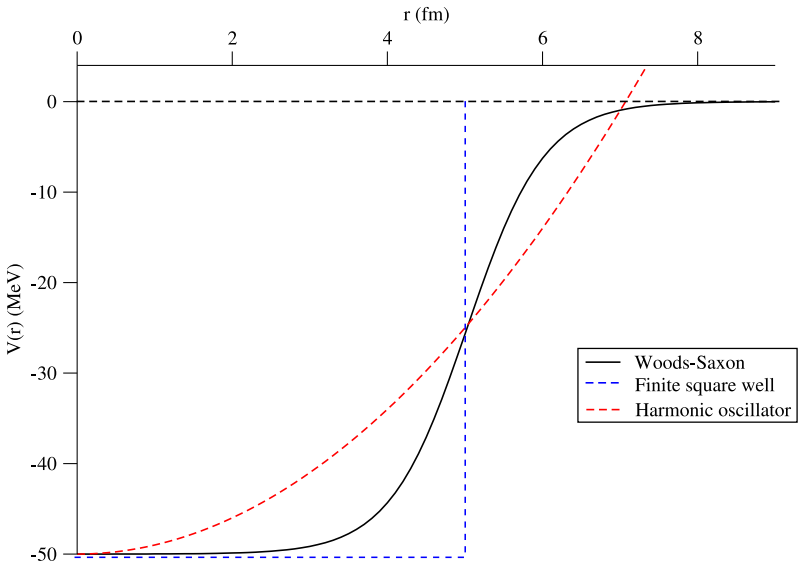

Figure 1.1: The finite square well (blue dotted line), harmonic oscillator potential (red dotted line) and the Woods-Saxon potential (black solid line). Adapted from [11].

The spin-orbit interaction has the form $V_{so}(r)\mathbf{L}\cdot\mathbf{S}$. When this term is included as a perturbation for the potential given by equation 1.5, the degeneracy of the states are further lifted. The $\mathbf{J}$ quantum number can be defined as $\mathbf{J}=\mathbf{L}+\mathbf{S}$, and the energy splitting between spin-orbit partners, ΔE, is given by

$$\Delta E = \begin{cases} -\frac{1}{2}(l+1) < V_{so} >_{Nl}, & J = L-S \\ \frac{1}{2}l < V_{so} >_{Nl}, & J = L+S. \end{cases}$$

The nuclear states are therefore labelled as Nlj. This scheme worked remarkably well to explain ground state properties of nuclei such as the spins and parities in terms of single-particle "valence" nucleons. However, over half a century has passed since the nuclear shell model became established and much more information has become available on the properties of radioactive isotopes away from the line of stability. Particularly in recent years, there has been an increasing number of experimental investigation which has been producing data pointing to radical changes in the shell structure. For instance, there is the onset of a new magic number at $N = 16$, near the neutron drip-line found by Ozawa *et al.* [13]; evidence of shell break-up at $N = 20$ for ^{32}Mg isotopes measured by Guillemaud-Mueller *et al.* [14] and Motobayashi [15] and evidence of shell break-up at $N = 8$, as discussed in [16, 17].

Spins, moments and the hyperfine structure

The data obtained from measurements of the nuclear spins and moments are extremely valuable in order to test the validity of nuclear models, as well as to help to improve the predicting power of such models in regions where experimental data is inaccessible. The most recent compilation of spins and moments of ground and excited states of radioactive isotopes measured by a variety of methods is the work of Stone [18] of 2005.

The hyperfine structure of atomic nuclei can provide model-independent, and often unambiguous information on the ground-state properties of the nucleus. In most cases observables such as the spin and moments (μ, Q_s) can be easily obtained from

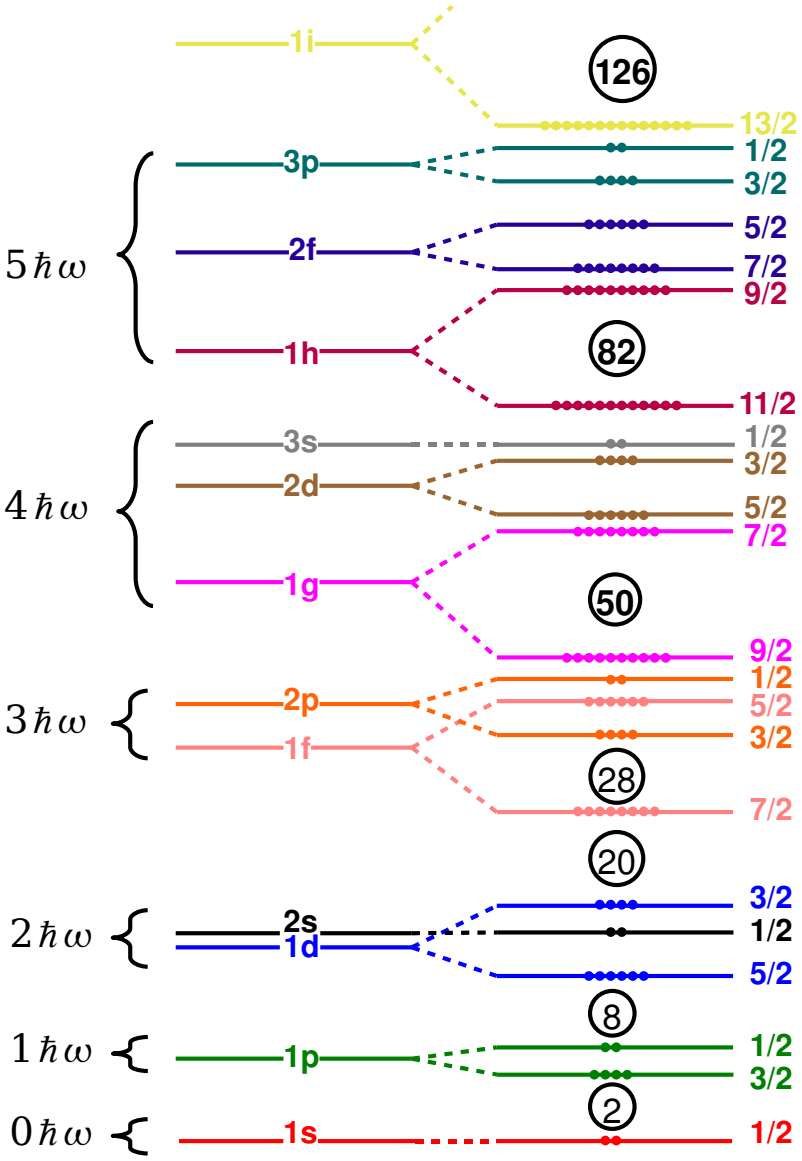

Figure 1.2: Single-particle occupancies of nucleons in a central mean-field potential with strong spin-orbit coupling. On the extreme left, the brackets indicate the levels for a pure $3D$ harmonic oscillator potential. In the middle, the occupancies for the Woods-Saxon potential. On the extreme right, the Woods-Saxon potential plus spin-orbit interaction. The numbers in the circles indicate the total accumulation of nucleons before a shell gap. Figure adapted from [1].

the data. If the nucleus is in a sufficiently long-lived excited state (with a lifetime typically greater than 1 ms), it is also possible to obtain nuclear information of that state. In addition, high-quality information on the change in mean-square charge radii is simultaneously achieved from the isotope/isomer shifts [19].

Laser spectroscopy

With the advent of tunable lasers in the 1970's, physicists have gained a sensitive and versatile tool to study the hyperfine structure of atomic spectra in the optical region. The parallel development of methods for the production and separation of radioactive ion beams culminated in the realisation of on-line laser spectroscopy studies which offered a wealth of data used to understand the structure of radioactive isotopes across the nuclear chart. Compilations of the hyperfine structure of radioactive isotopes can be found in [20, 21]. The present status of the optical measurements of nuclear observables, and including the recent gallium measurements discussed in this thesis is shown in Figure 1.3.

Nowadays, for the continual intellectual advancement of nuclear physics, it is increasingly necessary to produce exotic radioactive isotopes situated further from the line of stability. However, since the production cross sections for these isotopes become smaller, fewer are produced and with shorter lifetimes. Therefore, in order to compensate for the loss in detection sensitivity in collinear laser spectroscopy with fluorescence detection, background suppression methods are required. To this end, the use of ion traps in laser spectroscopy studies have become an attractive option.

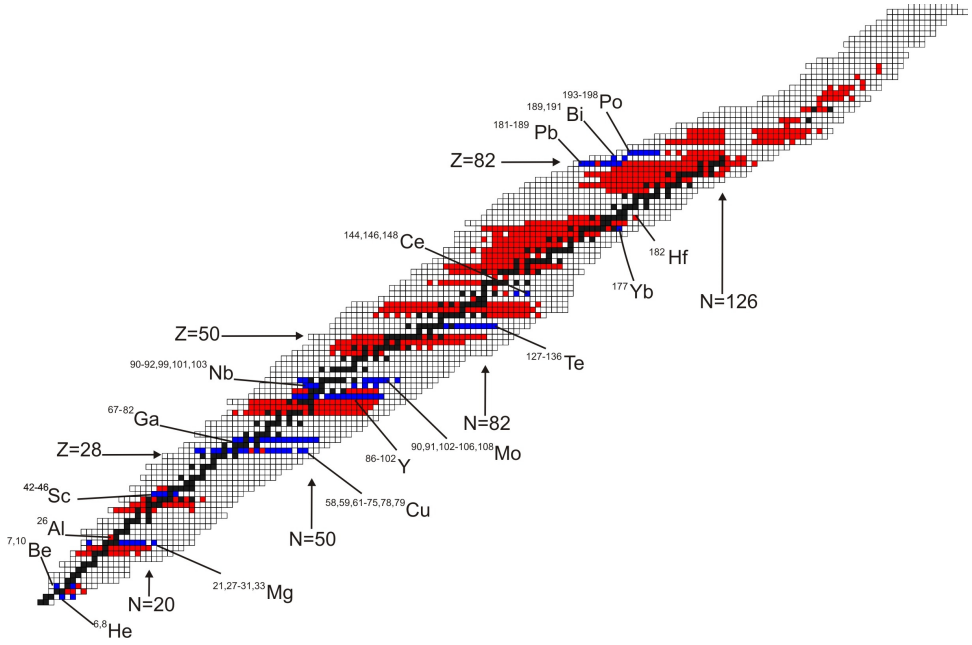

Figure 1.3: Present status of optical measurements. The black squares indicate the stable isotopes. The red squares refer to measurements made up to 2003, as detailed in Kluge and Nörtershäuser [21]. The blue squares represent the most recent update, adapted from Flanagan [22].

Ion traps

These traps were originally used for mass spectrometry [23]. Nowadays, ion traps have a much wider spectrum of applications, ranging from areas as diverse as analytical chemistry, to being an important ingredient in the development of prototypes of quantum computers [24]. For radioactive nuclear beam facilities, these devices are already part of the standard suite of beam manipulation devices. At the IGISOL facility in Finland, the pioneering application of a linear Paul trap to cool and bunch ions for laser spectroscopy, resulted in pushing the limits of fluorescence detection to radioactive beams with production rates of $\sim$ 100 ions/s and half-lives typically $\ll$ 1 s

[25].

1.2 This work

This Ph.D. research is the result of the author's contribution to the work of the collaboration between the Universities of Manchester-Birmingham and the collinear laser spectroscopy (COLLAPS) collaboration. This work builds on the doctoral work of Ivan Podadera, who designed a gas-filled RFQ cooler and buncher at ISOLDE (ISCOOL), and led the project up to the beginning of the off-line commissioning phase. The author of this thesis played an important role in the off-line and on-line commissioning of ISCOOL. With the definite installation of ISCOOL, better quality beams became readily available for the user's community using the high-resolution separator (HRS) beam line. This apparatus was used in conjunction with high resolution collinear laser spectroscopy technique for the first time for a fruitful programme of experiments on radioactive isotopes. During the on-line commissioning, radioactive ^{44,46}K ($Z = 19$) were investigated and the quadrupole moments were determined. In addition, ISCOOL allowed an extension of the current knowledge of spins and moments of neutron-rich gallium ($Z = 31$) isotopes, spanning $A = 67$ up to $A = 79$. The author was involved in all of the experiments described in this thesis and the analysis and interpretation of the results reported in this work were performed independently by the author and represent the author's own work. This thesis is organized as follows. Chapter 2 presents the basic theory of hyperfine structure of the atomic levels, Chapter 3 is about the laser spectroscopic methods used in this work. Chapter 4 introduces

the isotope separator facility at CERN, the laser spectroscopy beam line and the ISCOOL ion trap. Chapter 5 and 6 discusses the off-line and on-line commissioning of ISCOOL. Chapter 7 presents the first on-line experiment of neutron-rich Ga isotopes and Chapter 8 continues with a discussion of the results shown in Chapter 7.

CHAPTER 2

THE HYPERFINE STRUCTURE OF ATOMIC LINES

2.1 Hyperfine interaction and nuclear moments

The first observations of the hyperfine structure of optical transitions resolved into closely spaced fine lines was independently made by Michelson in 1891 and Fabry and Pérot in 1897 [26]. The range of this splitting is of the order of μeV $-$ meV, which is small compared to the fine structure splitting, hence the term "hyperfine" structure. The origin of this splitting is due to the interaction energy between the nuclear electromagnetic moments and the atomic fields and now it is well-understood, but it was only in 1924 that Pauli [27] first introduced the nuclear spin **I** in order to account for the observed hyperfine lines. In this way, the correct description of atomic states is achieved by using the vector sum of the atomic angular momentum **J** and the nuclear spin **I**, which is labelled as **F**

$$\mathbf{F} = \mathbf{I} + \mathbf{J}. \tag{2.1}$$

In the same way that atomic fine structure states are labelled by $|\, LSJM_J\rangle$, the

conservation of angular momentum **F** in an isolated system leads to states labelled by $|\, IJFM_F\rangle$. The total angular momentum **F** can be conceptualized in terms of a vector model as shown in Figure 2.1, where **I** and **J** are precessing around **F**.

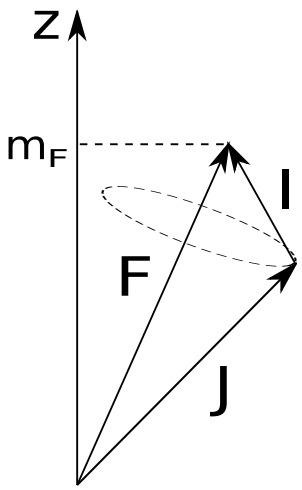

Figure 2.1: The vector model for the coupling of I and J to the angular momentum F.

There is a hyperfine multiplet of states for each I and J going from $F = I + J$ to $|\, I - J\,|$ in integer steps. The number of split components in a given multiplet is $(2J+1)$ or $(2I+1)$, whichever is smaller. In the absence of external fields, the M_F substates for a particular F value will be degenerate. Each F-state multiplet will have a different energy due to the electromagnetic interaction between the nuclear moments and the electromagnetic field produced at the nucleus by the electrons. The Hamiltonian which describes this interaction, H_{EM}, can be expressed in a multipole expansion of the product of two tensor operators of rank k [28]:

$$H_{EM} = \sum_{k=0}^{\infty} \mathbf{T}^k(n) \cdot \mathbf{T}^k(e), \tag{2.2}$$

The operators $\mathbf{T}^k(n)$ and $\mathbf{T}^k(e)$ act on the nuclear and electronic spaces, respectively. On the grounds of parity conservation of the electromagnetic interaction, the only terms which contribute to the Equation 2.2 are the even electric multipoles and odd magnetic multipoles. The hyperfine structure Hamiltonian is given by:

$$H_{hfs} = \sum_{i}^{N} \left[\mathbf{T}^0(n) \cdot \mathbf{T}^0(i) - \left(-\frac{Ze^2}{4\pi\varepsilon_0 r_i} \right) \right] + \sum_{k=1}^{\infty} \mathbf{T}^k(n) \cdot \mathbf{T}^k(e), \tag{2.3}$$

where the first sum is carried out for all the N electrons which interact with the monopole term ($k = 0$) via the Coulomb field. The difference of the terms in square brackets is what accounts for the field effect in the isotope shift (see section 2.2). In the second summation, the terms $k = 1$ and $k = 2$ are the magnetic dipole and electric quadrupole, respectively. The magnetic dipole term is associated with the nuclear spin I and the quadrupole term with the departures from a spherical charge distribution of the nucleus. In the optical spectra, the higher-order terms have a vanishingly small contribution to the hyperfine structure. The effects caused by the magnetic octupole ($k = 3$) and electric hexadecapole ($k = 4$) interactions, for instance, are already a factor of 10^8 smaller than the former terms [29], and hence are too small to be experimentally observed.

The shift in the atomic energy levels caused by a multipole k can be computed by projecting the product of $\mathbf{T}^k(n)$ and $\mathbf{T}^k(e)$ onto states of maximum I and J and using first-order perturbation theory [28]

$$\begin{aligned}\Delta E_k(IJF,IJF) &= (-)^{I+J+F}\begin{Bmatrix} I & I & k \\ J & J & F \end{Bmatrix} \\ &\times \left[\begin{pmatrix} I & k & I \\ I & 0 & -I \end{pmatrix}\begin{pmatrix} J & k & J \\ J & 0 & -J \end{pmatrix}\right]^{-1} A_k, \end{aligned} \tag{2.4}$$

where, A_k is given by the product of the matrix elements of the nuclear and electronic spaces (for $k \geq 1$):

$$A_k = \langle JJ \mid \mathbf{T^k}(\mathbf{e}) \mid JJ\rangle \cdot \langle II \mid \mathbf{T^k}(\mathbf{n}) \mid II\rangle. \tag{2.5}$$

The term in curly brackets in Equation 2.4 is a $6-j$ symbol, which controls the hyperfine structure through F. The terms in square brackets are $3-j$ symbols and are related to the projection of the tensor operators into the nuclear and electronic spaces. The hyperfine structure coupling constants A and B are defined with respect to A_k by [28]

$$A \equiv A_1/IJ, \tag{2.6}$$

$$B \equiv 4A_2. \tag{2.7}$$

2.1.1 Magnetic contribution

The energy shift caused by the magnetic dipole term is caused by the interaction between the nuclear magnetic dipole moment $\boldsymbol{\mu}$ and the magnetic field $\mathfrak{B}_l$ created by the electron currents in the nucleus and it is obtained from [29]

$$\begin{aligned} \Delta E_1(IJF,IJF) &= <\boldsymbol{\mu}\cdot\mathfrak{B}_l> \\ &= \frac{1}{2}AC, \end{aligned} \tag{2.8}$$

where C is given by

$$C = [F(F+1) - I(I+1) - J(J+1)]. \tag{2.9}$$

The A factor is explicitly written as:

$$A = \frac{\mu_I \mathfrak{B}_l}{IJ}, \tag{2.10}$$

Since I and J are fixed for a given multiplet, the spacing between neighbouring F's is accounted by the Landé interval for hyperfine components:

$$\Delta E_{F,F-1} = AF. \tag{2.11}$$

In cases where either $I = 0$ or $J = 0$, there is no hyperfine splitting.

2.1.2 Electric contribution

The energy shift caused by the electric quadrupole term is [28]

$$\Delta E_2(IJF,IJF) = \frac{B}{4}\frac{\frac{3}{2}C(C+1) - 2I(I+1)J(J+1)}{I(2I-1)J(2J-1)}, \tag{2.12}$$

where C is defined in Equation 2.9 and B is given by

$$B = eQ_s \left\langle \frac{\partial^2 V}{\partial z^2} \right\rangle . \tag{2.13}$$

In Equation 2.13, e is the electric charge, Q_s is the spectroscopic nuclear quadrupole moment, and the term in brackets is the average electric field gradient along the nuclear symmetry axis (taken arbitrarily as z) produced by the electrons at the nucleus. In addition to the atomic systems with either $I = 0$ or $J = 0$, the quadrupole contribution to hyperfine splitting also vanishes for those with $J = 1/2$ or $I = 1/2$.

2.1.3 Total hyperfine structure

The total observable energy for a hyperfine multiplet in an F state is given by

$$\Delta E_{total} = \nu_0 + \Delta E_1(IJF, IJF) + \Delta E_2(IJF, IJF), \tag{2.14}$$

where ν_0 is the fine-structure transition centroid. It should be noted that the electric quadrupole contribution in most cases can be seen as a small correction compared to the splitting caused by the magnetic term, and hence it causes a departure from the interval rule expressed by Equation 2.11. An illustration of the effect of both magnetic and quadrupole interactions in the hyperfine structure of an atomic transition $J_l \rightarrow J_u$, with the labels l and u standing for "lower" and "upper" states is shown by Figure 2.2.

It follows from Equation 2.10 that the ratio between the A hyperfine coefficients is a constant for all isotopes with the same atomic transition, being only a function of the electronic factors. Similarly, from Equation 2.13, the ratio between the B hyperfine coefficients is also a constant. As a consequence, if the ratios r_A and r_B are known

for one isotope, its possible to obtain the hyperfine coupling constants for an unknown isotope.

$$\frac{A_u}{A_l} = \frac{(\mathfrak{B}_l)_u\, J_l}{(\mathfrak{B}_l)_l\, J_u} = r_A, \tag{2.15}$$

$$\frac{B_u}{B_l} = \frac{\left\langle \partial^2 V/\partial z^2 \right\rangle_u}{\left\langle \partial^2 V/\partial z^2 \right\rangle_l} = r_B. \tag{2.16}$$

Electric dipole transitions between states labelled by $\mid IJFM_F\rangle$ and $\mid IJ'F'M'_F\rangle$ obey the rules given by 2.17.

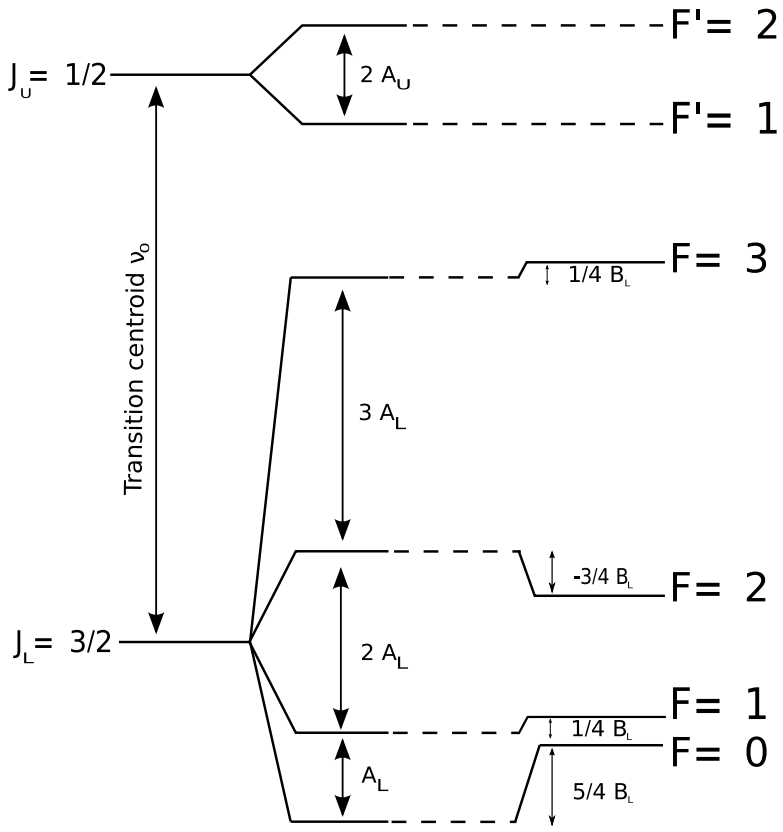

Figure 2.2: Scheme of a hypothetical atomic transition with $J_l = 3/2$, $J_u = 1/2$ and $I = 3/2$.

$$\Delta F = 0, \pm 1; \quad F + F' \geq 1. \tag{2.17}$$

The relative intensities of the peaks corresponding to electric dipole transitions between hyperfine components F and F' following spontaneous fluorescence decay obey the theoretical [1] value is given by [30], known as Racah coefficients

$$S_{F \to F'} \propto (2F+1)(2F'+1) \begin{Bmatrix} J' & F' & I \\ F & J & 1 \end{Bmatrix}^2. \tag{2.18}$$

This is a useful information which can be helpful in the determination of the nuclear spin.

2.1.4 Determination of μ_I and Q_s

An analytical determination of A and B and hence, μ_I and Q_s would require calculation of reduced matrix elements for the dipole and quadrupole operators in both electronic and nuclear spaces. This is a difficult problem. However, if the A factor and magnetic moment are known for a reference isotope, then it is possible to obtain μ_I for an unknown isotope. This assumption is valid ignoring an anomaly due to magnetization distribution in nucleus[2]. Using similar arguments, the Q_s can also be obtained if the B factor and quadrupole moment of a reference isotope are known. Equations 2.19 and 2.20 are used to obtain μ_I and Q_s.

[1] In this approximation, stimulated emission effects are ignored.

[2] This phenomenon is called *Bohr-Weisskopf effect* or *hyperfine anomaly* [31]. When this effect is taken into account, equation 2.19 must be modified to $\mu_I = \frac{AI}{A_{ref} I_{ref}} \mu_{ref}(1+\Delta)$, where Δ is the anomaly. However, for gallium, $\Delta \approx 0$ [32], and therefore equation 2.19 can be used.

$$\mu_I = \frac{AI}{A_{ref} I_{ref}} \mu_{ref}, \tag{2.19}$$

$$Q_s = \frac{B}{B_{ref}} Q_s^{ref}. \tag{2.20}$$

2.2 The isotope shift

Changes in the nuclear charge distribution and volume cause shifts in the electronic energy levels. The isotope shift (IS) is defined as the difference in the centroid frequencies of a given atomic transition between two different isotopes, A and A', where A' is the heavier

$$\delta\nu^{AA'} = \nu^{A'} - \nu^{A}. \tag{2.21}$$

Equation 2.21 can be divided into two different terms, the mass shift (MS) and the field shift (FS). The former is due to the changes in nuclear recoil kinetic energy between two isotopes, and therefore it is a finite mass effect, whereas the latter can be accounted for by considering the way the atomic electrons interact with the electromagnetic field generated by the nuclear charge distribution and consequently it is a finite size effect. Thus:

$$\delta\nu^{AA'} = \delta\nu_{MS}^{AA'} + \delta\nu_{FS}^{AA'}. \tag{2.22}$$

2.2.1 The mass shift

The total linear momentum in the atomic centre of mass frame is given by

$$\mathbf{p_{nuc}} + \sum_i \mathbf{p_i} = 0, \tag{2.23}$$

where $\mathbf{p_{nuc}}$ is the nuclear momentum and $\mathbf{p_i}$ is the momentum of the i^{th} electron. Conservation of linear momentum in the centre of mass frame leads to $\mathbf{p_{nuc}} = -\sum_i \mathbf{p_i}$. The total kinetic energy of the system is

$$\begin{aligned} KE &= \frac{1}{2M}(\mathbf{p_{nuc}})^2 + \sum_i \left(\frac{\mathbf{p_i}^2}{2m_e}\right) \\ &= \frac{1}{2M}\left(\sum_i \mathbf{p_i}^2 + 2\sum_{i>j} \mathbf{p_i}\cdot\mathbf{p_j}\right) + \frac{1}{2m_e}\sum_i \mathbf{p_i}^2, \end{aligned} \tag{2.24}$$

where M is the nuclear mass and m_e is the electron mass. Terms of $\mathbf{p_i}^2$ can be combined and the masses re-expressed as the reduced mass $\mu = \left(\frac{Mm_e}{M+m_e}\right)$,

$$KE = \frac{1}{2\mu}\sum_i \mathbf{p_i}^2 + \frac{1}{M}\sum_{i>j} \mathbf{p_i}\cdot\mathbf{p_j}. \tag{2.25}$$

Normal Mass Shift

The first term in equation 2.25 gives the shift in the energy levels for an atom with reduced mass μ. By considering $E(\infty)$ to be the energy level of a hypothetical atom with an infinitely heavy nucleus, Hughes and Eckart [33] were able to show that the energy levels of an atom with a finite nuclear mass M is

$$\begin{aligned} E(M) &= E(\infty)\frac{\mu}{m_e} \\ &= E(\infty)\frac{M}{M+m_e}. \end{aligned} \tag{2.26}$$

The change in the energy level of an atomic transition between isotopes A and A' can be calculated with Equation 2.26, for $E(\infty)$ as reference is given by [29]

$$\delta(\Delta E)^{A'-A} \approx E(\infty)\frac{m_e \delta A}{AA'}, \tag{2.27}$$

where $\delta A = A' - A$ Equation 2.27 can be redefined as the difference in the transition frequency of a given line for two different isotopes in the following way:

$$\delta\nu_{NMS}^{AA'} \approx \frac{m_e \delta A}{AA'}\nu, \tag{2.28}$$

where ν is the line frequency of the transition involving A. Equation 2.28 is referred to as the *Normal Mass Shift (NMS)*. It is useful to put real numbers in order to understand the magnitude of this shift. In the case of a $P_{1/2} \rightarrow S_{1/2}$ transition at 417.209 nm of ^{69,70}Ga isotopes, the normal mass shift is of the order of 80 MHz.

Specific Mass Shift

The *Specific Mass Shift (SMS)* is caused by the second term of Equation 2.25, which represent a sum over all momenta correlations between pairs of electrons. This term may reinforce the normal mass effect or act against it, depending on whether the pairs of electrons are moving in the same direction or in opposite ways. This term is difficult to calculate accurately for a many-electron system. It is sufficient to mention that the specific mass shift is also proportional to $\delta A/AA'$. The total mass shift is therefore expressed as [29]

$$\begin{aligned} \delta\nu_{MS}^{AA'} &= \delta\nu_{NMS}^{AA'} + \delta\nu_{SMS}^{AA'} \\ &= \frac{A'-A}{AA'}\widetilde{M}, \end{aligned} \tag{2.29}$$

where $\widetilde{M} = N + S$, is the sum of the normal (N) and the specific (S) mass shifts. Unless reliable calculations of the specific mass shifts are available, the normal mass shift and the specific mass shift can be related empirically [34] by :

$$\delta\nu_{SMS}^{AA'} = \begin{cases} (0.3 \pm 0.9)\delta\nu_{NMS}^{AA'} & \text{, for } ns - np \text{ transitions} \\ (0 \pm 0.5)\delta\nu_{NMS}^{AA'} & \text{, for } ns^2 - nsnp \text{ transitions} \end{cases}$$

2.2.2 The field shift

The difference between the monopole term ($k = 0$) and the $\frac{Ze^2}{4\pi\varepsilon_0 r}$ terms in the Equation 2.3 gives the field shift effect of the isotope shift. This effect is illustrated by Figure 2.3. This figure shows that an electron will be less bound to a nucleus with a finite charge distribution, than to a point charge nucleus. If $\frac{Ze}{4\pi\varepsilon_0 r}$ is the Coulomb potential of a point charge and $\phi(r)$ the electrostatic nuclear field, it is possible to apply first-order perturbation theory to obtain the change in the electron energy levels in the following way [35]

$$\Delta E = -e \int \left(\phi(r) - \frac{Ze}{4\pi\varepsilon_0 r} \right) \Psi^2(r) dV, \tag{2.30}$$

where $\Psi(r)$ is the electronic wavefunction. If $s(l = 0)$ states are considered, the wave function remains independent of the angular part and presents only a radial dependence. Since there is a non-zero probability of finding s-electrons inside the nucleus,

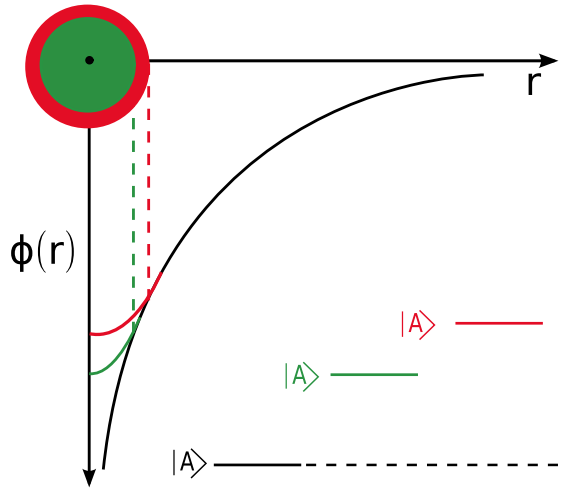

Figure 2.3: Scheme of the electrostatic potential as a function of the distance from the center of the nucleus r, for three general cases: a point charge, as indicated in black; a small nucleus with a finite charge distribution, indicated in green and a large nucleus, as indicated in red. The effects on the energy level of a state labeled by $|A\rangle$ are also highlighted.

and considering that the nuclear size is smaller than the atomic radius, the radial wave function remains constant and equation is reduced to [35]

$$\Delta E = \frac{Ze^2}{6\varepsilon_0}\Psi^2(0)\langle r^2\rangle, \tag{2.31}$$

where the mean square charge radii $\langle r^2\rangle = \frac{1}{Ze}\int r^2 \rho dV$, with ρ being the charge density. In the case of a spherically symmetric nucleus, $\langle r^2\rangle_0 = \frac{3}{5}R^2$, where $R = 1.22A^{1/3}$ fm [11]. From equation 2.31, it follows that for two isotopes A and A', the FS is given by:

$$\delta\nu_{FS}^{AA'} = -\frac{Ze^2}{6\varepsilon_0}\Delta\Psi^2(0)\delta\langle r^2\rangle^{AA'}/h. \tag{2.32}$$

If relativistic and electronic screening effects are included in the formalism, equation 2.32 is then generalised into the form [19]

$$\delta\nu_{FS}^{AA'} = F(Z)\lambda^{AA'}, \tag{2.33}$$

where, $F(Z)$ is a function showing a Z dependence, called *electronic form factor*, containing the required relativistic corrections [36]. $\lambda^{AA'}$ is a power series expansion in $\delta\langle r^2\rangle$

$$\lambda^{AA'} = \delta\langle r^2\rangle^{AA'} + \frac{C_2}{C_1}\delta\langle r^4\rangle^{AA'} + \frac{C_3}{C_1}\delta\langle r^6\rangle^{AA'} + \ldots \tag{2.34}$$

The coefficient C_i are tabulated values [37]. To a good approximation $\lambda^{AA'} \approx \delta\langle r^2\rangle^{AA'}$, for light or medium-mass elements. In summary, the total measured isotope shift is given by

$$\delta\nu^{AA'} = F(Z)\delta\langle r^2\rangle^{AA'} + \frac{A'-A}{AA'}M. \tag{2.35}$$

In order to obtain the changes in the mean square charge radii from the measured isotope shifts, it is necessary to subtract the mass shift and have knowledge of $F(Z)$. For light systems, the mass shift plays a more significant role in the overall shift. On the other hand, the field shift becomes more predominant in heavier elements, whereas the mass shift becomes negligible. The usual ways to obtain $F(Z)$ is by either performing *ab initio* calculations or by applying semi-empirical techniques using, for instance, *ns-np* transitions [38]. Non-optical measurements also allow a reasonable calibration of for $F(Z)$ heavy elements [20]. The situation for gallium is somewhat more difficult, since this element is located at an intermediate mass region ($A \sim 70$) and therefore the specific mass shift must be taken into account. Non-optical data on radii exist

Table 2.1: Measured isotope shift and charge radii for gallium isotopes.

A	IS ($^2P_{1/2} \rightarrow ^2S_{1/2}$)[a] ($\lambda = 403.3$ nm) [MHz]	IS ($^2P_{1/2} \rightarrow ^2S_{1/2}$)[a] ($\lambda = 417.2$ nm) [MHz]	$\langle r^2 \rangle^{1/2}$[b] [fm]
69	0	0	3.996
71	-32.8 ± 3.5	-39.6 ± 3.5	4.011

[a] The ^{69}Ga isotope was used as reference.
[b] Model-dependent RMS value. See [36] for details.

[36] for ^{69,71}Ga stable isotopes in addition to optical isotope shift data [39]. Table 2.1 summarises the information which is available in the literature.

CHAPTER 3

EXPERIMENTAL APPARATUS AND METHODS

3.1 Essentials of laser spectroscopy

The underlying mechanism of the technique applied in this work is the absorption of electromagnetic radiation by an atomic system and the measurement of the number of photons which originates from the ensuing spontaneous emission of radiation. This chapter will discuss the basic laser spectroscopy techniques which allow high resolution measurements of the hyperfine structure of atomic nuclei.

3.1.1 Natural line width

In an ideal two-level atom, as described by Figure 3.1, the lower and upper states j and k are separated by an amount of energy ΔE_{jk}. It is sufficient to picture the atom-radiation interaction semiclassically, in which the radiation at angular frequency ω_{jk} is treated as a classical field and the atomic wavefunction is in a superposition of lower and upper states, whose energy levels are perturbed by this field. The half life of the emission process is τ_{jk}.

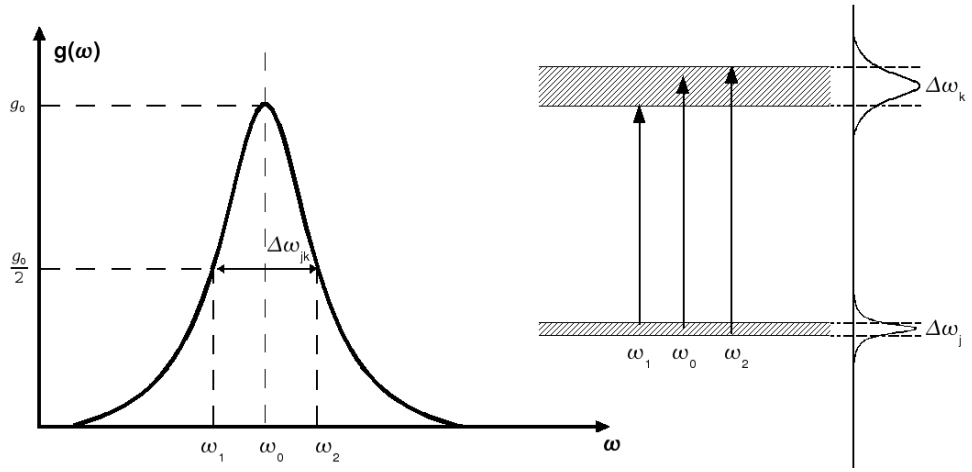

Figure 3.1: Natural line width of a transition between states labelled by j and k.

In fact, as the figure suggests, the transition which populates the upper state k is not only caused by an electromagnetic radiation with a defined frequency ω_{jk}, but instead by any frequency lying within a finite distribution of frequencies centered around ω_0, which is the resonant frequency. This "natural breadth" or linewidth of the transition, $\Delta\omega_{jk}$, is characterized by the full width at half-maximum (FWHM) of the *line profile* $g(\omega)$, described by a *Lorentzian* line shape

$$g(\omega) = \frac{1}{2\pi} \frac{\Delta\omega_{jk}}{(\omega - \omega_0)^2 + \Delta\omega_{jk}^2/4}. \tag{3.1}$$

The width of the line profile is given by the convolution of the individual widths of the j and k "lines". When the lower level is the ground state, $\Delta\omega_{jk}$ collapses to $\Delta\omega_k$. The latter is calculated by summing over Einstein's A_{ki} coefficients, which are the probabilities of transitions from k to any allowed low-lying state i [40]. In this two-level atom the summation is carried only for the $k \rightarrow j$ transition

$$\Delta\omega_k = \sum_i A_{ki} = A_{kj} \tag{3.2}$$

This two-level system has an optical absorption cross section given by [41],

$$\sigma(\omega) = 3 \times \frac{\pi^2 c^2}{\omega_0^2} A_{kj}\, g(\omega), \tag{3.3}$$

For the case of excitation with a laser tuned on resonance ($\omega = \omega_0$) with wavelength $\lambda_0 = 2\pi c/\omega_0$, the optical cross-section may be approximated by

$$\sigma(\omega_0) \approx \frac{\lambda_0^2}{2}, \tag{3.4}$$

which is on the order of 10^{-9} cm^2, for transitions lying in the optical spectrum. When compared with nuclear scattering cross-sections (10^{-24}cm^2), the advantage of using lasers to probe the atomic nucleus becomes evident.

3.1.2 Broadening of the spectral lines

The broadening of the spectral lines are due to different mechanisms, classified as homogeneous or inhomogeneous. Relevant to this work are the homogeneous power broadening and Doppler broadening.

Power broadening

The continuous interaction of the radiation field with the atomic system causes transitions between the lower and upper states at a frequency called *Rabi frequency*. This frequency is proportional to the field amplitude and the atomic dipole matrix element

[42]. At a certain value, called *saturation intensity*, the populations in the lower and upper states will be equal. An increase in the laser power leads to more rapid Rabi oscillations, which effectively shortens the lifetime of the upper level. Through the energy-time uncertainty relation, this mechanism leads to a broadening of the line shape, which causes a loss in resolution and to a lowering of the peak value of the line-shape function $g(\omega)$ [41]. The latter effect causes a loss in detection efficiency. Power broadening can be mitigated if the laser power is set below the saturation value for the atomic transition. In practice, this is achieved by optimizing the measured fluorescence count and linewidth as a function of the laser power.

Doppler broadening

This broadening mechanism is related to the thermal velocities of the atomic sample. Since each atom in the sample to absorb radiation on its rest frame, the range of frequencies that can be absorbed by the sample is widened. The Doppler width for a gas of thermal particles with resonance frequency ω_0 is given by [42]

$$\delta\omega_D = 2\sqrt{\ln 2}\,\omega_0 \frac{v_p}{c}, \quad v_p = \left(\frac{2K_B T}{M}\right)^2 \tag{3.5}$$

Depending on the mass and temperature, the Doppler broadening can be on the order of several GHz [41], which in most cases washes out the individual peaks of the hyperfine structure, which are typically separated by < 1 GHz.

3.1.3 Collinear laser spectroscopy with fast beams

The traditional methods used to perform Doppler-free optical spectroscopy on radioactive beams are the crossed beam technique and the collinear laser technique. The crossed beam technique consists of "crossing" the laser and ion beam using collimating slits in such a way that only the fraction of the atoms travelling *perpendicular* to the direction of the laser beam are excited. It is not hard to imagine that this technique requires a substantial amount of atoms, which most of the time are not available for radioactive species. This is one of the main reasons this technique has given place to more efficient Doppler-free methods such as the collinear technique, which has been used in the work reported in this thesis. In a typical collinear spectroscopy setup, accelerated radioactive ions are overlapped with a co- or counter-propagating laser beam. Historically [43], this geometry was developed out of the necessity to improve the efficiencies and resolution of laser spectroscopy measurements at on-line separator facilities. The collinear geometry is superior to the crossed beam technique because the overlapping between the laser and the ions/atoms along the axial direction naturally maximises the interaction region. In addition, Doppler-free measurements can be performed due to the velocity compression of the ion beam caused by electrostatic acceleration. This fact was first noted independently by Kaufman [44] and Wing [45].

The difference in velocity of two identical ions with initial energies $E_1 = 0$ and $E_2 = K_B T$ along the beam propagation direction z is given by

$$\delta v_z = v_2 - v_1 = \sqrt{\frac{2K_B T}{M}} \tag{3.6}$$

If the ions are subject to acceleration due to an electrostatic potential V, the gain in energy is eV. Now, the difference in velocity $\delta v_z'$ between the accelerated ions is

$$\delta v_z' = v_2' - v_1' = \sqrt{\frac{2(eV + K_B T)}{M}} - \sqrt{\frac{2(eV)}{M}} = ({v_1'}^2 + v_2^2)^{1/2} - v_1' \tag{3.7}$$

Equations 3.6 and 3.7 are related by

$$\begin{aligned} \delta v_z' &\approx \frac{1}{2}\left(\frac{v_2}{v_1'}\right)\delta v_z \\ &\approx \frac{1}{2}\sqrt{\frac{K_B T}{eV}}\delta v_z, \end{aligned} \tag{3.8}$$

which states that an increase in the acceleration voltage V causes a reduction in the velocity spread. The considerations taken which led to equation 3.8 may be generalized to an ensemble of N ions with a Maxwell-Boltzmann velocity distribution. In this case, the spread in kinetic energy for an ensemble of ions produced in an ion source with average velocity $\bar{v}$ is a constant of motion,

$$\delta E = m\bar{v}\delta v = cte. \tag{3.9}$$

This situation is graphically illustrated by Figure 3.2. The reduced Doppler width due to the velocity compression of accelerated ions is found to be

$$\delta\omega_D = \frac{2\omega_0 K_B T}{c}\sqrt{\frac{\ln 2}{MeV}} \tag{3.10}$$

Therefore, for the case of thermal ions at 60 keV, the Doppler width can be reduced to less than the natural line width.

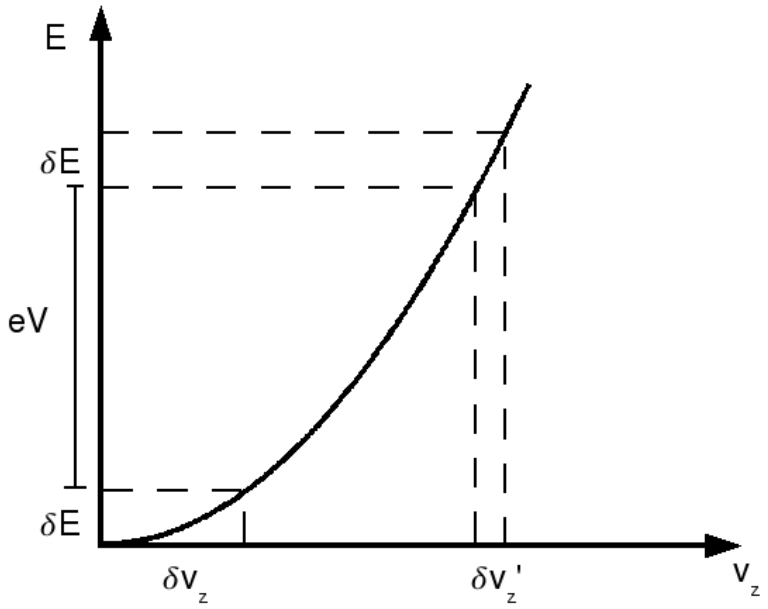

Figure 3.2: Illustration of the velocity compression mechanism along the beam propagation in the z direction. Note that the spread in energy does not change with the electrostatic potential.

In laser spectroscopy experiments, a scan can be performed either by changing the laser frequency or by exploiting the (relativistic) Doppler effect. While changing the laser frequency requires a fine control via scanning optical devices, it is known that an observer moving towards a source of electromagnetic radiation will perceive a frequency "shifted to the blue", whereas if the observer is moving away from the the source the shift will be "to the red". The collinear laser geometry allows the laser frequency to be kept fixed and the scan to be performed by Doppler-shifting the ions to resonance, by changing the voltage of the sample. Consider the diagram shown by Figure 3.3. It shows the collinear geometry, in which the ions are irradiated with a co-propagating laser light.

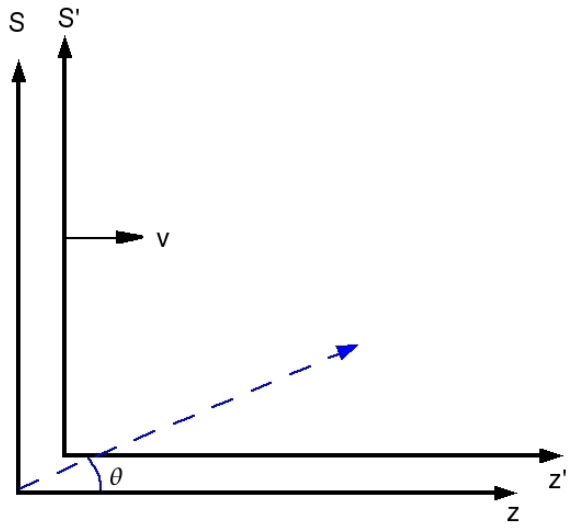

Figure 3.3: Frame S denotes the laser source fixed in the lab and S' is the frame of the ions moving away from the laser with velocity v.

In the S' frame the energy of a single ion is $E' = Mc^2$. In the S frame the ion energy is Lorentz-transformed into

$$\begin{aligned} E &= \gamma Mc^2 \\ &= \left(1-\frac{v^2}{c^2}\right)^{-1/2} Mc^2 = \underbrace{Mc^2}_{rest} + \underbrace{eV}_{acc.} \end{aligned} \tag{3.11}$$

Rearranging equation 3.11 gives a useful relation:

$$\beta = \frac{v}{c} = \left[1-\frac{1}{(1+\alpha)^2}\right]^{1/2}, \quad \alpha = \frac{eV}{Mc^2}. \tag{3.12}$$

The relativistic Doppler shifted frequency ν' in the frame S' is related the frequency fixed on the resonant frequency ν by

$$\frac{\nu'}{\nu} = \gamma(1+\beta\cos\theta) \tag{3.13}$$

The angle θ accounts for the departure from the collinear geometry and is usually small, on the order of mrad. If $\theta = 0$ then the shift can be expressed as

$$\nu' = \nu(1+\alpha+\sqrt{\alpha^2+2\alpha}) \tag{3.14}$$

During an on-line experiment it is important to determine how the frequency will be shifted with the scanning voltage, V. Thus

$$\frac{\delta\nu'}{\delta\alpha} = \frac{-\nu}{\sqrt{\alpha^2+2\alpha}} \tag{3.15}$$

Since $\delta\alpha = e\delta V/Mc^2$, a variation of the frequency with the scanning voltage is obtained,

$$\frac{\delta\nu'}{\delta V} = \frac{-\nu e}{Mc^2\sqrt{\alpha^2+2\alpha}}. \tag{3.16}$$

This can be realised by electrostatic plates which are introduced prior to the interaction region. It should be noted that the relativistic expression (equation 3.14) used for the conversion from scanning voltages to frequency provides the general procedure which can be used for any experiment of nuclei of any mass accelerated at any energy. For the case of gallium isotopes ($A \approx 70$) accelerated at 50 keV, $\beta \approx 10^{-3}$, which means that a non-relativistic expression can be used. However, this procedure introduces a systematic error of ~ 1 MHz for calculations of isotope shifts. This becomes more

problematic if lighter species are investigated.

When $\theta \neq 0$ and not negligible, which happens when there is a poor overlap between the ion/atom and the laser beam, the measured resonances are modified. This non-homogeneous broadening effect is known as *peak skewing* and was studied by Campbell [46]. From equation 3.13, this effect can be accounted for by

$$\begin{aligned} \Delta\nu' &= \nu'(\theta) - \nu'(0) \\ &\approx \nu\gamma\beta\frac{\theta^2}{2}. \end{aligned} \tag{3.17}$$

3.2 Laser instrumentation

The spectroscopic experiments described in this work necessitated the use of a continuous-wave tunable Ti:Sa laser as well as an external frequency doubler. This section delineates the principle of operation of these devices.

3.2.1 The titanium sapphire laser

The Ti:Al_2O_3 laser, also known as titanium sapphire (or simply Ti:Sa) was developed by Moulton [47] in the 1980's and belongs to a wide class of solid-state gain media. It has become the most popular choice among the others because the interaction of the Ti^{3+} ion with the host lattice (Al_2O_3) produces a broad laser output, with a tuning range from $680-1025$ nm. Additionally, since there is no other *d* electron states above the levels involved in the laser operation, this system does not suffer from excited state absorption, which is an unwanted loss mechanism of pump power. This system can be

though of as a 4-level system and the electronic structure of the levels involved in the absorption and emission is shown by Figure 3.4.

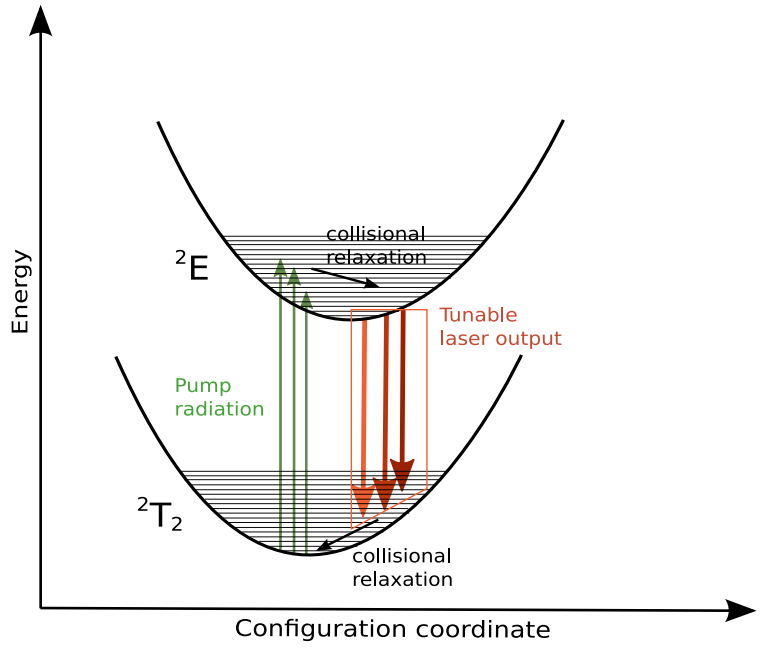

Figure 3.4: The electronic structure of the Ti:Al_2O_3.

Optical pumping excites the ground state electrons from the $^2T_2$ band to the excited E_2 band. This absorption can occur from $400-600$ nm. Collisional relaxation allows the electrons to de-excite to the bottom of the band. At this stage the population inversion condition is met and stimulated emission then occurs from this level down to the ground state band. The drain transition is achieved through rapid collisional relaxation to the bottom of the ground state band. There are several cavity implementations which can be used to obtain a laser output from a Ti:Sa crystal. In this work, the commercial model Coherent $899-21$ ring cavity was used to generate a laser output on CW mode. Typical pump laser power ranges from $5-15$ W. The Ti:Sa laser was initially pumped

by an argon ion laser for the on-line commissioning and subsequently by a 18 W Verdi laser for the gallium work. The Coherent $899-21$ ring cavity has the "figure of eight" geometry as shown by Figure 3.5.

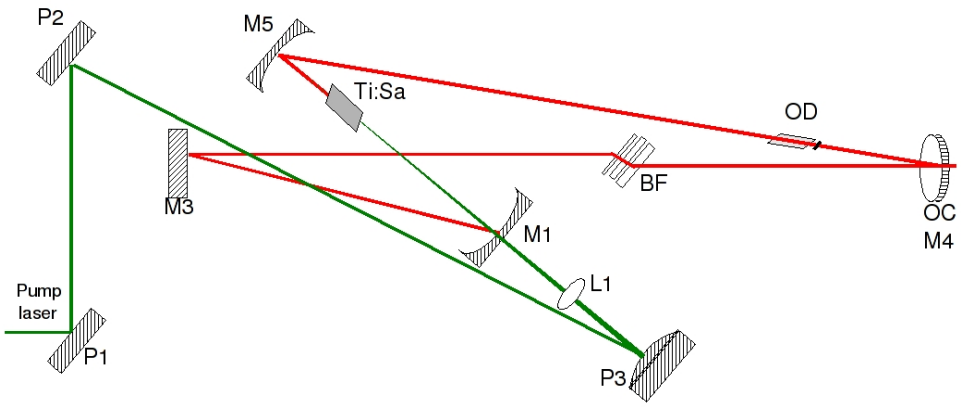

Figure 3.5: Scheme of the $899-21$ cavity. $P1$, $P2$ and $P3$ are the pump mirrors. "The figure of eight" cavity is formed with $M1$, $M3$, $M4$ and $M5$ folding mirrors. See text for more details.

This model has passive and active frequency controls, which produce a single longitudinal mode output. In order to guarantee mechanical stability, as well as to avoid thermal drifts, the cavity elements were mounted on a rigid Invar rod, as shown by Figure 3.6.

The cavity elements comprised four folding mirrors ($M1$, $M3$, $M4$ and $M5$). The last folding mirrors serves as the output coupler where the laser light passes through. The cavity also has a lens, $L1$, which is used to focus the light from the pump mirror into the Brewster cut Ti:Sa crystal. Other elements are the optical diode OD, a Lyot filter (a stack of three birefringent filters BF [48]) and an intra cavity assembly (ICA), used for single mode selection. The optical diode, which consists of a Faraday rotator and

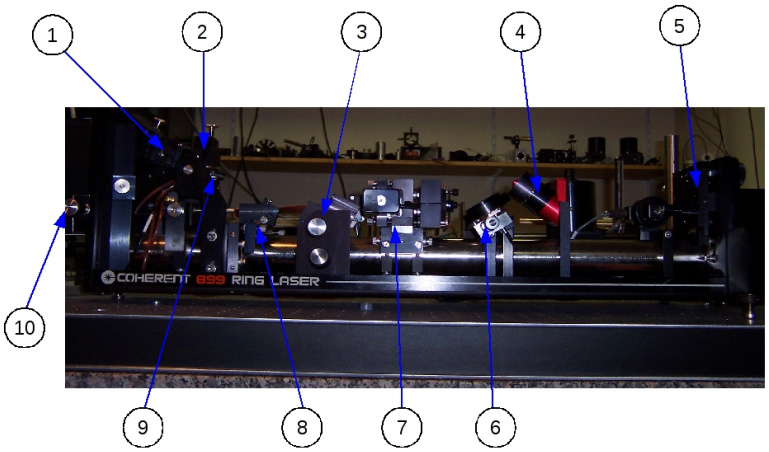

Figure 3.6: All the elements which comprise the Coherent $899-21$ ring cavity assembly: 1. Upper fold mirror $M5$. 2. Lower fold mirror $M3$. 3. Pump mirror $P3$. 4. Optical diode. 5. Output coupler $M4$. 6. Birefringent filter. 7. Intra cavity assembly (ICA). 8. Focusing lens $L1$. 9. Titanium:Sapphire crystal. 10. Periscope optics $P1$/$P2$.

a quarter-wave plate, causes the light inside the cavity to travel only in one direction. The birefringent filters are placed at Brewster's angle and serve as a coarse mode selector. Tunability can be achieved by rotating the stack around the plane containing the crystal's optical axis. For a given wavelength corresponding to an integral number of full-wave retardations, the laser polarization is unaltered by the stack; otherwise the laser polarization is modified and suffer Brewster losses in the cavity [49].

The ICA comprised a thin and a thick etalons. After the insertion of this element in the cavity, the bandwidth is narrowed to 10 MHz. A temperature stabilised etalon was placed externally to the cavity, and was used to achieve mode stabilisation, against shirt term drifts. This arrangement permitted the laser to operate with a bandwidth of $\sim$ 1MHz. The laser wavelength was monitored with a wavemeter with a precision of 3 MHz. This precision was enough for the spectroscopy of gallium, since its natural

linewidth is $\sim$ 25 MHz. The output power of this laser was typically 1 W.

During the on-line commissioning of ISCOOL, the lines used were within the fundamental output of the Ti:Sa. However, for the gallium run, ultraviolet light was needed in order to excite the transitions of interest (403 and 417 nm). Therefore, the Ti:Sa output was frequency doubled by an external cavity.

3.2.2 The frequency doubler unit

In order to produce the second harmonic laser light used in the gallium experiment (403 nm and 417 nm), the fundamental light from the Ti:Sa was directed to a commercial external frequency doubler, WAVETRAIN®, from Spectra-Physics [50]. This apparatus is a ring cavity, which resembles a delta is shown by Figure 3.7.

In order to achieve cavity stabilization, an active control method is implemented. This method is based on the Pound-Drever-Hall technique, which is aimed to measure changes in the derivative of the reflected light from the cavity. Qualitatively, this technique consists of adding sidebands to the fundamental laser beam and picking the reflected beam. The sidebands are added due to phase modulation of the laser after it passes through an electro-optic crystal. To improve the efficacy of the locking technique and hence the cavity stability, the sidebands should be far enough from the resonance conditions inside the cavity for them to be reflected. This reflected signal is mixed with the fundamental and by using phase sensitive detection, an error signal is obtained and fed back to a prism mounted on a piezo control, which adjusts the length of the cavity accordingly. This arrangement therefore ensures the cavity stability. The

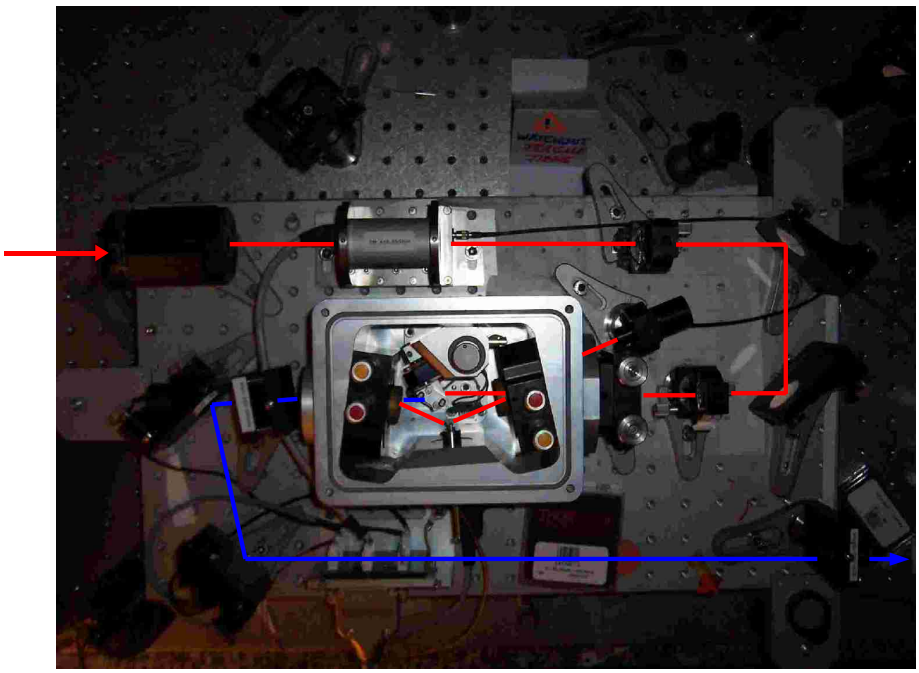

Figure 3.7: The Spectra-Physics Wavetrain external frequency doubler cavity together with the beam paths of the fundamental and doubled light.

Pound-Drever-Hall technique offers many advantages over previous locking schemes, since phase-sensitive detection decouples the variations on the laser frequency and power. A detailed and approachable explanation of this technique can be found in [51], for example. The cavity, along with its main optical components are shown by Figure 3.8.

The fundamental beam passes through a retardation plate *RP*. The next optical component is the phase modulator *PM*, which consist of $2KD^{*}P$ electro-optic crystals, driven by an rf oscillator. This part of the device also contains the phase sensitive electronics. The phase modulator adds sidebands to the fundamental beam. The beam

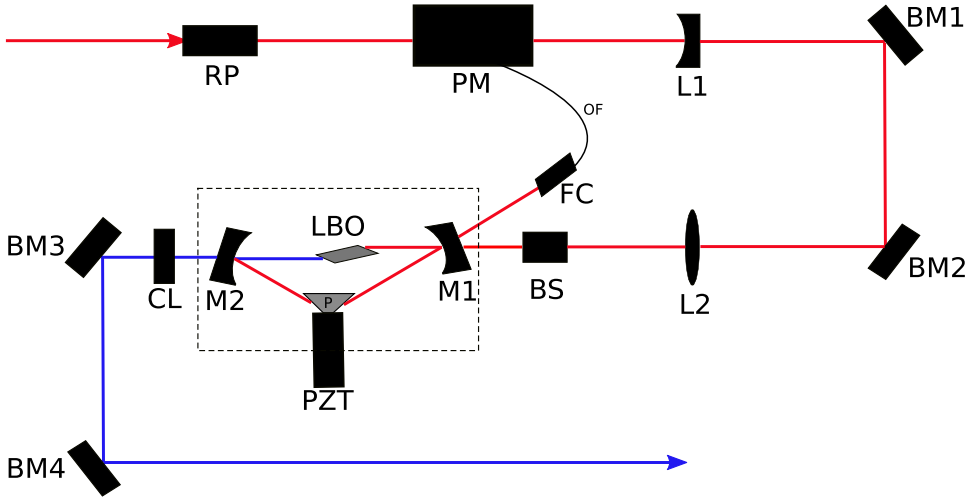

Figure 3.8: The Spectra-Physics Wavetrain external frequency doubler cavity together with the beam paths of the fundamental and doubled light. The Delta cavity is comprised by $M1$, $M2$, PZT and the non-linear crystal, LBO. A major part of the fundamental which is not converted makes several round trips in the Delta cavity. A small fraction of the fundamental is also used for the phase sensitive detection electronics. See text for more details on the other components of this device.

is then directed to the cavity by lenses ($L1$ and $L2$) and bending mirrors $BM1$ and $BM2$. By careful adjusting the foci of $L1$ and $L2$, as well as the beam shifter BS, the incoming laser can be mode-matched with the cavity. The ring cavity has the shape of a triangle and the beam is deflected to the folding mirrors $M1$ and $M2$ by a prism P. This arrangement improves the conversion efficiency with respect to other cavity arrangements (e.g. the bow-tie resonator), since the losses are minimised by replacing two folding mirrors by a Brewster cut prism P. The fundamental passes through the non-linear crystal, Lithium Triborate (LBO) and the second harmonic output leaves through $M2$. The major part of the fundamental which was not converted makes several round trips in the Delta cavity, which allows more power to be built, greatly improving

the conversion efficiency. If the fundamental is not perfectly resonating in the cavity, part of it will leak and will be picked up by a fiber couple FP and sent to the phase modulator module via an optical fiber OF. The error signal is then fed back to the piezo mount PZT, which stabilizes the cavity against vibrations caused by acoustic noise. The frequency-doubled output beam is reshaped into a circular and non astigmatic beam by a cylindrical lens CL and is directed to the ISOLDE experimental hall by $BM3$ and $BM4$.

CHAPTER 4

THE ISOLDE FACILITY

The Isotope Separator On-Line Device, ISOLDE, is a factory of radioactive ion beams, which currently produces more than 600 isotopes of 70 different chemical elements. The facility is part of CERN's accelerator complex, and it has been in operation since 1967. This chapter outlines the main features of this facility in which the experiments reported in this thesis were performed.

4.1 Facility layout

Figure 4.1 shows the structure of CERN's accelerators network and ISOLDE is among the various experiments hosted by the laboratory. The radioactive beams are produced at this facility by means of proton, and sometimes neutron induced reactions on a thick target. The ISOLDE facility utilizes the ISOL method for the separation of radioisotopes. This concept, which was first developed back in the late 1940's by Koch and collaborators [52] basically consists of producing and separating radioactive ions through a mass spectrograph fast enough so that the beam can be delivered to experiments located downstream the mass separator. Over the years, the method has not

changed in concept. However, the improved selectivity in the ionization process, as well as in the mass resolving power of current mass spectrographs have enabled the production of rare isotopes at intensities of up to 10^{11} atoms per μA proton beam [53].

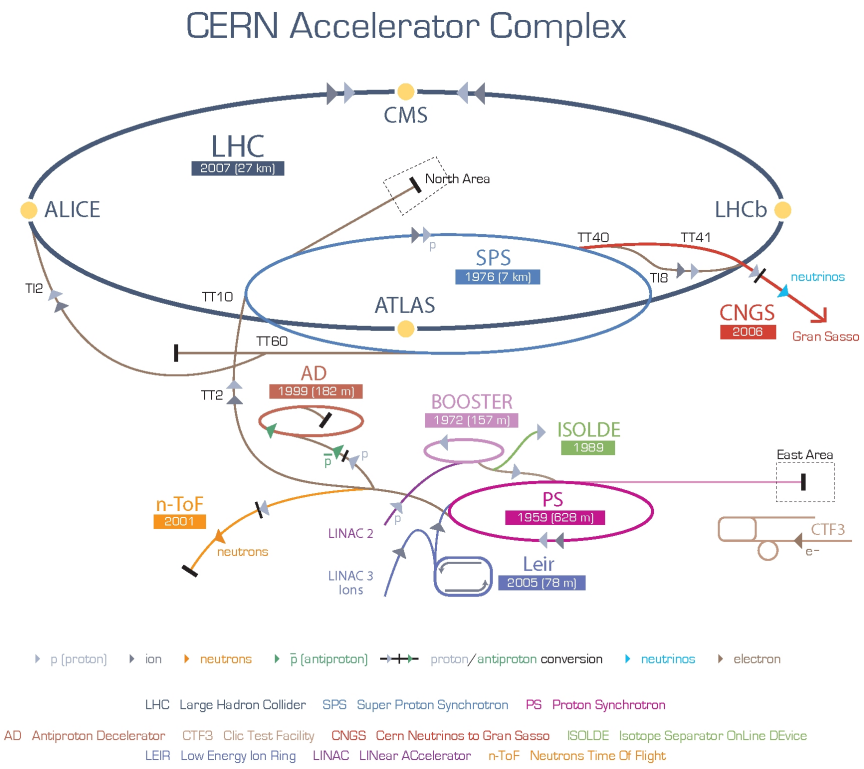

Figure 4.1: CERN accelerator complex and its various experiments. The position of ISOLDE (green) can be seen with respect to the proton synchrotron booster, indicated in pink.

The current installations of ISOLDE, as shown by Figure 4.2, went into operation in 1992, after an upgrade which placed the facility at one of the delivery arms of the Proton Synchrotron Booster, PSB, which consists of a stack of four 50 m diameter accelerator rings. The PSB receives 50 MeV protons from a linear accelerator, LINAC 2. The beam coming from the LINAC 2 is split into four parts. Each part is then

sent to a PSB accelerator ring, at a particular order. These beams are subsequently accelerated, synchronised and recombined for extraction. The timing involved in this process is what determines the ultimate time structure of the proton pulse delivered to ISOLDE. At ejection the proton beam reaches energies of up to 1.4 GeV. The proton pulses delivered to CERN experiments by the PSB has a timing structure, namely, the "supercycle". In one supercycle, several experiments receive a fixed amount of proton pulses. The pulsed are allocated in slots and the slot distribution is decided by the PSB technical team. Typically, the PSB delivers typically 40 proton pulses per supercycle, with an interval of 1.2 s between each pulse. At present ISOLDE takes approximately 20 pulses of 3×10^{13} protons, totalling an average proton DC current of 2 μA, and never exceeding 2.5 μA due to radioprotection issues.

4.1.1 The target and ion source unit

There are two independent target stations at ISOLDE, each connected to different mass separators. These are called the general purpose separator (GPS) and the high resolution separator (HRS); the latter has a mass resolving power of $M/\Delta M = 5000$. These two stations offer great flexibility to the users in that it is possible to schedule beam time in such a way that their use is whenever possible alternated - an experiment can run in one of the target stations, while the radiation levels at the other station goes down for a target change to be performed for the next experiment. A typical ISOLDE target unit is shown by Figure 4.3. Due to the high radiation levels at the target area, robotic arms are used to replace the units.

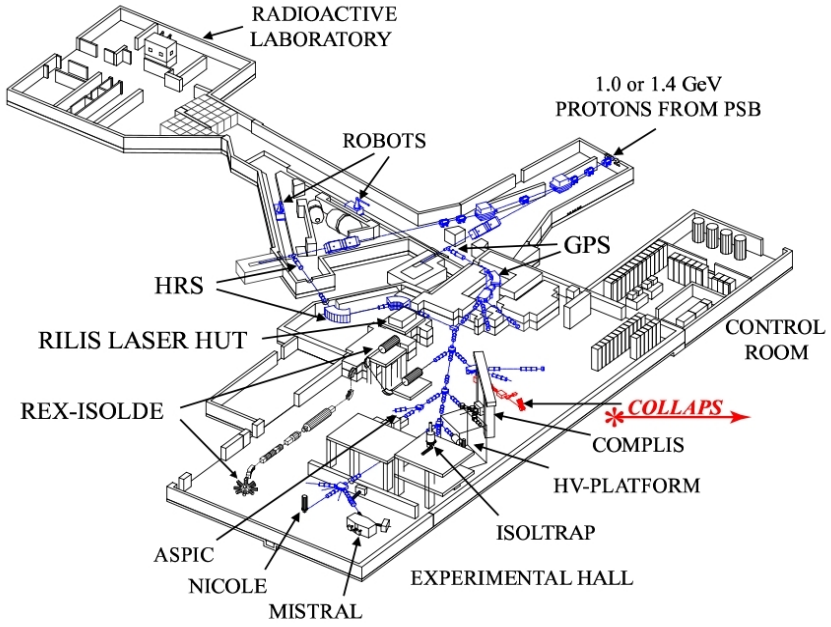

Figure 4.2: Layout of the ISOLDE hall, with the various experimental setups which are present the facility. The COLLAPS beam line is highlighted in red. Taken from [54].

The material used in the fabrication of the target units varies depending on what elements are to be investigated. There are three classes of materials employed: molten, metal powder or a metal foil. The thickness of the target varies from $50 - 200$ g/cm^2. The target temperatures range between $700 - 2000$ K. When the protons are delivered to the target unit, radioactive nuclei are produced by different reaction channels such as spallation, fission or fragmentation. The reaction products, which are in a gaseous form thermally diffuse out of the target due to temperature gradients. For a target unit equipped with a classical surface ion source, the radioactive vapour then effuses through a transfer line and a hot ionizer tube. The ionizer tube is coated with

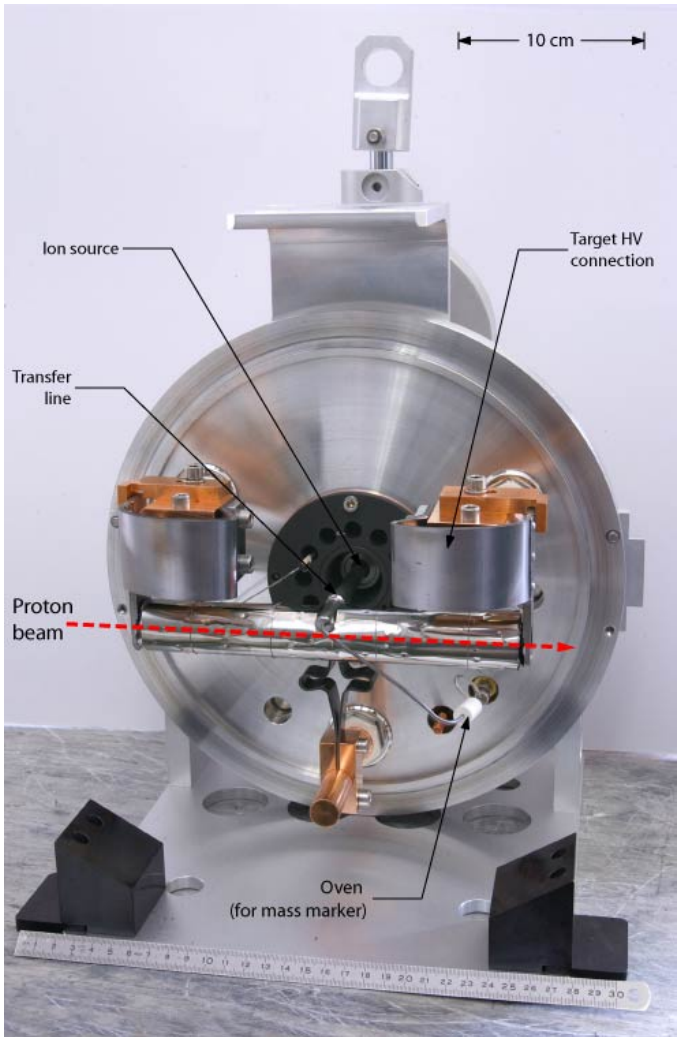

Figure 4.3: Picture of an ISOLDE target unit. Taken from [55].

a material with a low vapour pressure (e.g. : Ta, Mo, Nb). Depending on the ionization potential of the atom to be studied and on the work function of the material chosen for the ionizer, some degree of chemical selectivity can be achieved. In order to improve selectivity, photoionization can be used, depending on whether there are schemes available. A thorough discussion of these issues can be found in [55]. Following the ionization process, the single charged ions are accelerated electrostatically

by a voltage of up to 60 kV, mass separated and transported to a particular experiment by means of ion beam optics elements. Experience has shown that the extracting high voltage in the target area has to be applied asynchronous to the proton pulse to avoid electrical breakdown due to the ionization of air at the target front-end. The final yield has a quasi-continuous structure.

4.2 The COLLAPS beam line

The collinear laser spectroscopy (COLLAPS) beam line is shown schematically by Figure 4.4. The incoming ion beam enters the setup and is deflected by 10° by two capacitor plates. In order to optimize the transport downstream the beam line, the beam passes through ion optics shaping devices (not included in the Figure 4.4). The main part of the beam line is the post-acceleration region, where the Doppler-tuning of the ion beam occurs. This region is formed by four ring electrodes and a charge-exchange cell (CEC). The CEC, which is detailed in Figure 4.5, is a device filled with a hot alkali vapour. It serves to neutralize the incoming ions on a single pass. The next part of the beam line is the interaction region, where the beam on the atomic state is resonantly excited with the collinear laser. The photons from the fluorescence decay are counted by two photomultiplier tubes, positioned at 90° with respect to the beam axis. This fluorescence is imaged by a cylindrical reflector which is placed at the back of the light interaction region. Finally, there is a Brewster window mounted on a vacuum flange which closes the beam line. Its purpose is to minimize internal laser reflections which are a source of background.

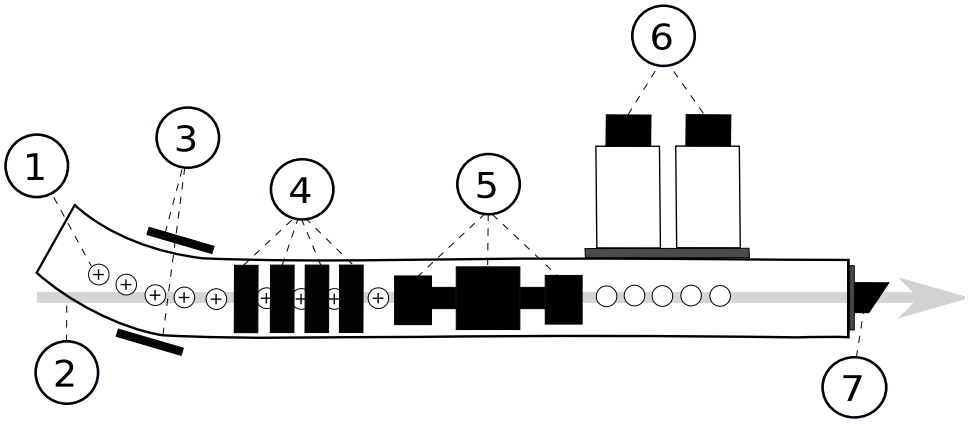

Figure 4.4: A simplified scheme of the collinear laser spectroscopy setup at ISOLDE. 1. Single charged ions; 2. Laser beam; 3. Electrostatic deflection plates; 4. Post-acceleration electrodes; 5. Charge-exchange cell (CEC); 6. Photomultiplier tubes; 7. Brewster window. The dimensions are not to scale.

The scanning voltages and the signal from the photomultiplier tubes are controlled by the "measurement and control program", MCP. The MCP is set to output scanning voltages between -10 V and 10 V, as shown by Figure 4.6. This voltage is then amplified by a factor of ~ 50 with a Kepco BOP 500M amplifier, and added to the high voltage of either of 3 independent Fluke power supplies. These power supplies can be electronically switched in order to facilitate scans covering a wide spectral range or across different mass regions. The scanning and Fluke voltages are connected to a 1000:1 voltage divider, which is read by a Prema 6040 digital voltmeter. The readout from the Prema divider is recorded by the MCP at the end of the scan.

In order to measure a hyperfine structure, an accelerating voltage range ΔV is defined for a given scanning region, as shown by 4.7. This region is divided into N "channels". Each channel collects photon counts during a fixed dwell time, which is typically $10-100$ ms. In principle, this cycle can be repeated many times, to improve

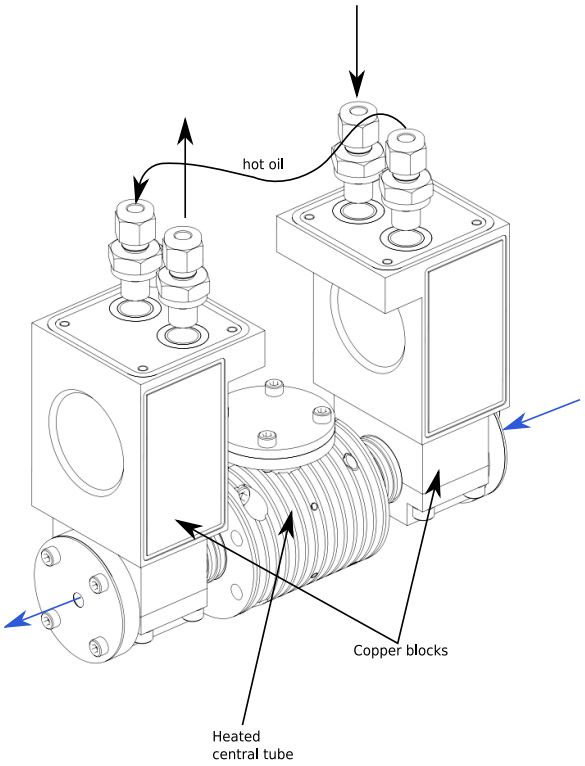

Figure 4.5: Technical drawing of the charge-exchange cell. The central part contains a solid piece of an alkali element. The blue arrows indicate the direction of the incoming and outgoing beams.

the statistics.

4.2.1 Data acquisition electronics

For the conventional photon detection technique used in COLLAPS, the signals from the photomultiplier tube are amplified and sent to a discriminator unit, for single photon counting. Under a certain threshold value set on this unit, the signal is not regarded as coming from a photon and is rejected. Otherwise the signal is counted by a scaler. For each channel, the output of the scaler is recored by the MCP program and reset. A schematic description of the data acquisition electronics is shown by Figure 4.8.

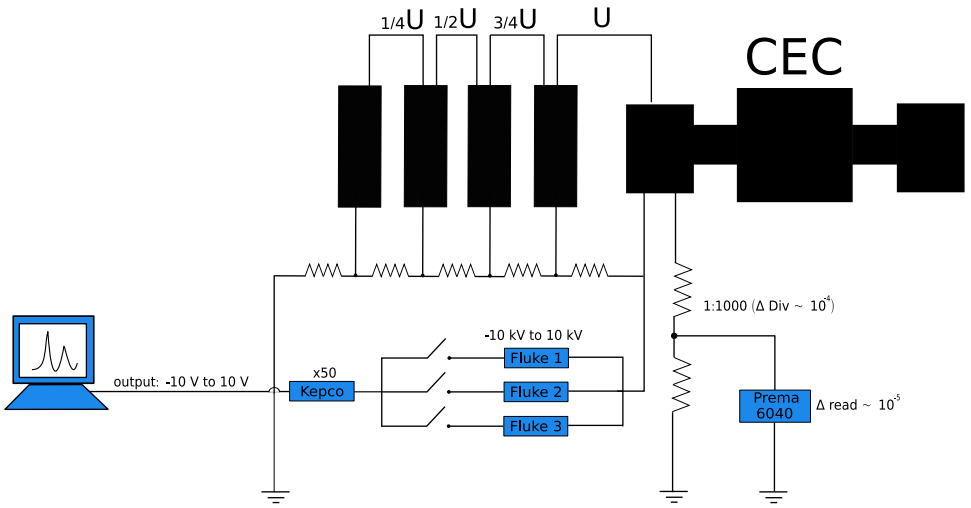

Figure 4.6: A simplified scheme of the scanning voltage applied to the post-acceleration electrodes and the charge-exchange cell.

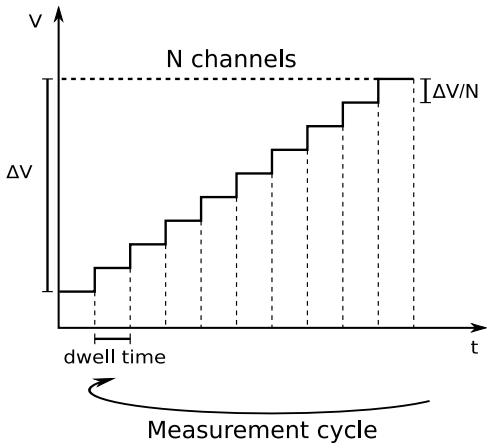

Figure 4.7: Scheme of the variation of the tuning voltages used in a hyperfine scan.

Collinear laser spectroscopy with the subsequent laser induced fluorescence detection has been successively applied to the study of several radioisotopes for the past 30 years [19]. However, with this technique it is difficult to significantly increase the detection efficiency without at the same time increasing the detection of the background due to continuous laser scatter from apertures and other components of the

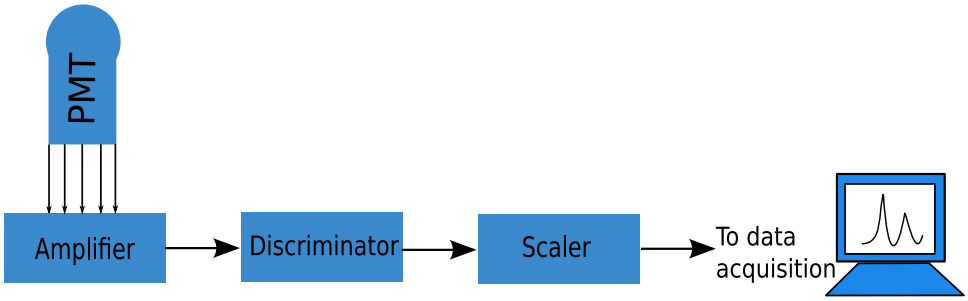

Figure 4.8: Schematic layout of the electronics used on a classical collinear laser experiment.

beam line. As a consequence, the minimum beam intensity required is typically of the order of 10^6 ions/s. On the other hand, with the advent of linear ion traps, an efficient way of suppressing laser background has been developed during the past few years. This technique is the bunched-beam spectroscopy [25], and allows measurements to be performed with ion fluxes as low as 50 ions/s. The technique was pioneered by the Manchester-Birmingham groups, which since the closure of Daresbury radioactive ion beam facility in the late 1990's, have been conducting their experimental programme primarily in Jyväskylä . Based on the expertise accumulated from the work in Finland, the group has promoted the development of a similar ion trap at ISOLDE and has been working in conjunction with the COLLAPS collaboration in order to implement the bunched-beam technique at ISOLDE.

4.3 The RFQ ion cooler and buncher - ISCOOL

A gas-filled linear Paul trap, ISCOOL, has been designed by Petersson [56] and Podadera [57] in order to reduce the ion beam transverse emittance and longitudinal en-

ergy spread, and deliver the beam as a continuous flux of particles, or accumulate and release the ion beam in short bunches with a definite time structure. Figure 4.9 depicts the device.

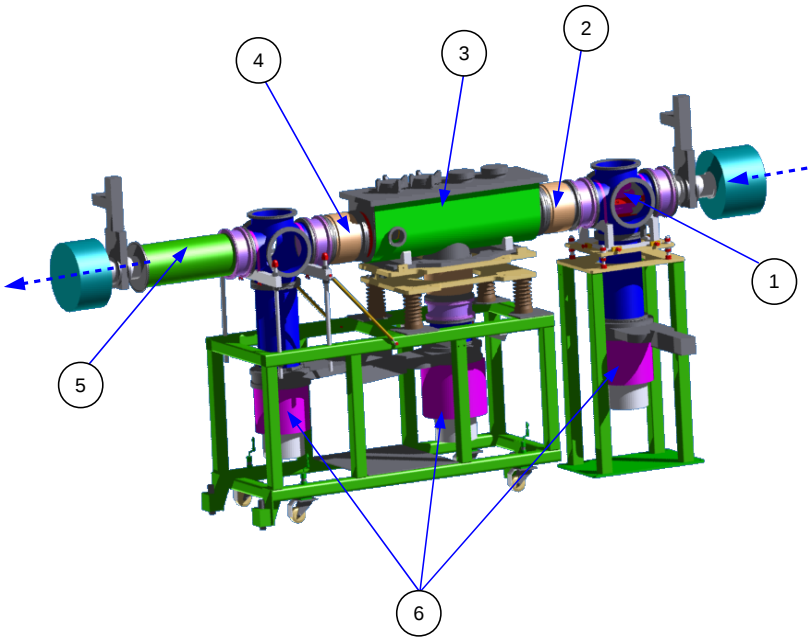

Figure 4.9: All the elements which composes the ISCOOL assembly: 1. Injection quadrupole triplet. 2. Injection optics. 3. Main trapping chamber. 4. Extraction optics. 5. Extraction quadrupole triplet. 6. Turbomolecular pumps. The dotted arrows indicate the direction of the incoming and outgoing beams.

During the initial design stages, several locations were considered for the installation of ISCOOL. Ideally, this device should be installed at the target area, between the target front-end and the separator magnets, because this would increase the mass resolving power of the separator magnets. However, this place would render several technical difficulties, the main one being due to radioprotection issues, considering that the target zone is a controlled radioactive area at ISOLDE. Therefore, on the final

design stages of ISCOOL, its location was decided to be on focal plane of the HRS separator, after the 60° magnet, as shown by Figure 4.10.

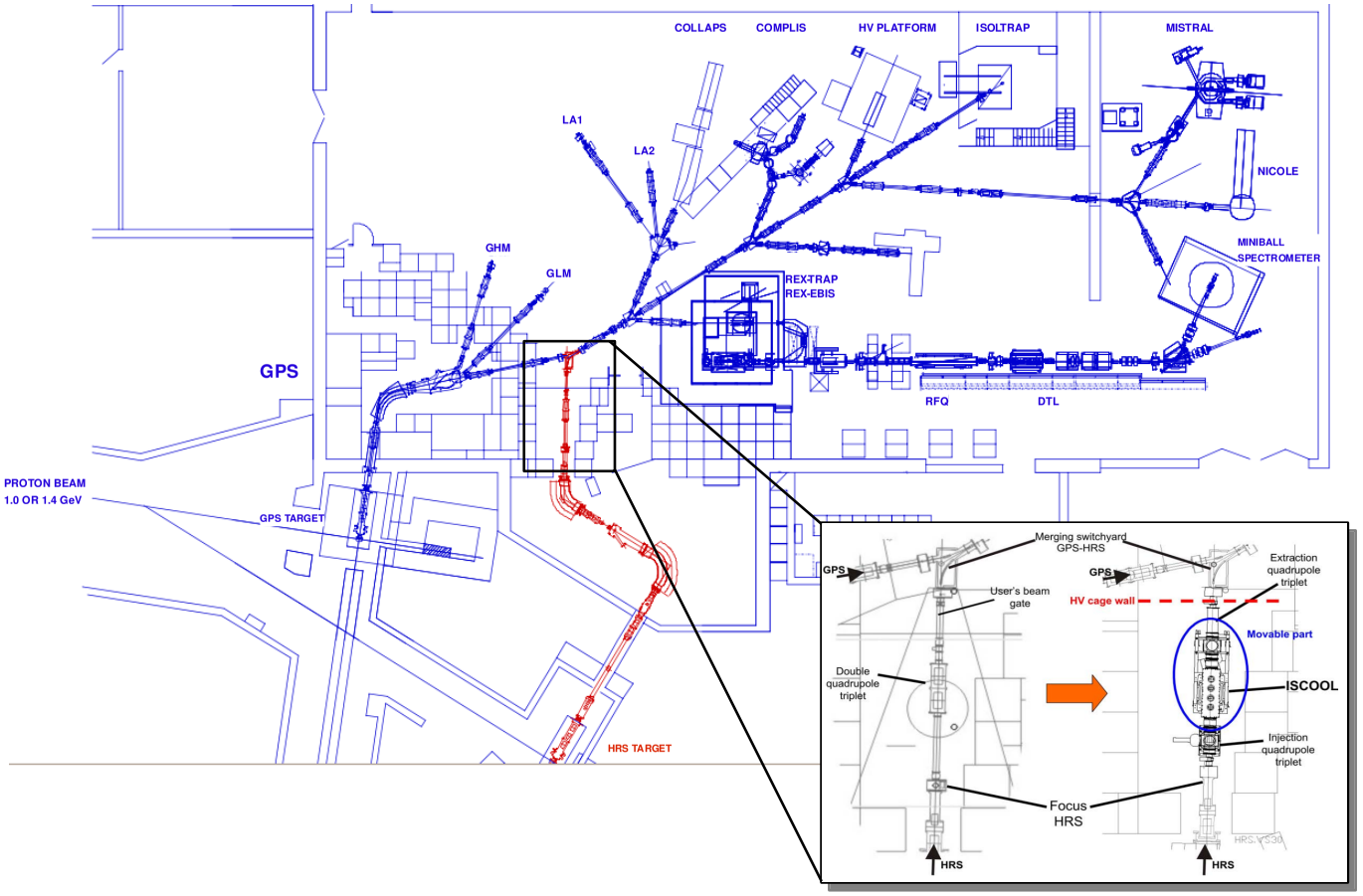

Figure 4.10: Layout of the ISOLDE hall. The red part shows the tagert area and the HRS separator magnets. The insert shows the location of ISCOOL in the facility. Adapted from [57].

ISCOOL was designed to be a general purpose ion guide in that it should be able to deliver cooled and bunched ions from a wide range of masses ($10 < A < 300$) to all the experiments located downstream the HRS beam line. Essentially, ISCOOL consists of injection electrodes, the radiofrequency quadrupole trap floating at high voltage, and extraction electrodes. The quadrupole structure is formed by four rods, coupled pairwise. The distance from the rods to the ion guide axis is r_0. To each pair of electrodes, a DC field and radiofrequency field with frequency ω and amplitude V is applied. A phase shift of 180° is maintained between the pairs. The arrangement is shown by Figure 4.11.

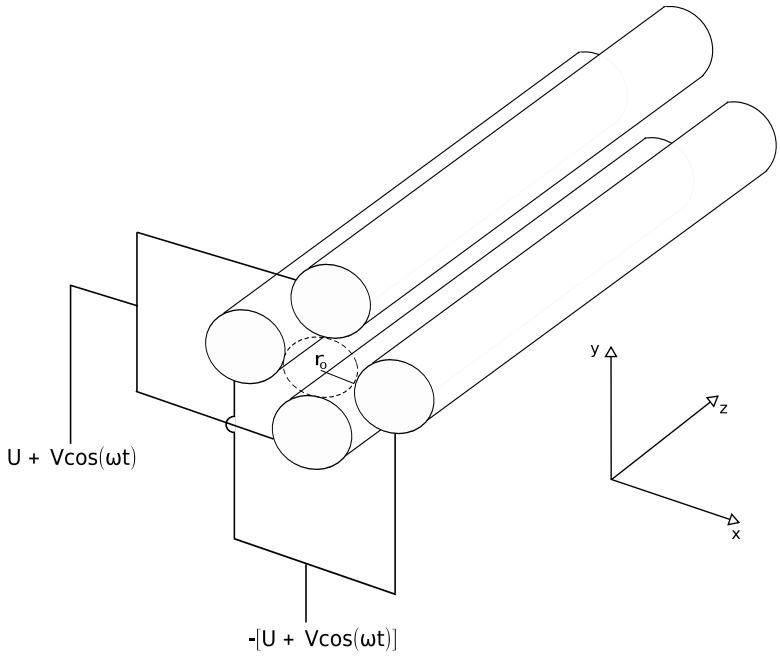

Figure 4.11: Simplified scheme of the ion trapping device.

The confining potential in the transverse plane, defined as (x, y) reads [58]:

$$\phi(x,y) = \frac{\phi_0}{r_0^2}(x^2 - y^2). \tag{4.1}$$

Equation 4.1 describes a hyperbolic paraboloid, commonly referred to as a "horse saddle" potential. The field lines in the $(x-y)$ plane are hyperbolae. The problem of particles confined in a time-varying quadrupolar field can be explained with a simple mechanical analogue - if a sphere is placed on the "saddle point" of a horse saddle, it would not remain stable for very long. However, if the saddle is rotated around the z axis, a dynamical feedback is created which maintains the sphere on the centre of the saddle. Analogously, if a static DC field were applied to the quadrupole structure, that would not provide a stable confinement, and therefore the ion cloud would escape the centre of the trap. On the other hand, the ion cloud does stay dynamically confined in the $(x-y)$ plane due to the radiofrequency field. For a potential of the form $\phi_0 = U + V\cos(\omega t)$, the equations of motion in x and y coordinates read:

$$\begin{cases} \frac{d^2x}{d\tau^2} + [a - 2q\cos(2\tau)]x = 0 \\ \\ \frac{d^2y}{d\tau^2} - [a + 2q\cos(2\tau)]y = 0 \end{cases} \tag{4.2}$$

The substitutions $\tau = \frac{\omega t}{2}$, $a = \frac{8eU}{mr_0^2\omega^2}$ and $q = \frac{4eV}{mr_0^2\omega^2}$ were made, where e is the ion charge, V is the DC voltage, U is the zero-to-peak radiofrequency voltage amplitude, m is the ion mass in atomic mass units, ω is the radiofrequency. The equations 4.2 for x and y are the canonical Mathieu's equations [59]. Since the radius r_0 (see Figure 4.11) is fixed (for ISCOOL, $r_0 = 20$ mm) and the beam is composed of single ionized ions, the

dimensionless parameters a and q are functions of the DC field, the radiofrequency and amplitude. For fixed values of the radiofrequency and amplitude the ions will develop a complicated oscillatory radial motion. It can be shown [60] that the stability of the solutions of the Mathieu's equation can be represented in terms of a diagram in the $a-q$ plane, shown by Figure 4.12. Outside the hatched regions in this diagram, the ions develop an unstable motion and eventually hit one of the electrodes and are lost.

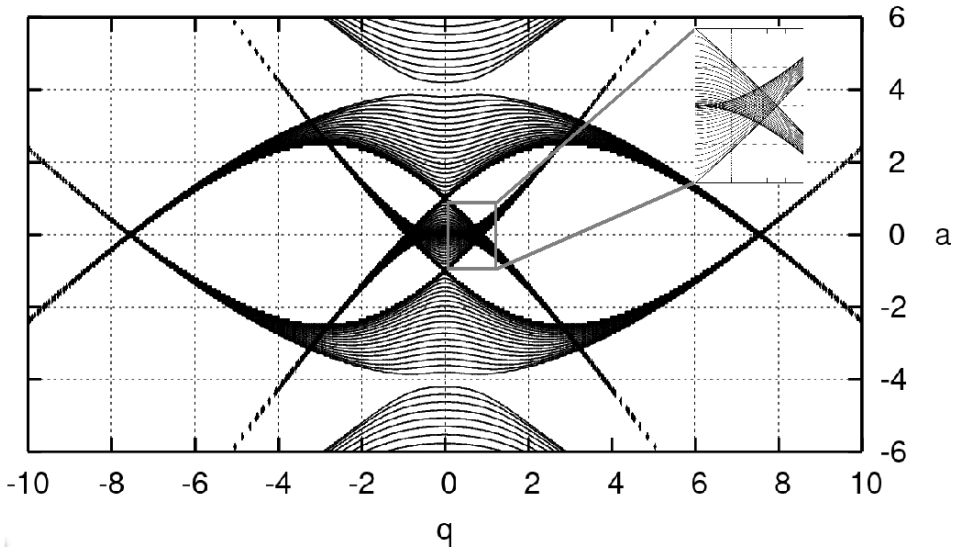

Figure 4.12: Single particle stability diagram for the $(x-y)$ plane. The inner figure shows in detail the expanded diagram, for $0 < q < 1.2$ and $-1 < a < 1$.

In reality, ISCOOL was designed so that the quadrupole rods pass through a series of 25 variable-width wedge electrode rings, insulated from each other by SiO, as shown by Figure 4.13. This allows the radiofrequency to be applied independently from the DC part of the potential. In addition, it is also possible to apply different DC voltages to each of the rings in order to create a potential gradient, which pushes the beam out of the trap more efficiently. A typical DC gradient for ISCOOL is 0.2 V/cm. The trap

can also accumulate the ions and release bunches. This is accomplished by applying a voltage on the end plate electrode, as shown in Figure 4.14.

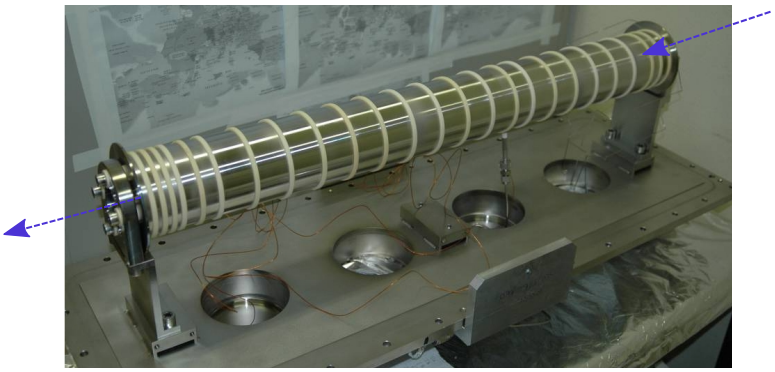

Figure 4.13: Picture of the trapping structure of ISCOOL superimposed by the 25 wedge electrodes. The direction of the incoming and outgoing beam is indicated by the blue arrows.

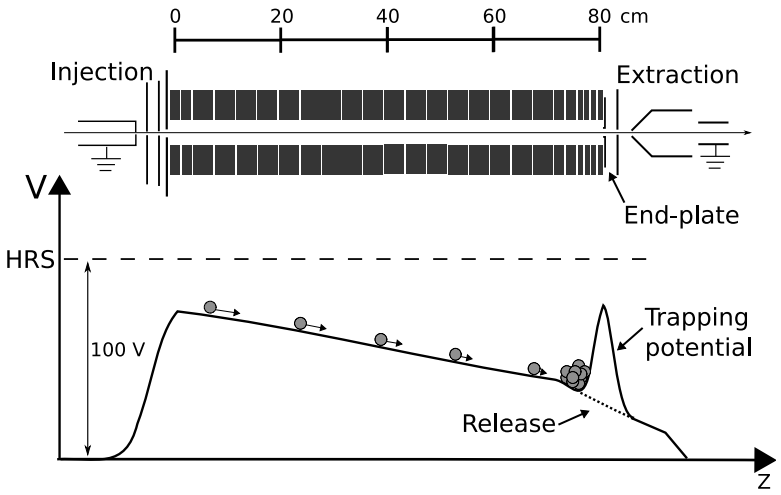

Figure 4.14: Diagram of the DC axial potential of ISCOOL.

In this configuration, the application of a trapping DC axial field generates a harmonic defocusing potential, as pointed out by Drewsen *et al.* [61]. In the region of axial confinement, the equations of motion are modified and so is the $a-q$ stability diagram.

For further discussion on this issue, see [62]. In continuous mode, Petersson [56] estimated that up to ~ 1 nA of current would be fairly concentrated around the optical axis (defined as z) and would be transmitted.

4.3.1 Phase space and ion cooling

In the Hamiltonian formulation of classical mechanics, a particle's dynamics in three dimensions is described by its position $q = (x, y, z)$ and its conjugate momentum $p = (p_x, p_y, p_z)$. These variables form a six-dimensional *phase space*, and each point of this space will describe the state of the particle. The state of a collection of N particles will be characterized by $6N$ variables. For a system with a large number of particles, it becomes difficult to book-keep the state of each particle. Alternatively, these particles are usually treated as an ensemble. As a consequence, it is the gross properties of the ensemble as opposed to of individual particles which will be of interest.

4.3.1.1 Emittance and Acceptance

The positions and momenta of all the ions in an ensemble occupy a volume in the six-dimensional phase space, formed by $\{q_x, q_y, q_z, p_x, p_y, p_z\}$ coordinates. If the ion motion is decoupled in the three directions of space, which means that the equations of motion for each coordinate have only linear terms in the force fields, then this volume can be projected into subspaces for each pair of canonical coordinates (q_i, p_i) [63]. The projection will occupy an area S_i, which is known as an *action diagram*, S_i, expressed as:

$$S_i = \int\int dq_i dp_i. \tag{4.3}$$

The action diagram S_i is defined as an emittance when the contour of the action diagram can be represented by an ellipse. In the case of a beam propagating with the optical axis in the the z direction, there is one longitudinal emittance and two transverse emittances. The longitudinal emittance would be defined as $\varepsilon_z = zp_z$. However, since z is the direction the beam propagates, an alternative definition of emittance is used [62], which takes into account the spread in energy and time. Therefore $\varepsilon_z = \Delta E \times \Delta t$. It only makes sense to use this definition for bunched beams. Typical bunching times for ion traps are of the order of μs, therefore the unit for longitudinal emittance is expressed as [eV. μs]. The transverse emittances either in x or in y coordinates can be generally represented according to Figure 4.15. It shows an ellipse in two systems of coordinates, rotated by an angle θ. In the x, y coordinates, the equation of the ellipse can be written as:

$$\begin{pmatrix} x & y \end{pmatrix} \underbrace{\begin{pmatrix} C_T & A_T \\ A_T & B_T \end{pmatrix}}_{T} \begin{pmatrix} x \\ y \end{pmatrix} = \varepsilon, \tag{4.4}$$

where ε is the eccentricity of the ellipse. A_T, B_T, and C_T are the Twiss parameters, which read [64]

$$\begin{aligned} A_T &= (l_a/l_b - l_b/l_a)\sin\theta\cos\theta \\ B_T &= (l_b/l_a)\sin^2\theta + (l_a/l_b)\cos^2\theta \\ C_T &= (l_a/l_b)\sin^2\theta + (l_b/l_a)\cos^2\theta \end{aligned} \tag{4.5}$$

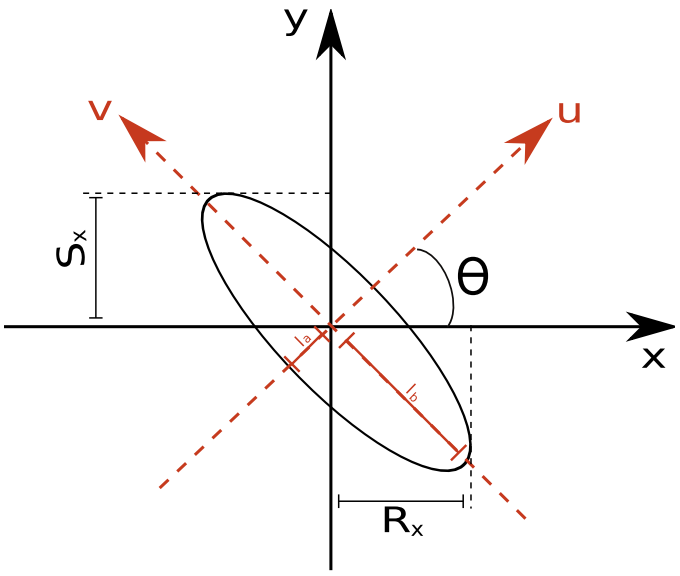

Figure 4.15: Representation of an ellipse in an arbitrary system of coordinates rotated by an angle θ with respect to the x, y plane. Adapted from [64].

It can be shown that the combination of these parameters for any given θ is

$$B_T C_T - A_T^2 = 1. \tag{4.6}$$

The equation of the ellipse in the coordinates defined by the eigenvectors u and v, and the eigenvalues λ_1 and λ_2 of the Twiss matrix T is:

$$\left(\frac{u}{l_b}\right)^2 + \left(\frac{v}{l_a}\right)^2 = 1,$$

where $l_a = \sqrt{\varepsilon/\lambda_2}$ and $l_b = \sqrt{\varepsilon/\lambda_1}$. In this basis, the area of the ellipse is $\pi l_a l_b = \frac{\pi\varepsilon}{\sqrt{\lambda_1\lambda_2}} = \frac{\pi\varepsilon}{\sqrt{detT}}$. The condition 4.6

$$\det T = C_T B_T - A_T^2 = 1,$$

implies that the area of the ellipse $A_e = \pi\varepsilon$. The transverse emittance diagram can be plotted in two ways. One way is by using the canonical displacement-momentum variables (x,p_x). Another way would be to use the (x, x') pair, where x' is an angle. Figure 4.16 shows graphically the basic relation $x' = p_x/p_z$. If the transverse emittance is represented in (x,x') coordinates, then the emittance is said to be non-normalized. This means that whenever the beam energy is changed, the longitudinal momentum will also change, therefore, the angle x' will change. The unit of the non-normalized emittance is [mm.mrad]. However, it is conventioned to present the emittance as [π mm.mrad]. Since (x,x') are not conjugated coordinates, care must be taken in order to always be clear about what is the beam energy for that particular non-normalized emittance. An emittance ε_1 measured at a fixed energy E_1 can be related to an emittance ε_2 measured at a different energy E_2 by [57]

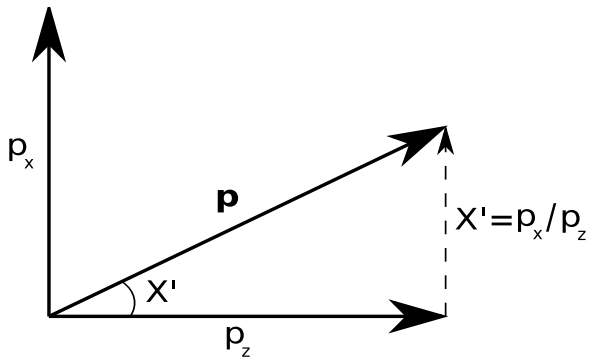

Figure 4.16: Decomposition of the momentum **p** in the p_x, p_z components. The angle x' represents the beam divergence with respect to the beam with central momentum at p_z.

$$\varepsilon_2 = \varepsilon_1 \sqrt{\frac{E_1}{E_2}}. \tag{4.7}$$

From this expression, it is clear that the higher the energy, the smaller the emittance. If the emittance is calculated in the canonical representation (x, p_x), the emittance is said to be normalised. In this case, the units are [mm^2/s]. Because of the relation in Figure 4.16, it is always possible to recover the normalized emittance from the non-normalized emittance and vice-versa. In practical terms emittances are often measured as displacement-angle diagram accompanied by the beam energy. The emittance of an ISOLDE beam will depend on the combination of target-ion source, but is about 35π mm.mrad [65]. It can be physically understood with the help of Figure 4.17. ISCOOL was designed to deliver beam with a transverse emittance of 3 πmm·mrad at 60 keV.

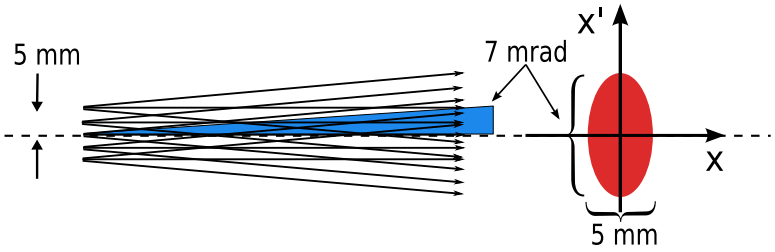

Figure 4.17: Geometrical representation of a typical emittance of a beam produced at ISOLDE.

It is not always true that shape of the action diagram is elliptical. According to Fong [66], the elliptical shape of the emittance will only be preserved if the motion of each coordinate is independent. For ions travelling in a perfect quadruple field this is the case. However, due to imperfections in the fabrication of quadrupole rods, high order terms in the electric field are introduced, and non-linear forces will couple the coordinates and therefore will induce aberrations. These aberrations will distort the elliptical shape of the emittance diagram, and may compromise the beam quality.

For any ion optics device, the system may accept a collection of ions with or without losses. This *acceptance* is therefore related to the geometry and fields applied to an ion optics system, in order to exactly match each of the action diagrams in the phase space so that the ion beam may be fully transmitted [67]. The acceptance and emittance have the same units. Therefore, only a fraction of the ion beam with an emittance bigger than the acceptance of the device will be transmitted. The rest will get lost by various mechanisms. For instance, the ions can hit the electrodes and get lost. Moreover, as Dezfuli pointed out [63], matching the area of the action diagrams with the acceptance is a necessary, but not a sufficient condition for a perfect transmission; The *shape* of the ellipse should also match the shape of the acceptance of the optical system. The latter condition can in principle be achieved by employing linear focusing elements, such as a quadrupole lens.

4.3.1.2 Liouville theorem

In the active view of a canonical transformation [68], the time evolution of a collection of N particles in the phase space is regarded as a mapping of the $6N$ canonical coordinates into the same phase space. Figure 4.18 shows a point characterized by its position and momentum vectors $(\mathbf{q}, \mathbf{p})$. The Figure also shows the vicinity of the point, which is represented by the dotted circles. The solid and dotted lines enclose the two volumes of particles in the phase space. They are connected by the solid arrow, which takes the ensemble from a given time t_1 to a time t_2. The Liouville theorem states that for conservative systems, the local density of a cloud of non-interacting particles does

not change as the ensemble evolves with time [67]. In other words, the density of a collection of particles in the phase space behaves as an incompressible fluid [69], and can only be reduced by means of dissipative forces. In the case of interacting particles, Liouville theorem will only hold valid for a gas of particles in thermal equilibrium [69].

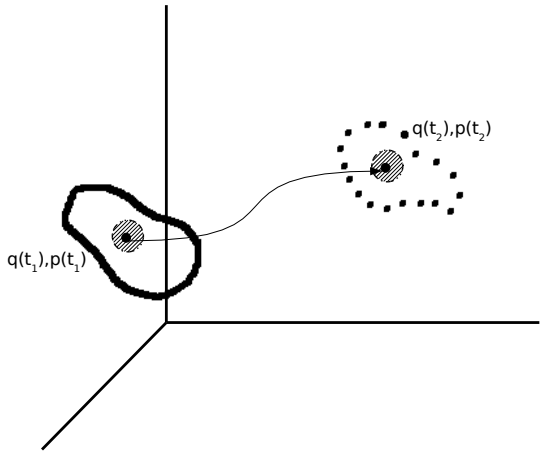

Figure 4.18: Active representation of a canonical transformation. Adapted from [68].

Since the ISOLDE facility provides a plethora of radioactive species, it makes sense to employ a cooling method which is fast, universal and chemistry independent. For ISCOOL, buffer gas cooling was the method chosen, owing to the quick cooling times involved, and the relatively simple implementation. It should be noted, however, that many other powerful methods of ion cooling exist. Laser cooling is a good example, which is based on the directional loss of momentum of an atom after laser absorption and isotropic emission. With this technique it is possible to cool atoms down to $<$ mK.

The only drawback of this technique is that it is limited to a few atomic species. For a comprehensive review of alternative methods of ion cooling, see for instance [70].

4.3.2 Buffer gas cooling

Major and Dehmelt [71] were the first to examine the effect of the ion motion in a background neutral gas in a conventional Paul trap. Their model disregarded ion-ion collisions and was mainly based on the assumption that the ions suffered elastic collisions with the neutral gas. They found out that the collision process would result in a viscous drag caused by the background gas and the ion motion would be damped exponentially. The next important contribution that followed was the work of Douglas and French [72], who reported that filling a linear radiofrequency quadrupole trap with a buffer gas improves the transmission of the ions injected. They called this effect "collisional focusing". Following the work of Douglas and French, Kim [69] made a detailed study based on Monte Carlo approach on the the effect of buffer gas cooling and the statistical properties of the cooled beam. Monte Carlo simulations such as the one performed by Jokinen *et al.* [73], are useful to understand the process of gas cooling at ISCOOL. A more detailed account on how these simulations were performed can be found in [56].

In the treatment of buffer gas cooling, the charged particles and the neutral buffer gas occupy a volume which is permeated with a homogeneous electric field. The thermal collisions between the buffer gas and the ions are isotropic. Since there is a directional electric field **E**, the ions on average gain momentum and drift in the direction

of the field with a velocity $\mathbf{v}_d$. The *ion mobility* K is defined [74] as the constant of proportionality between $\mathbf{v}_d$ and $\mathbf{E}$. In equilibrium, the force in the direction of the field will be the same as the dissipative force, and therefore

$$\mathbf{F}_d = -\frac{e}{K}\mathbf{v}_d. \tag{4.8}$$

This velocity dependent dragging force modifies the equations of motion 4.2 to:

$$\begin{cases} \frac{d^2x}{d\tau^2} + b\frac{dx}{d\tau} + [a - 2q\cos(2\tau)]x = 0 \\ \\ \frac{d^2y}{d\tau^2} + b\frac{dy}{d\tau} - [a + 2q\cos(2\tau)]y = 0, \end{cases} \tag{4.9}$$

where $b = e/Km$. A change of the kind $x(t) = x'(t)e^{-\frac{b}{2}t}$ for the x and y coordinates transforms the set of differential equations for the respective coordinates back into the canonical Mathieu equations, now for x' and y' variables, and the a parameter changed into a' such that $a' = a - b^2/4$. As Dawson [58] pointed out, the damping force induced by the presence of a buffer gas can be seen as enlarging the area of stability in the $a-q$ diagram.

In order to quantitatively determine the effect of gas cooling on the motion of the ions, it is important to know the ion mobility. For the microscopic determination of K, it is necessary to develop a rigorous statistical treatment of the loss of momentum during collisions between the ions and the buffer gas, and even between the ions themselves. Lunney and Moore [75] have carried out a numerical integration method considering the damping as a viscous force caused by hard sphere collisions. For the

low energy region ($E < 1$eV), one can find data on ion reduced mobility in the literature. For the $E > 1$ eV, the hard sphere collision model gives the equivalent mobility:

$$K = \frac{2e}{M}\frac{(M+m)^2}{Mm}\frac{1}{n\sigma\nu}. \tag{4.10}$$

where m is the mass of the buffer gas, M is the mass of the ions, n is the gas density, σ is the elastic collision cross section, and ν is the ion velocity.

An important feature of the microscopic approach is that it reproduces a phenomenon called rf-heating. It is based on the fact that during ion-gas collisions, the transfer of momentum generates an increase in the amplitude of the ion oscillations and eventually the ion hits the electrodes and gets lost. This is the dominating effect when the mass of the ion is of the same order of the mass of the buffer gas. Therefore, lighter ions would not be efficiently transmitted with this method of cooling. This is the main reason that for gas-filled ion beam coolers, He or H are often chosen as the buffer gas.

CHAPTER 5

THE ISCOOL OFF-LINE COMMISSIONING

5.1 Introduction

Prior to the installation of ISCOOL at the focal plane of the HRS, it was decided by the ISOLDE technical committee that tests with the device should be performed at an off-line test bench. During these tests, the conditions of operation of ISCOOL were investigated under scenarios similar to the operating conditions of an ISOLDE beam line element. The requirements set by the committee concerned the efficiency and quality of the beam transport through the device, and were based on the design specifications of Podadera [57]. These requirements are listed below:

- Greater than 70% transmission for Cs and K and greater than 20% for Li in continuous mode;
- Stable transmission without losses for up to 1 nA of current;
- Transverse emittance less than 3π mm.mrad at 60 keV;
- Longitudinal emittance less than 1 μs bunches with an energy spread of 1 eV at

60 keV for all ion sources.

The whole test bench was enclosed by a Faraday cage because the pilot studies with ISCOOL were performed in high voltage. The off-line set-up comprised the ion source, injection optics, the cooler and beam diagnostics. For the diagnostics, Faraday cups, emittance meters and a Micro Channel Plate were used. During the off-line tests the ions were extracted from the ion source with energies ranging from 30 to 60 keV. An assessment of the electronics and vacuum system was also undertaken. These investigations were essential in order to set the limits of the parameters necessary for the efficient and reliable operation of the device. For instance, the optimal gas pressure as well as the DC and radiofrequency fields needed for cooling and transmission of the ions in continuous mode were established. These tests took place from September 2005, when the author of this thesis started the Ph.D. course and was involved in the building, testing and parallel developments which comprised the off-line commissioning of ISCOOL. This phase lasted until June 2007 and demonstrated that the device met most of the the requirements for installation. This chapter is dedicated to the description of the setting up of the test bench and the results obtained from the investigations. These results, and preliminary investigations of the transmission in bunched mode were reported in [76].

5.2 Tools for diagnostics

For the assessment of ISCOOL performance, several ion beam detectors were employed during the device commissioning. Faraday cups were used to measure the

transmission efficiency of the device in continuous mode. The emittance meter was used to measure the transverse emittance. The Micro Channel Plate detector was used to measure the bunch widths and energy spread.

Faraday cups

A Faraday cup consists of a metal plate usually placed in a cylinder. The ions hit the interior of the cup and induce an electron current. The output of the Faraday cups was connected to a Keithley picoammeter, model 485. There is a correspondence with the number of ions and the electron current produced. Two Faraday cups were used for the off-line tests. One was placed in a beam diagnostic box, anterior to the ion source. The second Faraday cup was connected on the other extremity of ISCOOL. To avoid the escape of secondary electrons, -200 V was applied in front of the cups, causing a 2-fold suppression on the current generated by the secondary electrons. The suppression voltage was provided by a FUG HCN 7EM-2000 negative polarity power supply. The Faraday cups could be moved in and out with a compressed air outlet, controlled manually by a 24V switch place outside the cage. With this arrangement, it was possible to measure the transmission efficiency $\eta(\%)$ between the ion current measured before (I_b) and after (I_a) the trap,

$$\eta(\%) = \frac{I_a}{I_b} \times 100. \tag{5.1}$$

Emittance meters

Two emittance meters were used. One developed at Orsay, and a commercial apparatus. Figure 5.1 shows the two devices used for the emittance measurements. Both devices are based on the same principle, but differ in the design.

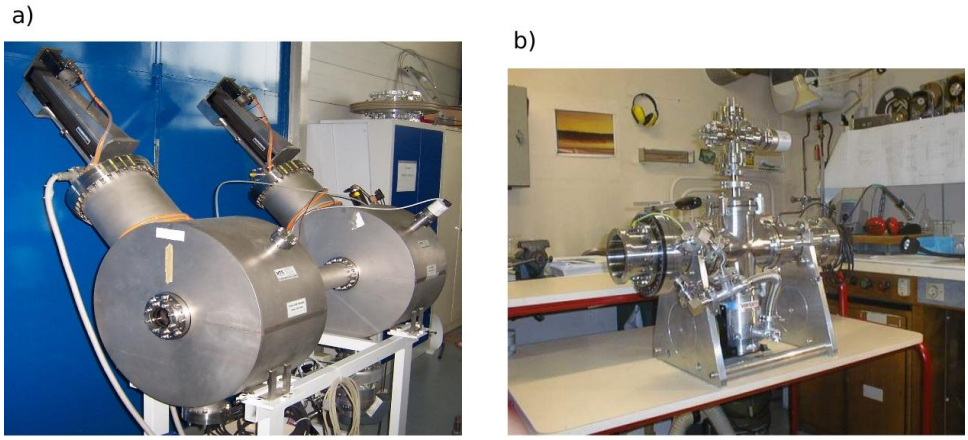

Figure 5.1: In picture a) the commercial emittance meter from ISOLDE, in b) the emittance meter from Orsay.

The emittance meter from Orsay is based on electrostatic deflectors, as described in [77], and shown in Figure 5.2. By varying $V1$ and $V2$ stepwise, the data acquisition records the ion current from an electron multiplier positioned at the back of the deflectors (not shown in the figure). The ion current is measured as a function of the displacement x (mm) and the angular divergence x' (mrad). This device could also be rotated by 90°, thus providing emittance information of the $y - y'$ plane. The emittance meter from Orsay only operates with small currents (< 100 pA) due to the limitations in the electron multiplier used for the current measurements.

The emittance meter from ISOLDE was developed by NTG Neue Technologien

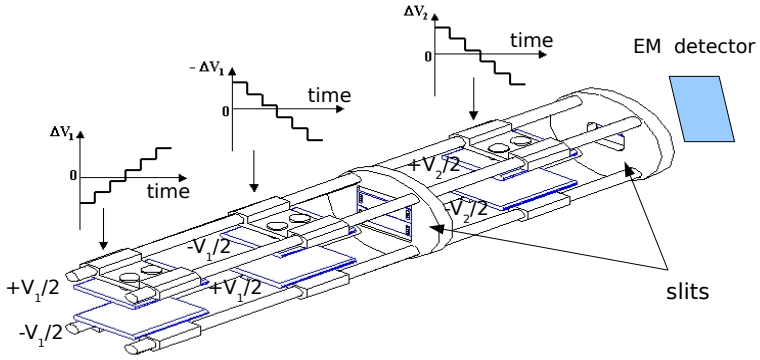

Figure 5.2: Principle of operation of the emittance meter from Orsay. The voltages V_1 and V_2 are applied to the plates indicated in blue. Adapted from [77].

and purchased by the ISOLDE collaboration. This emittance meter is a purely mechanical device based on the slit-harp principle [78], as illustrated by Figure 5.3. The "harp" is made of metal wires and the ion current, I, is measured as the harp is moved in the vertical direction. The slit and harp are positioned parallel to each other, and are controlled by linear stepping motors. This device is able to measure nA of current.

Micro Channel Plate

In addition to the Faraday cups and emittance meters, a Micro Channel Plate (MCP) detector was also used during the off-line tests. This device was necessary in order to characterize the ion bunches and to investigate the cooling times. An MCP is ba-

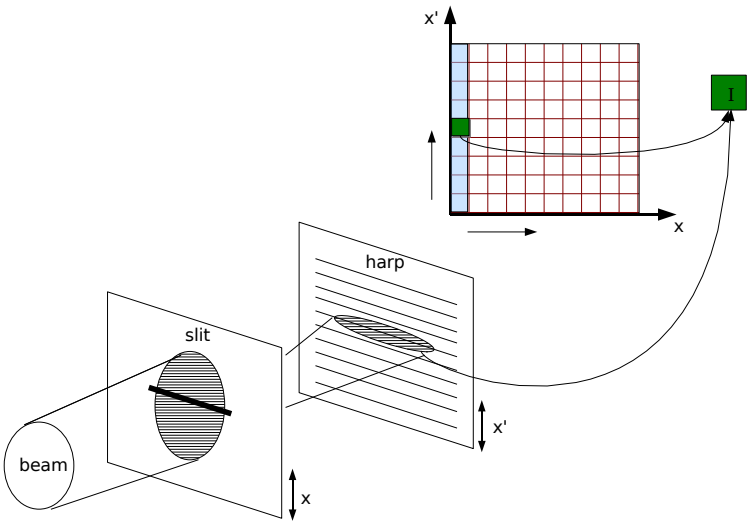

Figure 5.3: Principle of operation of the emittance meter from ISOLDE, based on the slit-harp principle [78].

sically a matrix of small electron multiplier tubes arranged uniformly parallel to each other. Each tube is a channel whereby secondary emission from the charged particle is stimulated. This device is directly sensitive to single charged particles and is suitable for measurements of time-of-flight. The MCP used was from El-Mul Technologies, model B025JA. It is a 25 mm diameter single MCP with an anode as read out. Because of the relatively high currents used for the tests, which could easy damage or saturate the MCP, attenuation grids were put in front of the device. The grids consisted of a 0.2 mm thick metal etched mesh, with holes of 0.1778 mm diameter, with an orientation of 60%, providing 91% attenuation, as specified by the manufacturer. These attenuation grids were mounted on two plates which were connected to a linear vacuum feedthrough. This arrangement offered three positions for different modes of

transmission: 100% (no attenuation), 9% when one grid is used and 1%transmission when the two grids are parallel. Both plates were floating at ISCOOL high voltage (30 kV). The back plate was connected to a positive high voltage supply in order to make it possible to measure the energy spread of the beam after re-acceleration, by measuring the variation of the ion beam current as a function of a positive bias applied between the plates. The detector set-up was mounted on a DN200 flange as shown in Figure 5.4.

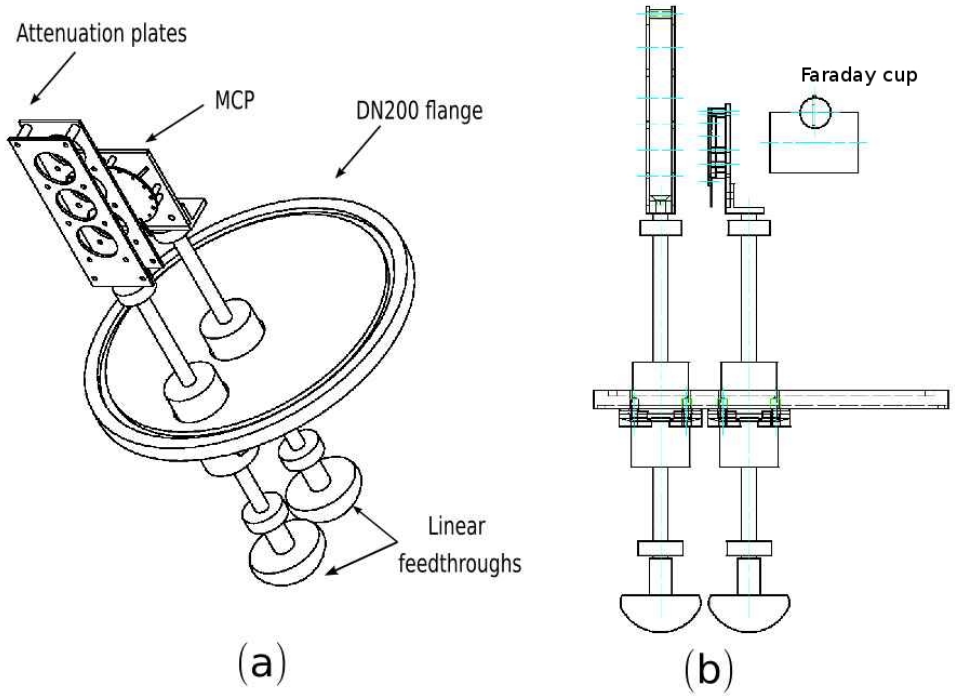

Figure 5.4: Technical drawing of the MCP and attenuation grids. In (a), a three dimensional view of the setup, and in (b), the side view.

The electrical connections of the MCP detector are shown in the Figure 5.5. A voltage of +1000 V is applied at the anode for the amplification with a CAEN HV power supply, model N470. The whole assembly was then placed on top the side of a

cross piece chamber as shown in Figure 5.6.

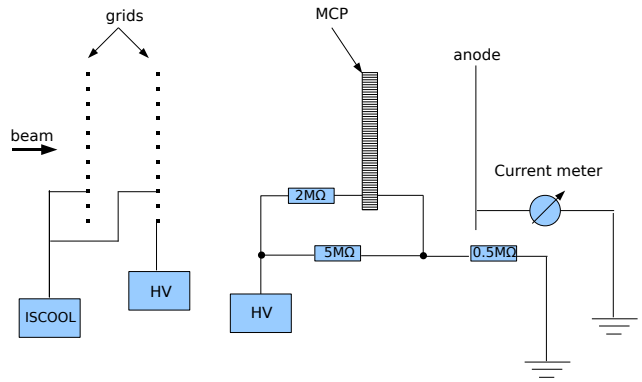

Figure 5.5: Scheme of the MCP electrical connection. The high voltage was supplied by a CAEN HV power supply, model N470.

5.3 First tests

Stable ions of ^{6}Li, ^{23}Na, ^{39}K, ^{133}Cs were used in the initial stage of the ISCOOL commissioning. Although these elements have the same chemical properties, and therefore would not give much information on the different chemical processes which might take place inside the trap, they covered a convenient mass range and therefore would give important information concerning the mass dependence of the transmission efficiency through the trap.

Surface ion source

The ion source used was a commercial Heat Wave model 101139 [79]. Separate pellets were used for different elements. The ion source pellet consisted of a fused mixture

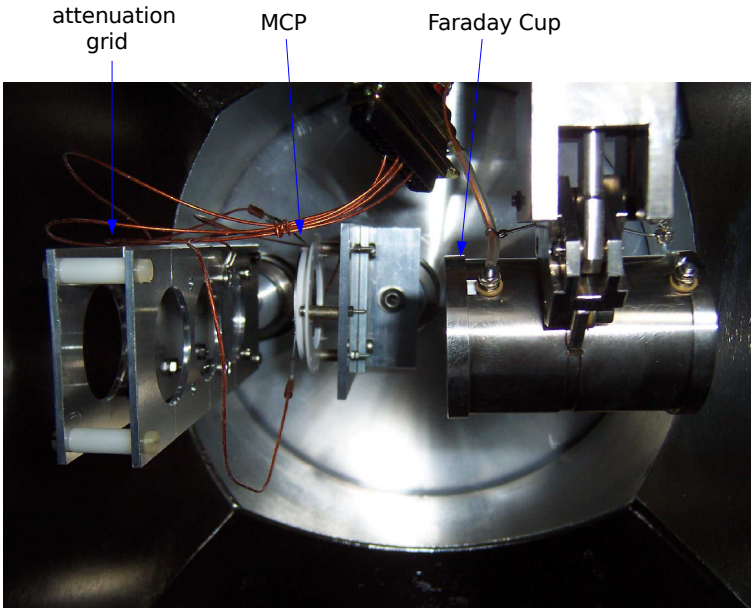

Figure 5.6: Installation of the MCP at the cross piece chamber.

of the sample and a porous matrix of aluminosilicate. The compound was held by a container made of molybdenum. The whole structure was supported by three rhenium legs. The heater was a molybdenum coil, welded together with the compound. The diameter of the ion source was 6 mm. Typical temperatures of $950-1100\,^{\circ}$C were sufficient for releasing the singly charged ions. The ion source was heated with a Delta Elektronika ES $030-5$ power supply and was connected to the ion source as shown in Figure 5.7. A bias voltage could be applied to the Delta supply, as indicated in the figure. The power supply was limited in voltage. Typical heating current of 1.8 A in voltage limited mode ($4-5$ V) produced ion currents of a few nA.

The extraction optics consisted of an ion gun, where the ion source was placed,

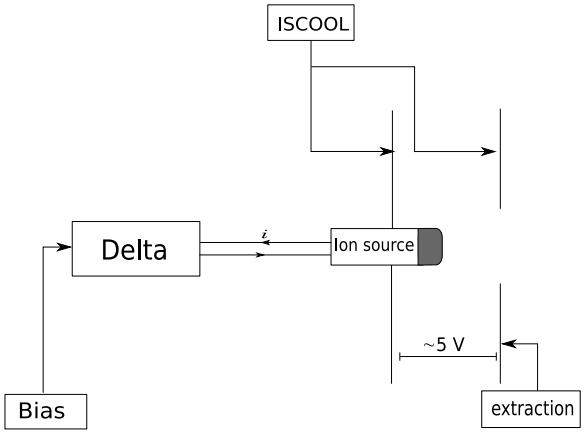

Figure 5.7: Illustration of the surface ion source connections with the delta power supply.

according to the set-up shown in Figure 5.8. In the ion gun there were five electrostatic elements: a bias voltage which was added to the high tension through the Delta supply; an extraction voltage; two Einzel lenses and a set of x, y steering voltages. The structure was mounted on a DN160 - ISO CF flange. The electrodes were powered with a CAEN High Voltage power supply model N126. The ions leaving the gun were initially assumed to have transverse emittance of about 10π mm.mrad, although measurements performed during the off-line commissioning indicated that the emittance was actually 35π mm.mrad.

During the first tests with the surface ion source, low ($< 0.5\%$) transmission efficiencies were measured. The most reasonable explanation for such low transmission efficiency was due to the inappropriate ion source and optics, such that the ions were not being efficiently injected into the cooler. The ion beam had to travel 1 m in a field-free region before entering the trap. Under these conditions, where there was no well-defined potential, the ion beam naturally diverged, causing severe losses. A num-

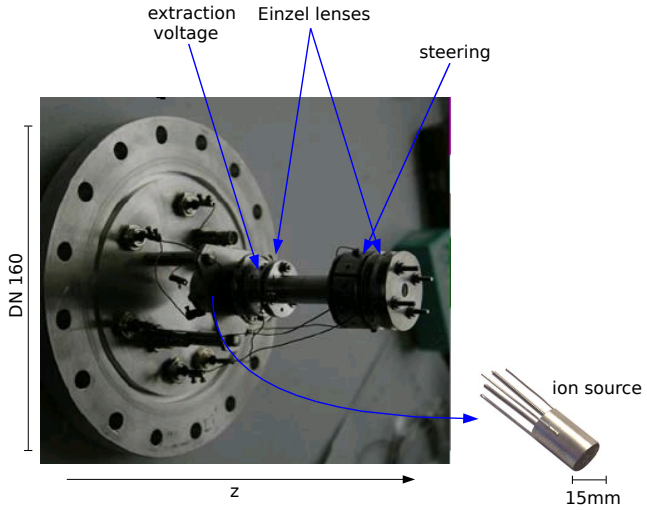

Figure 5.8: Ion gun from the "Laboratoire de Physique Corpusculaire", IN2P3-Caen (LPC).

ber of ideas were tested in order to improve the injection conditions at the entrance of the trap, including the introduction of extra lensing optics placed after the ion source. These arrangements only marginally improved the transmission efficiency through the trap. The maximum transmission efficiency achieved was of about 5% for $^{133}Cs^{+}$. In order to quantify the losses, two consecutive Faraday cups were placed before the cooler, as shown in Figure 5.9. The ion current was measured with Faraday cups connected to a Keithley picoammeter. The result of this test showed that $4/5$ of the beam was lost half-way between the ion source and the trap entrance, which suggested the urgent need of more focusing elements. The installation of an injection quadrupole triplet for the off-line test bench had already been foreseen, but during this first stage of the off-line commissioning it was still missing.

The quadrupole triplet consisted of three sections of electric quadrupoles. In the

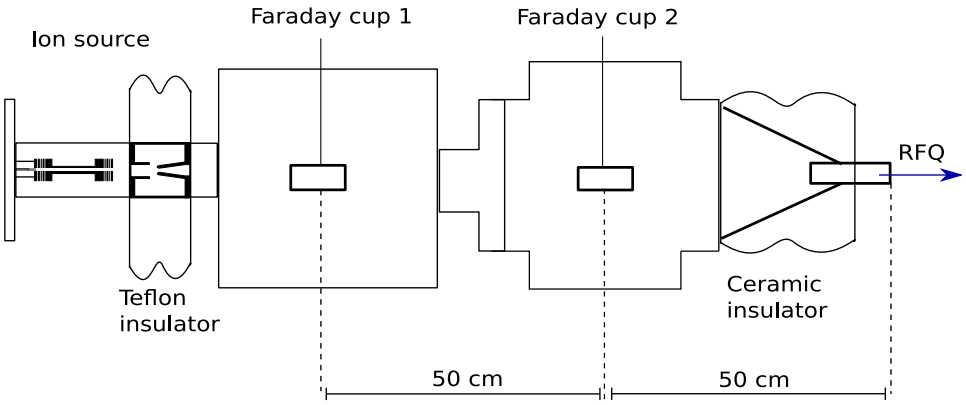

Figure 5.9: Scheme of the test intended to understand the poor extraction conditions of the LPC ion source.

first section of the triplet, the rods up and down were coupled together with positive polarity and left and right also coupled together, but with negative polarity. The same order of polarity was applied to the third sector. For the second sector, in order to avoid over-stretching the ion beam in one direction, the rods had the polarities switched. Since misalignment could cause large asymmetries in the fields, the voltages applied on the second section the electrodes were decoupled. A simulation of the beam trajectory was carried out for the stages covered during the off-line commissioning using SIMION 3D [80]. Figure 5.10 compares the results. The bottom picture shows the configuration of the first attempts to inject the beams into the cooler. The middle picture shows a relative improvement in the injection optics towards the cooler after the extra lens was included, whereas the top picture shows the injection optics set-up including the injection quadrupole triplet.

Therefore, the injection quadrupole triplet was essential for the continuation of the tests. Figure 5.11 shows the installation of the device. CAEN power supplies, model

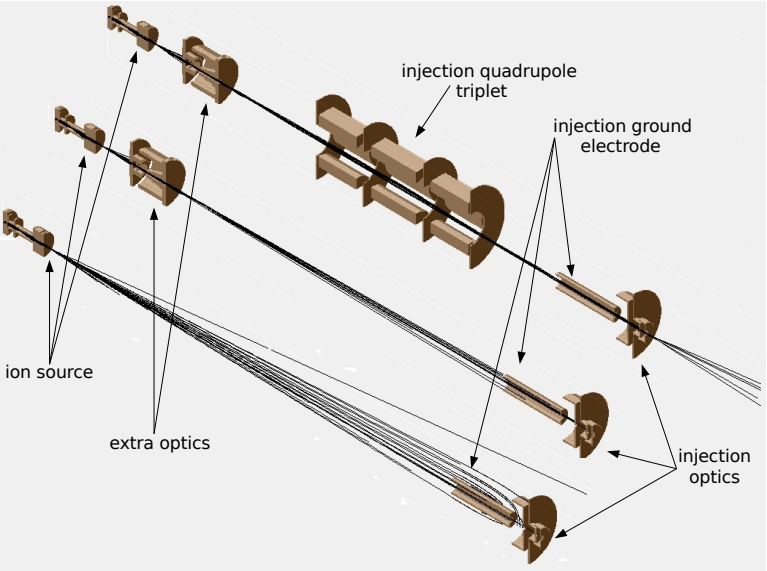

Figure 5.10: Beam calculations with and without the injection quadrupole triplet. The beams were travelling at 30 keV.

N471A ware used for the electrodes. For an ion beam extracted at 30 keV, the voltages necessary for the triplet were of about 2 kV. This was the recommended limit of what the Kapton wires used to connect the electrodes to the power supplies could sustain. Therefore, during the off-line tests it was only possible to optimize the quadrupole triplet voltages for beams up to 30 keV.

5.4 The main vacuum chamber assembly

Figure 5.12 shows the core of ISCOOL, which consist of injection optics, the trapping region and the extraction optics. A complete account of all the dimensions of the vacuum chamber as well as its mechanical characteristics can be found in [57].

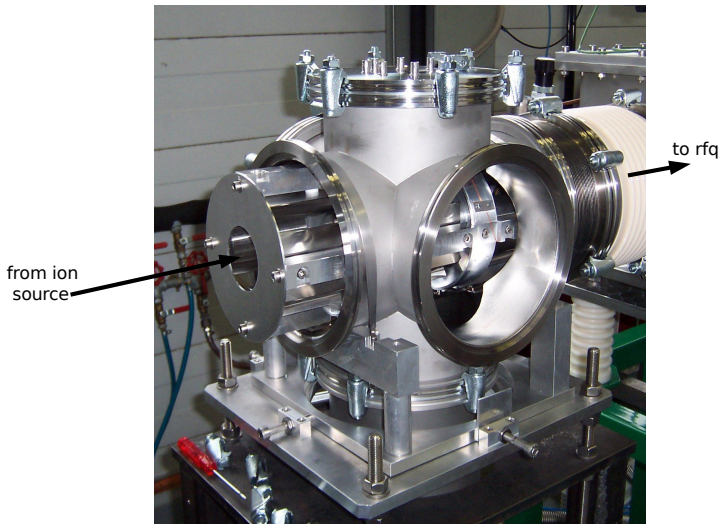

Figure 5.11: Installation of the injection quadrupole triplet at the off-line test bench. The top flange contains the connections feedthroughs for the triplet electrodes.

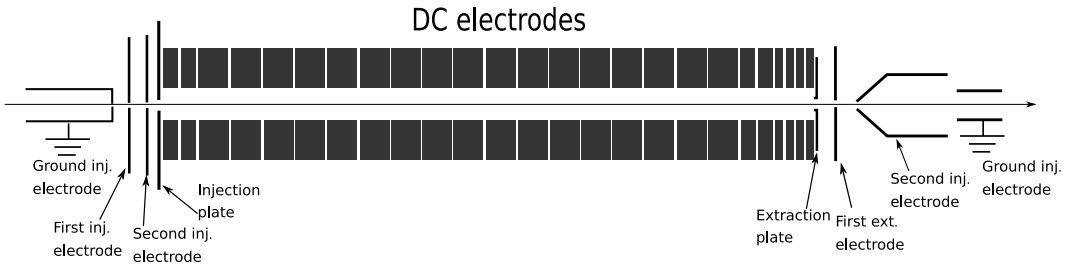

Figure 5.12: Main components of ISCOOL.

Injection optics

The injection optics comprises a ground injection electrode, two injection electrodes and an injection plate, as shown in Figure 5.12. These electrodes were designed [57] so as to gradually bring the difference of energy between the trap and the ion beam down to 100 eV. The two injection electrodes were powered with FUG HCN 7E-20000 NEG and FUG HCN 7E-12500 NEG power supplies, respectively. The injection plate was

Table 5.1: Set voltages for the injection optics relative to ISCOOL high-voltage V_p.

Injection electrode 1	Injection electrode 2	Injection plate
$V_p - 7000$ V	$V_p - 2000$ V	$V_p - 50$ V

powered with a DC24-D3500 power supply. Typical setting values used during the off-line tests are shown in Table 5.1.

Vacuum system

The beam line pressure at ISOLDE should ideally be kept at 10^{-7}mbar. This is a requirement which suits most of the experiments existing at the facility. Since there is a constant flow of a buffer gas inside the trap, a differential pumping scheme was needed.

Although it is true that the ion cooling is enhanced with higher pressures, an increase in the gas load may have three side effects. Firstly, it can exceed the pumping capacity of the vacuum pumps, making it more difficult to keep a satisfactory vacuum on the extremities of the device. Secondly, high pressures would spray the beam prior to re-acceleration, because in this region there is no RF field in order to keep the beam radially confined. Thirdly, the high voltage fields causes electrical sparks depending on the mean free path of the gaseous media. Therefore, in order to find the optimal gas pressure for the operation of ISCOOL, these constraints were tested in the off-line commissioning.

Figure 5.13 shows a layout of the vacuum system used in the test bench. On the extremities there were two Pfeiffer TPH 1201P turbomolecular pumps, with a pumping

capacity of 1200 l/s. They were connected to an Edwards RV12 rotary vane primary pump. In the middle section, there is another Pfeiffer turbomolecular pump, model TPH 1801P, with a pumping capacity of 1400 l/s. This pump was connected to an Edwards E2M28 two stage rotary primary pump. All the turbomolecular pumps were controlled by Pfeiffer DCU600 modules placed outside the HV area.

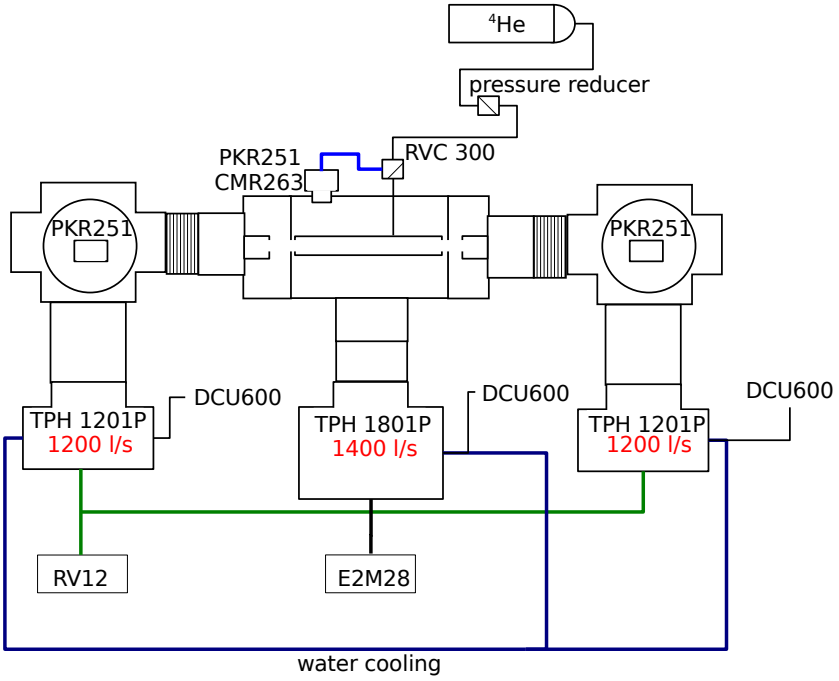

Figure 5.13: Layout of the vacuum system for the test bench.

The vacuum on the injection and extraction regions was monitored with two Pfeiffer PKR251 gauges. These gauge uses the cold cathode plus Pirani measurement devices in a single system. The Pirani system reads the pressure from 10^3 mbar to 10^{-3}mbar. From 10^{-3} mbar to 10^{-9} mbar the pressure is measured with the cold cathode. Therefore, pressures ranging from 10^{-9} mbar to 10^3 mbar could be measured. In

the beginning of the off-line tests, the pressure in the vacuum chamber was also measured with a PKR251 gauge. However, since the vacuum in this region lies between the two measurement systems employed, it was difficult to get it to work properly. Attempts to measure the pressure with a Pfeiffer CMR 263 capacitance gauge were made; however, this gauge operates with pressures ranging from 10^3 mbar to 10^{-3} mbar. Therefore it was not possible to precisely determine the pressure in this section during the off-line tests. Instead, the pressure on the extremities of the trap, hereafter defined as "side pressure" was the quantity measured. The buffer gas was helium. For a flow of between 0.1 mbar l/s and 1 mbar l/s, the pressure in the vacuum chamber was estimated to be ranging from 10^{-4} mbar to 10^{-3} mbar, which approximately scales down to 10^{-1} mbar inside the trap region, according to the calculations performed by Podadera [57]. For most of the tests a 200 mbar bottle of grade 6.0 (99.9999%) helium was used. From the bottle, there was a pressure reducer connected to the valve. The pressure reducer was always set to 0.5 mbar. From the valve, the gas was fed through a capillary metal tube to the region enclosed by the the DC electrodes. The valve was controlled by a Pfeiffer RVC300 unit. This device was also connected to the pressure gauge in the middle section.

DC electrodes

As briefly discussed in section 4.3, ISCOOL has 25 variable-width axial electrodes, which are wrapped around the quadrupole rods. This serves to create a potential gradient to guide the ions towards the trap extraction end. The application of modest

potential gradients (0.1 V/cm) allows 100 times faster extraction times [81]. This architecture also offers the possibility to swap the position of the electrodes for different axial trapping configurations. Each electrode is connected to a DC24-D3500 power supply. The last three electrodes can be fast-switched between two different power supplies. This alternative was not tested during the commissioning phase. Typical values for the DC electrodes used in the off-line tests are tabulated in 5.2. It is worth mentioning that according to calculations performed by Podadera [57], the voltage on each axial section of the trap approximately corresponded to a third of the voltage applied to the axial electrode.

Radiofrequency oscillator

The radiofrequency generator used for ISCOOL was designed and built by Klaus Rudolph [82]. It consists of one oscillator head, which generates the radiofrequency and a control unit. The oscillator head was placed inside the high voltage cage, on top of ISCOOL main vacuum chamber, whereas the control unit was located on the electronic rack, also inside the HV cage. The control unit could be controlled locally or remotely. This system was specified for a load of 300 pF, which is almost the measured capacitance of the rf rods (295 pF). The radiofrequency oscillator provides a sinusoidal voltage to the pair of RF-electrodes. These connections are symmetrical with respect to ground. There are two modes of operation. In *mode 1*, the frequency range lies between 200 kHz and 1000 kHz, with a voltage amplitude from peak-to-peak ranging from 100 V to 400 V. In *mode 2*, the frequency ranges between 300 kHz and 1400 kHz.

Table 5.2: Typical set voltages for the DC electrodes.

Electrode	Length (mm)	Voltage (V)
AX1	19	+110
AX2	19	+95
AX3	39	+90
AX4	39	+84
AX5	39	+82
AX6	39	+80
AX7	39	+76
AX8	39	+70
AX9	39	+65
AX10	39	+61
AX11	39	+57
AX12	39	+52
AX13	39	+48
AX14	39	+45
AX15	39	+40
AX16	39	+35
AX17	39	+30
AX18	39	+24
AX19	39	+20
AX20	19	+15
AX21	19	+13
AX22	9	+12
AX23	9	+10
AX24	9	+51
AX25	9	+110

In both modes, the frequency can be varied in steps of 1 kHz.

Figure 5.14 shows a scheme of the RF circuit. In the picture L1 and L2 indicate the inductances of the control winding and of the radiofrequency-output windings, re-

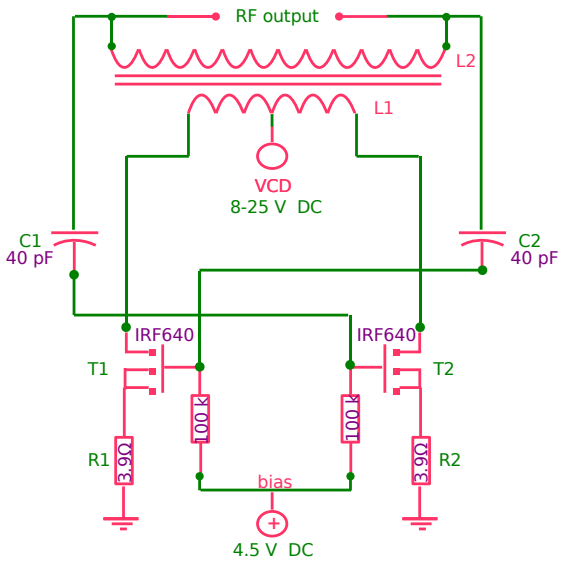

Figure 5.14: Diagram of the NG-VFO400/200-1200 sinus oscillator main circuit. Taken from [82].

spectively The rf inductance is a toroidal core wound up with copper wire. The core is made of ferrite, a ferromagnetic material. L2 and the total circuit capacitance form a resonant circuit. This arrangement has a fixed output frequency $\omega = \sqrt{\frac{1}{(L2)C}}$. Therefore in order to change the frequency it would be necessary to modify either the total capacitance or the inductance of the circuit. The solution proposed by Klaus was to change the frequency by changing the inductance. When the oscillator is switched on, it starts with the lowest possible frequency. To get higher frequencies the inductance is reduced by saturation of the core. The magnetic field H is related to the magnetic flux density by $B = \mu H$, where μ is the magnetic permeability. Due to a non-linear property in ferromagnetic materials, μ rapidly decreases as H gets stronger. The DC current applied on L1 serves to increase H so the ferrite becomes μ-saturated. As a consequence, the magnetic permeability does not increase with the magnetic flux in-

duced at the core. Instead, it drops, thus dropping the inductance L2, increasing the output frequency. The power comes from two IRF640 FET in a self-excited push-pull arrangement. A phase-locked-loop circuit was also integrated to the system to control the frequency of the oscillator and stabilize it. At the control unit there is a green LED to indicate when the frequency is locked. The amplitude is stabilized via the drain DC voltage at the FET. The voltage at the oscillator head is compared to the set value. In order to keep it at this value, the drain DC voltage of the FET is regulated accordingly. From the off-line tests, it was noticed that the oscillator could not deliver frequencies higher than 1 MHz with the required amplitudes in order to maintain the stability conditions of the ion motion inside the trap. This problem was later fixed by Klaus Rudolph in good time for the on-line commissioning.

Extraction optics

The extraction electrodes comprised an extraction plate, two extraction electrodes, and one ground extraction electrode as shown in Figure 5.12. This geometry was designed to gradually extract the ions back to the beam energy defined by the vacuum chamber ($<$ 60 keV) prior to extraction. The extraction plate was powered with two DC24-D3500 power supplies. The plate has two set values, namely “collection” and “extraction”, where the “collection” corresponds to the positive polarity power supply and the “extraction” corresponds to the negative polarity power supply. In the bunching mode these two power supplies are switched typically every 100 ms. The two extraction electrodes were powered with FUG HCN 7E-20000 NEG power supplies. Table 5.3

Table 5.3: Set voltages for the extraction optics relative to ISCOOL high-voltage V_p.

Extraction plate	Extraction electrode 1	Extraction electrode 2
$V_p - 0$V	$V_p - 500$V	$V_p - 6500$V

summarises the typical values used for the extraction optics during the off-line tests.

5.5 The complete set-up and external controls

Figure 5.15 shows the complete set-up in the test bench. Once this set-up was completed, access to the area enclosed by the Faraday cage was only necessary for the change in the ion source and minor intervention operations.

A control system was developed to set most of the parameters involved during the off-line commissioning. This system comprised hardware and a software for remote control. The control hardware was a Siemens S7-300 Programmable Logic Controller (PLC) placed outside the high voltage cage, acting as a master for an ET- 200M distributed station located at the high voltage platform. The user interface was written in LabVIEW, from National Instruments, by Talinen [83] and later modified for extra capabilities. The communication between the PLC and the stations was done with a Process Field Bus (Profibus) receiver/transmitter via a fibre optics cable. This interface allowed the user to control the power supplies for the injection electrodes and the extraction optics, as well as for the DC segments. The DC electrodes had $0-10$V analog input and output signals, with an accuracy of 0.1% of the controlled range. In addition, the interface permitted the control of the radiofrequency and gas flow. Figure

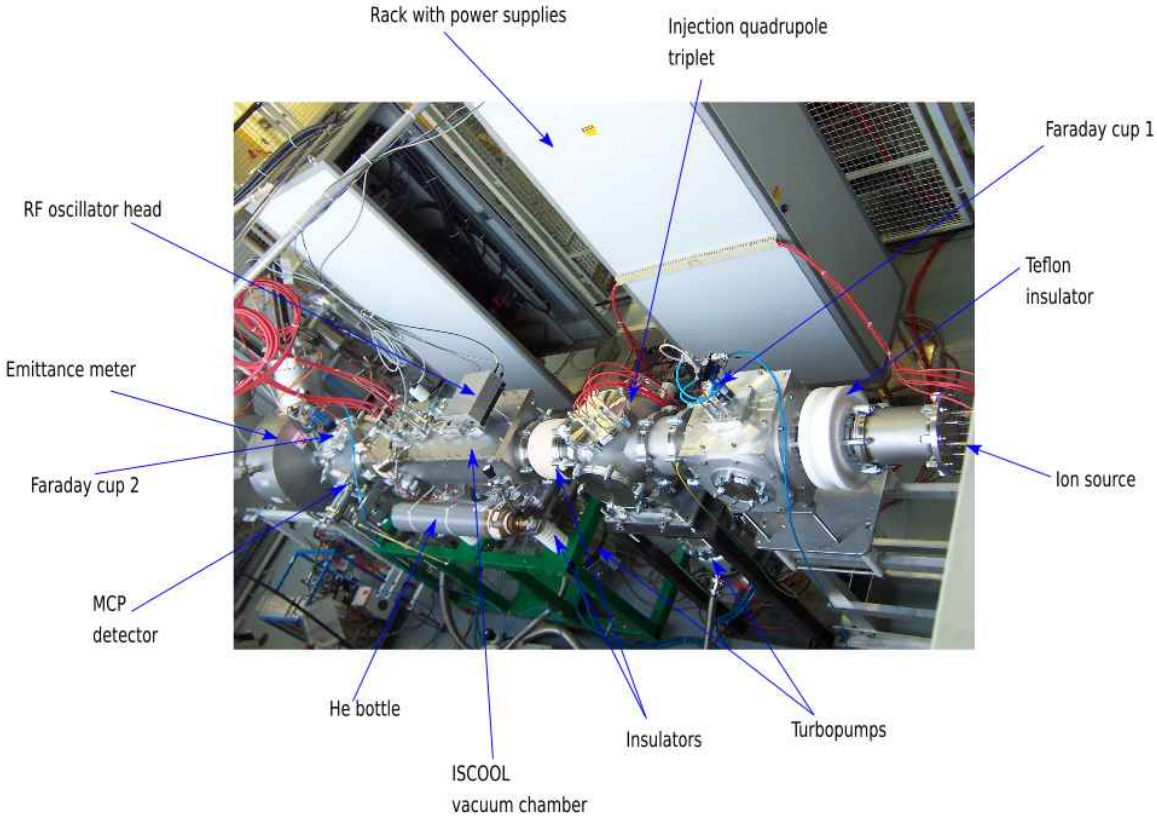

Figure 5.15: The complete set-up. The beam travelling direction is from the right to the left.

5.16 shows a scheme of the I/O hardware for the control system. During the off-line tests the injection quadrupole triplet and ion source control voltages were tuned manually with a Teflon stick. Both emittance meters from Orsay and ISOLDE had their own control system.

In the graphical interface, shown by Figure 5.17, the grey fields were for monitoring purposes, whereas the white fields allowed the user to make changes within the range indicated in square brackets. An excellent matching with monitoring values has been observed. Also, for a given ion mass and a set of voltage amplitude and frequency

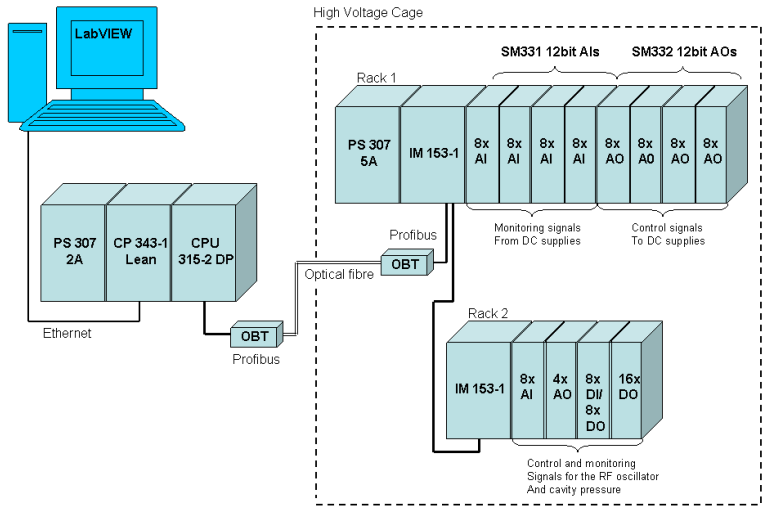

Figure 5.16: Scheme of the off-line *I/O* hardware used for the control system. It comprised analog input (*AI*) and output (*AO*) modules to control the DC supplies and digital inputs (*DI*) and outputs (*DO*) used to control the RF and pressure. Taken from [83].

the interface (see Figure 5.17) calculated the Mathieu q value, which was essential in order to understand the stability conditions of the ions inside the device. The author of this thesis implemented the buffer gas feeding control with two modes of operation. In the pressure mode, the user could set a pre-defined nominal pressure and the RVC300 controller would adjust the valve in order to reach this pressure. In the flow mode, the user could control a voltage lying between $(0-10)$ V and the valve, which is factory calibrated for the voltage against flow would open or close accordingly. Since the pressure readout from the gauge installed in the vacuum chamber was not reliable for reasons already discussed, the flow mode ended as the final method of operation for the buffer gas.

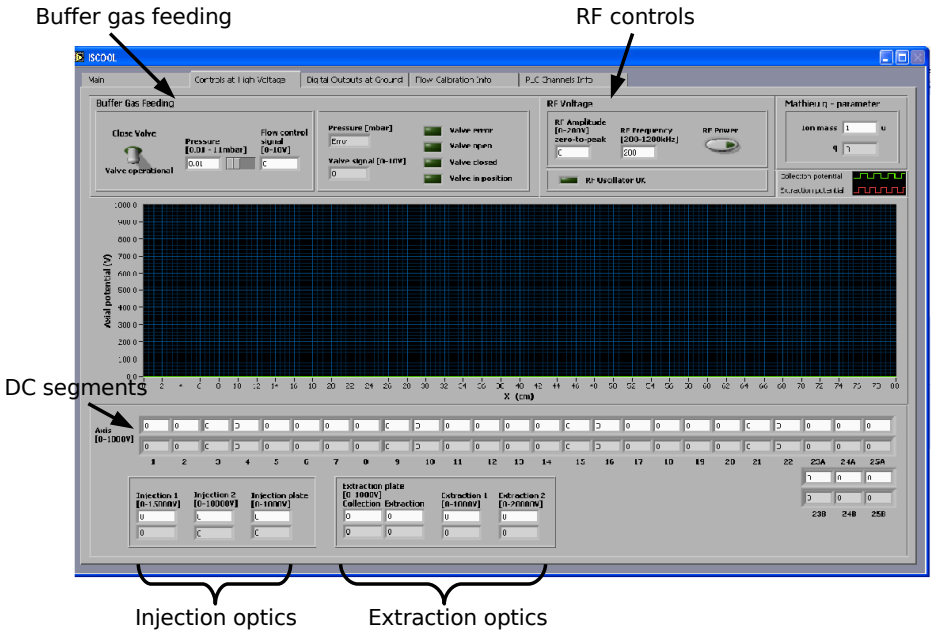

Figure 5.17: Graphical user interface used to control most of the ISCOOL parameters.

5.6 Results in continuous mode

The trap parameters such as the radiofrequency and amplitude, the gas pressure, the injection optics, the extraction optics and the potential gradient produced by the DC electrodes were optimized for maximum transmission. The following subsections outline the main results of the off-line commissioning, including the transmission efficiency and transverse emittance.

5.6.1 Cesium

The first element used in order to characterize the cooler in the off-line test bench was $^{133}Cs^{+}$. This element was also the heaviest available for the tests. Thus, it was useful

Table 5.4: Set voltages used for the injection quadrupole triplet. The notation "U" and "D" stand for "up" and "down". The numbers indicate the sections of the triplet. The beam is injected through section 1.

UD1	LR1	L2	R2	U2	D2	UD3	LR3
+1950V	−1930V	+2216V	+2318V	−2000V	−2343V	+1168V	−1233V

to check the upper limit of the efficiency. The pressure on the extremities of the trap was approximately 10^{-6} mbar. The bias voltage of the ion source was set to +300 V and the extraction voltage +295 V. The first lens voltage was +292 V. The second set of Einzel lenses at the ion source had no effect on the beam focusing and were set to zero. The third lens was set to +350 V. Table 5.4 summarises the set voltages of the injection quadrupole triplet. The difference between the voltages applied to the second section of the injection quadrupole triplet can be in part explained by a misalignment of the beam line.

Concerning the injection optics, the first injection electrode was set to +6350 V, the second injection electrode was set to +1600 V and the injection plate to +60V. For the extraction electrodes, the extraction plate set to 18 V. Extraction electrodes 1 and 2 were set to +1000 V and +12600 V, respectively. This set of values maximised the injection of ions in the trap. For the purpose of efficiency measurements, Figure 5.18 shows the transmission efficiency of 4.7 nA $^{133}Cs^{+}$ at 30 kV as a function of the voltage applied at the extraction plate. Since there is a sudden drop in the transmission efficiency for a small voltage difference, the energy spread before re-acceleration and extraction could be estimated to be ≈ 1 eV.

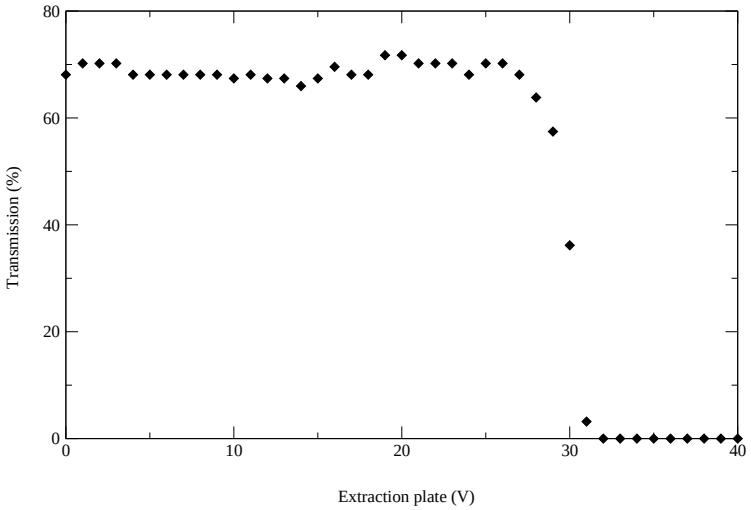

Figure 5.18: Transmission efficiencies for $^{133}Cs^{+}$ as a function of the voltage applied at the extraction plate.

Figure 5.19 shows the emittance diagrams of $^{133}Cs^{+}$ ions extracted at 30.3 keV. The measurements were made with the emittance meter from Orsay.

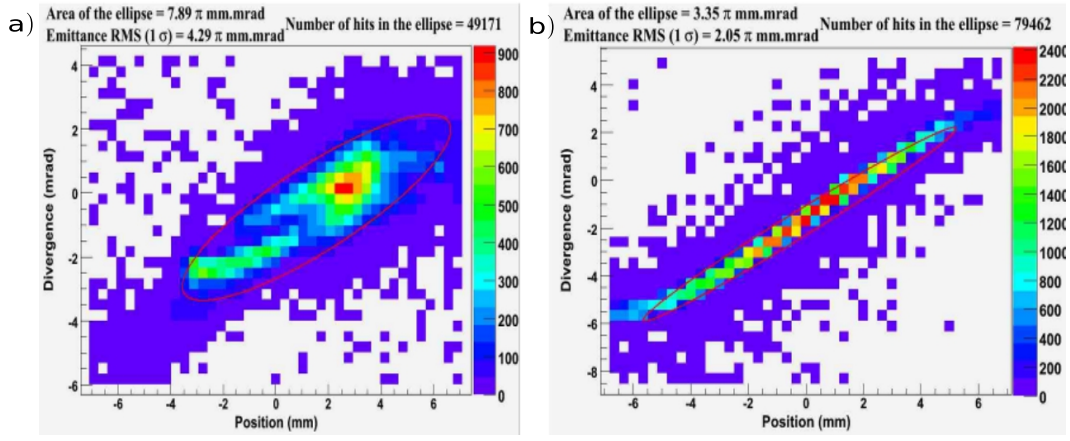

Figure 5.19: In a) the emittance of $^{133}Cs^{+}$ transmitted without gas, whereas b) shows the reduced emittance once the gas is injected in the trap.

In Figure 5.19.(a), 10 pA of cesium was injected in the trap without the buffer gas. The transmission efficiency was 10%. In Figure 5.19.(b), it is shown the emittance measured with the same parameters, except for the fact that helium has been released in the chamber with a flow of 0.1 mbar l/s. The presence of the buffer gas resulted in a transmission efficiency of 70% of cesium. Figure 5.19 also shows a significant difference in the emittance diagrams. Once the cesium undergoes thermal collisions with the buffer gas, there is almost a 3-fold reduction in the transverse emittance. Figure 5.20 shows the dependence of the transmission efficiency as a function of the radiofrequency.

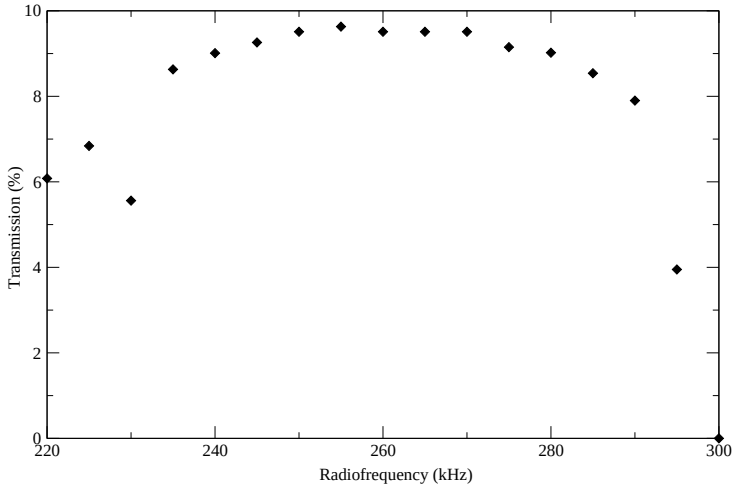

Figure 5.20: Transmission of uncooled ions against radiofrequency for $^{133}Cs^{+}$. The ions are extracted at 2 kV. The uncertainty in the measurement is $\sim 5\%$. This estimate is used hereafter.

The amplitude was fixed at 240 V_{0-p} (zero-to-peak). The incoming current was

0.79 nA. During these measurements, the settings for the ion source power supply were +4.5 V, 1.58 A. The HV was 2 kV, with a bias of 200 V. The extraction voltage was set to 190 V. Lens 1 and 2 were set to 2 kV and 0.63 kV, respectively. The triplets had not been installed during this measurement. Therefore the maximum transmission efficiency was limited to 10%. The measurement was useful to show that the trap can work as a "high-pass" mass filter, since a large frequency bandwidth $240 - 280$ MHz, the transmission was hardly altered. This result can be understood in connection with the Mathieu q parameter. It was also instructive to understand the behaviour of the transmission efficiency as a function of the buffer gas pressure in the trapping region. For monitoring purposes, the pressure was measured with a gauge located in one of the trap extremities. The result of this analysis is shown in Figure 5.21.

What is interesting in this data is the collisional focusing effect already alluded to in section 4.3.2. The plot also indicates a subsequent saturation in the transmission curve, followed by a sudden drop. This drop is believed to be related to a leak of the buffer gas out of the main vacuum chamber. In fact, on this occasion the current measured with the first Faraday dropped from 3 nA to 0.16 nA.

5.6.2 Potassium

A number of different systematic measurements was carried out for $^{39}K^{+}$. During these tests, the current measured in the first Faraday cup was 11.5 nA, with the ion source power supply at 5 V, limited to 1.8 A of current. The influence of the buffer gas pressure on the transmission and emittance was investigated. The radiofrequency and

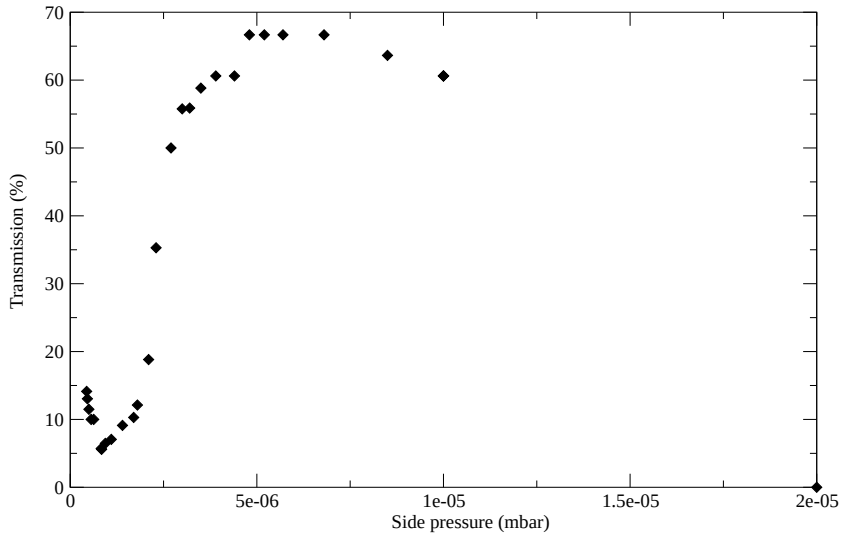

Figure 5.21: Transmission of $^{133}Cs^{+}$ against gas pressure measured outside the main vacuum chamber.

amplitude were fixed to 520 kHz and 280 V_{0-p}. In terms of the Mathieu parameters, this gave $q = 0.65$. Figure 5.22 presents the results. The transmission efficiency monotonically increased with more gas injected in the chamber. It then reached a saturation point at a side pressure of flow of 5×10^{-6} mbar. For the emittance, the plot indicates that with no gas inside the trap, the emittance was 32π mm.mrad. As the buffer gas flow increased, the emittance experienced a 10-fold decrease, while the transmission reached its maximum value. Once again, a remarkable feature of this plot is the deep saturation of the efficiency and emittance at about the same gas pressure, which indicates a strong correlation between the enhancement in the transport of the ion beam and the underlying cooling process.

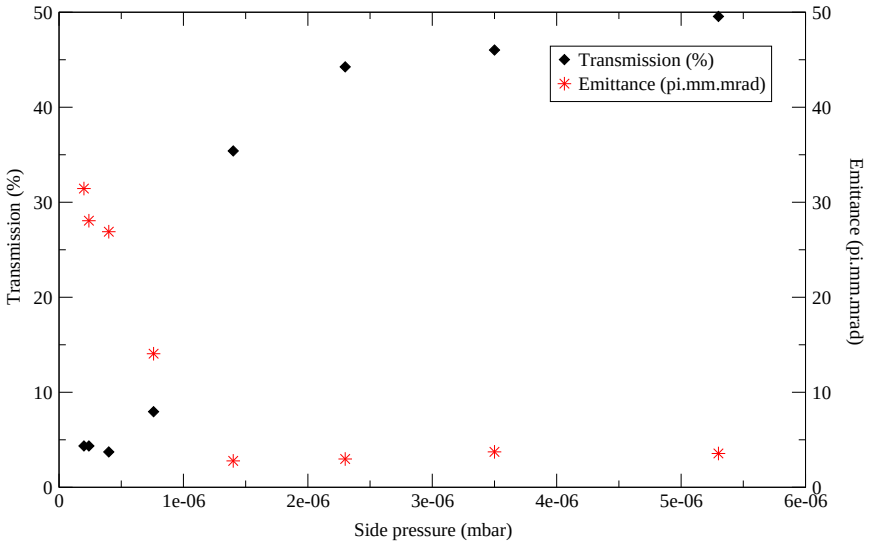

Figure 5.22: Transmission efficiencies and transverse emittance for $^{39}K^{+}$ as a function of the gas pressure measured on the sides of the cooler.

Figure 5.23 shows the results from the analysis of the influence the radiofrequency amplitude had on the transmission and emittance. From the data, it is apparent that although there is almost a reduction factor of 2 in the emittance, the overall trend varies only slowly, whereas the transmission dramatically increases with the rf amplitude. Finally, a complementary study was carried out to assess how the radiofrequency influenced the transmission efficiency and the emittance. Figure 5.24 shows the results. The transmission efficiency rapidly peaks at 500 kHz, then steadily decreases with increasing radiofrequencies. However, the data suggest that around the peak frequency, the cooler should still transmit as a “high-pass” mass filter. It can be seen from the plot a lack of emittance data points before 420 kHz. This was due to limitations of

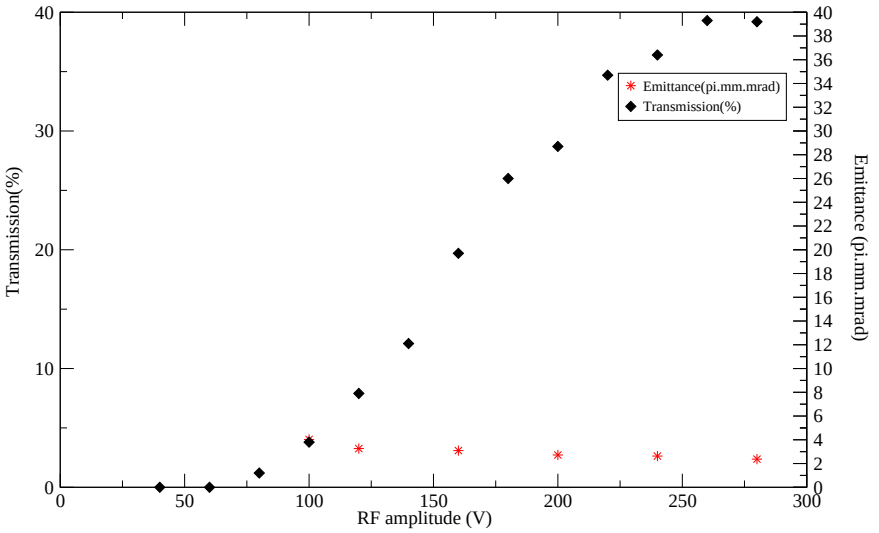

Figure 5.23: Transmission efficiencies and transverse emittance for $^{39}K^{+}$ as a function of the rf amplitude. The frequency was fixed to 520 kHz.

the ISOLDE emittance meter, which requires a minimum of 1nA of current in order to operate.

5.6.3 Sodium

In order to test the transmission in continuous mode of $^{23}Na^{+}$, the radiofrequency was fixed at 650 kHz and the amplitude 280 V_{0-p}. During these measurements, it was found that the current from the ion source was rather unstable. Figure 5.25 shows the results. From the plot, it can be seen that it follows the same systematics of potassium. Finally, an interesting result that emerges from this data is the fact that initially the transmission suffers a small decrease with the increase of the buffer gas. A possible

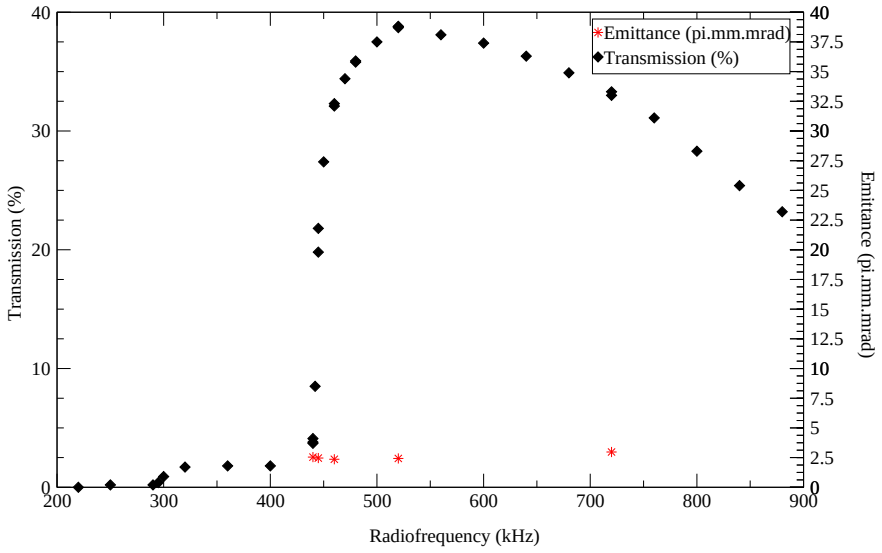

Figure 5.24: Transmission efficiencies and transverse emittance for $^{39}K^{+}$ as a function of the rf amplitude. The amplitude is fixed to $280V_{0-p}$.

explanation for this result might be due to a non-linear behaviour between the voltage and gas flow calibration of the RVC300 valve controller in the region studied.

Further to the previous buffer gas systematics for $^{23}Na^{+}$ ions, another set of measurements was taken in order to assess the dependence of the transmission on the radiofrequency amplitude. This study was made for both cases of transmission with cooling and without cooling. The same dependence was investigated for the emittance, but only considering cooled ions. The rf was fixed at 650 kHz. The buffer gas flow was kept at 0.1 mbar l/s (side pressure 4.6×10^{-6} mbar). The incoming current was 6.4 nA for the scans without buffer gas, about $12-6$ nA for the tests with cooling and 4.4 nA for the emittance scans. Figure 5.26 summarizes the results.

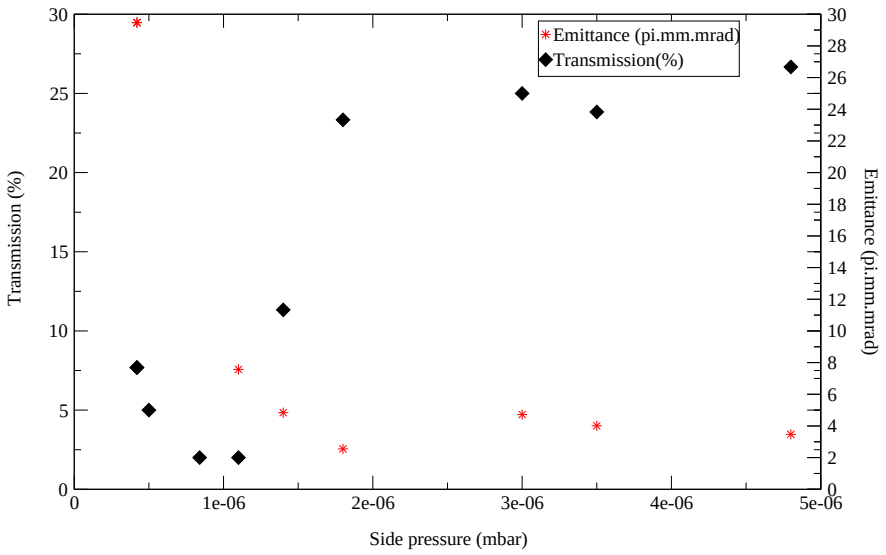

Figure 5.25: Transmission efficiencies and transverse emittance for $^{23}Na^{+}$ as a function of the gas pressure measured on the sides of the trap.

This plot is revealing in several ways. First, unlike the clear saturation in the case of transmission with cooling, the data represented by the squares connected by the dotted lines show that there is a staggering effect in the transmission as a function of the zero-to-peak field amplitude. Second, in the region between 200 V and 250 V the emittance follows the same trend as the transmission without cooling. This means that the ion motion is dominated by instabilities which are not being damped by the buffer gas.

A complementary measurement was taken, this time keeping the amplitude fixed ($280V_{0-p}$), but varying the radiofrequency. The flow was still kept at 0.1 mbar l/s. For the emittance measurements, the current measured at the first Faraday cup was

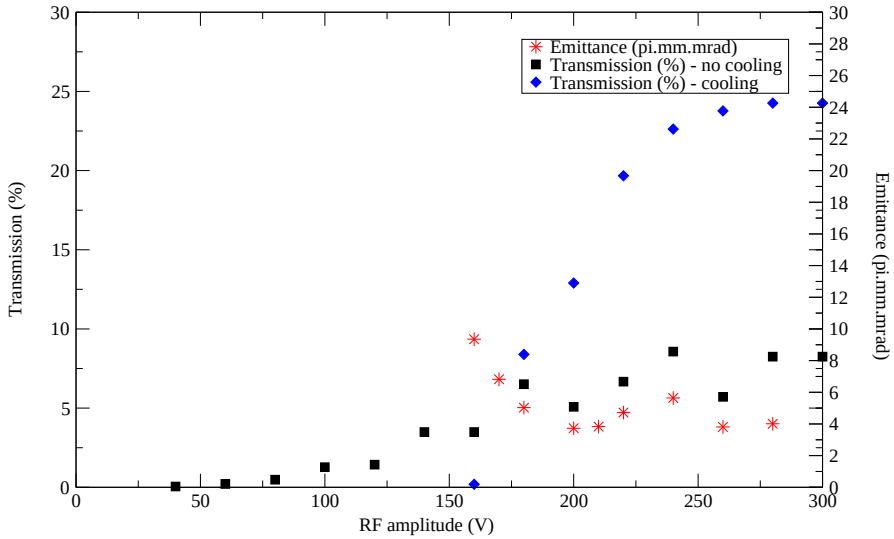

Figure 5.26: Transmission efficiencies and transverse emittance for $^{23}Na^{+}$ as a function of the rf amplitude. For the emittance data, cooling is assumed.

between $5-9$ nA. The results obtained by these measurements are shown in Figure 5.27.

Interestingly, this plot suggests a stepwise behaviour in the transmission efficiency with increasing radiofrequency. It was first believed that this was due to other elements being extracted from the ion source. However, an analysis of the composition of this ion source using the Scanning Electron Microscope/Energy Dispersive X-Ray Spectroscopy (SEM/EDX) technique [84] indicated that indeed the ion source beam was predominantly made of sodium. It is possible that this behaviour could be understood in terms of the different regions of stability for the ion motion, which would affect the transmission efficiency. On the other hand, this effect is washed out when no cooling

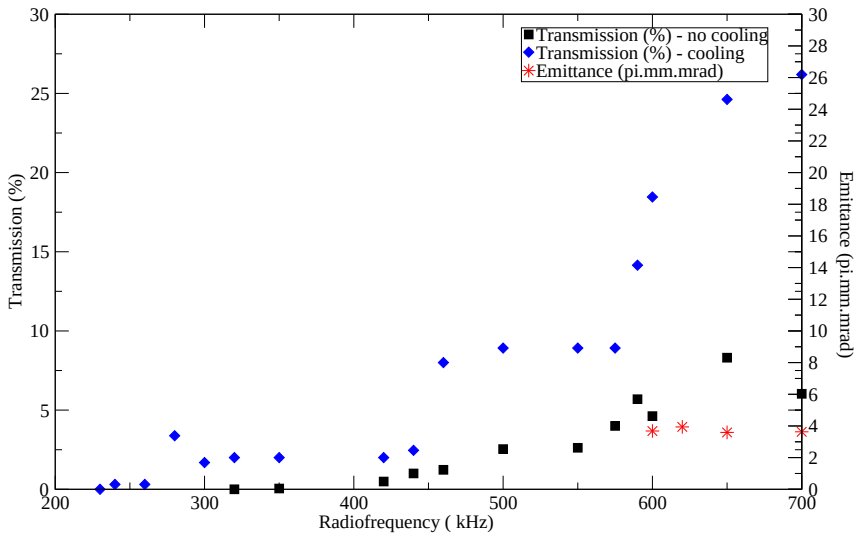

Figure 5.27: Transmission efficiencies and transverse emittance for $^{23}Na^{+}$ as a function of the rf. For the emittance data, cooling is assumed.

is involved. It can also be seen from this plot that the emittance remains to some extent insensitive to changes in the radiofrequency. By comparing the evolution of the transmission efficiency at the same rf region, it is clear that the rf helps to compress the ion cloud as the cooling effect takes place.

As a final remark, since the errors were not included in these measurements due to instabilities in the ion source, caution must be applied for the interpretation of these observations. As a conservative estimate, the error on the transmission efficiency was of the order of $3\% - 5\%$. Therefore some of the claimed effects are only speculative.

5.6.4 Lithium

This element was useful to check the lower limit of the transmission efficiency against mass. Figure 5.28 shows the systematics in the transmission of 0.25 nA of $^{6}Li^{+}$ injected into the trap, as a function of the radiofrequency. The amplitude was fixed at 280 V_{0-p}. From this plot, it can be seen that the transmission efficiency as a function of the radiofrequency displays a similar behaviour to that of ^{23}Na ions. At 500 kHz the curve reaches a saturation point.

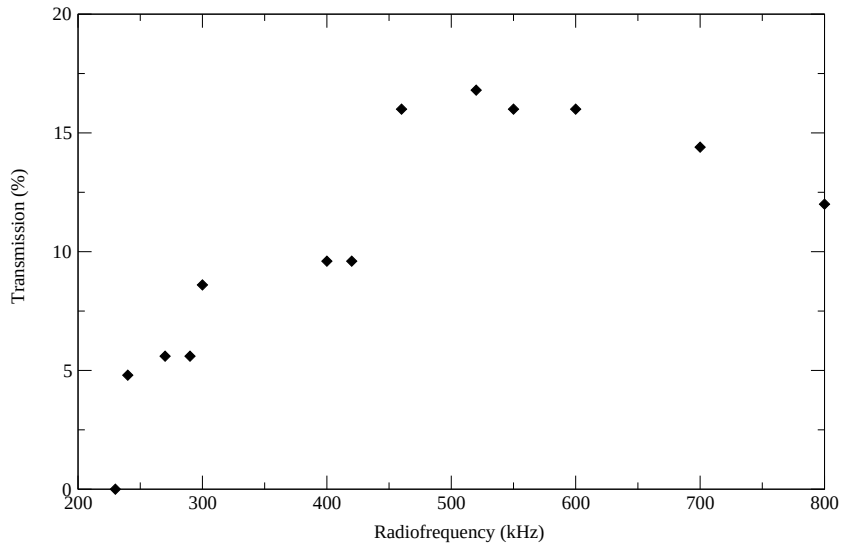

Figure 5.28: Transmission efficiencies and transverse emittance for $^{6}Li^{+}$ as a function of the radiofrequency.

The optimum transmission in continuous mode for this element was 18%. It is worth mentioning that this relatively low transmission is due to the fact that helium was used as the buffer gas; therefore, ions with light masses such as lithium will suffer

Table 5.5: Transmission efficiencies and emittances for the elements used in the off-line tests.

Element	Transmission efficiency	Transverse emittance at 30 keV
^{6}Li	17%	-
^{23}Na	28%	3.47π mm mrad
^{39}K	68%	3.56π mm mrad
^{133}Cs	79%	3.35π mm mrad

from the effect of rf heating and will not be efficiently transmitted.

5.6.5 Argon

$^{40}Ar^{+}$ was used for the tests with a MK5 ISOLDE plasma ion source unit. It has been observed that the current measured in the first Fadaray cup was 10 times higher when a normal load of buffer gas was released into the trap. It is likely that residual buffer leaking from the trap has drifted and has been ionized in the plasma. Therefore, it was not possible to make any efficiency estimates with this type of ion source. On the other hand, in a real on-line scenario, this will not pose a problem, since it is unlikely that helium would drift towards the target-ion source region.

5.7 Summary

Table 5.5 summarises the main results as far as the transmission in continuous mode is concerned at 30 keV, and Table 5.6 summarises the best parameters found for operation of ISCOOL during these tests. It is apparent from Table 5.5 that the reduction of the emittance is a property which is independent of the incoming beam. It is also

important to recall that the beam emittance is expected to be lower with the increase of the HV, which at ISOLDE is typically 60 kV. These results matched the assigned requirements, and had been presented to the ISCC (ISOLDE Scientific Coordination meeting) on a continuous basis. In December 2006 Richard Catheral took over the role of Technical Coordinator of ISOLDE and became responsible for the ISCOOL integration. Further studies were requested on transmission in bunched mode and on "ISOLDE like" beams. Meanwhile, integration issues started to be dealt with by the technical team. Permission was granted to install ISCOOL in situ at the ISOLDE hall during the Summer 2007.

Table 5.6: Optimal settings of ISCOOL for different masses.

Control	^{6}Li	^{23}Na	^{39}K	^{133}Cs
Inj. 1	−7000 V	−7000 V	−7000 V	−6050 V
Inj. 2	−2000 V	−2000 V	−2000 V	−2100 V
Inj. Plate	−50 V	−50 V	−50 V	−50 V
AX1	+150 V	+100 V	+100 V	+110 V
AX2	+101 V	+80 V	+80 V	+95 V
AX3	+59 V	+70 V	+70 V	+90 V
AX4	+58 V	+67 V	+67 V	+84 V
AX5	+56 V	+65 V	+65 V	+82 V
AX6	+54 V	+64 V	+64 V	+80 V
AX7	+52 V	+62 V	+62 V	+76 V
AX8	+50 V	+59 V	+59 V	+70 V
AX9	+48 V	+56 V	+56 V	+65 V
AX10	+46 V	+53 V	+53 V	+61 V
AX11	+44 V	+50 V	+50 V	+57 V
AX12	+42 V	+47 V	+47 V	+52 V
AX13	+40 V	+44 V	+44 V	+48 V
AX14	+38 V	+41 V	+41 V	+45 V
AX15	+36 V	+38 V	+38 V	+40 V
AX16	+34 V	+35 V	+35 V	+35 V
AX17	+32 V	+32 V	+32 V	+30 V
AX18	+30 V	+29 V	+29 V	+24 V
AX19	+28 V	+26 V	+26 V	+20 V
AX20	+26 V	+23 V	+23 V	+15 V
AX21	+25 V	+20 V	+20 V	+13 V
AX22	+24 V	+17 V	+17 V	+12 V
AX23	+23 V	+24 V	+14 V	+10 V
AX24	+30 V	+60 V	+30 V	+51 V
AX25	+70 V	+130 V	+100 V	+110 V
Ext. Plate	−1 V	−5 V	−3 V	0 V
Ext. 1	−500 V	−800 V	−900 V	−500 V
Ext. 2	−8000 V	−8000 V	−8000 V	−6500 V
RF	900 kHz	650 kHz	520 kHz	300 kHz
Amplitude	280 V	280 V	280 V	300 V

CHAPTER 6

THE ISCOOL ON-LINE COMMISSIONING

The insertion of ISCOOL at the focal plane of the HRS during the summer 2007 was made possible due to the positive results obtained from the off-line commissioning phase. Figure 6.1 shows the final location of the device. The installation work comprised the integration of the vacuum system to the existing network, the connection of the pumps to the central exhaust containers, the construction of water cooling circuits for the turbomolecular pumps, the mechanical alignment of the new beam line element, the installation of the extraction quadrupole triplet, as well as the construction of one high voltage cage for the trap and one for the electronics and power supplies. All the controls for the power supplies of the DC electrodes, which include the injection, the 25 segments and extraction optics became part of the standard ISOLDE control system. The control of the gas pressure and the radiofrequency were maintained in LabVIEW. Following the installation work, done by the ISOLDE technical team, the on-line commissioning took place in November 2007. This was also a convenient opportunity to start optimising the device for future on-line runs. During these tests, it

was also possible to further characterize the device in conjunction with the COLLAPS laser spectroscopy setup.

Figure 6.1: The location of ISCOOL before and after the on-line commissioning.

This chapter is dedicated to the first tests of bunched beam laser spectroscopy with ISCOOL. These results of these investigations were reported in [85].

6.1 Laser spectroscopy of ^{39,44,46}K and ^{85}Rb

The COLLAPS line (see Figure 4.4) was not modified for these tests, apart from a Faraday cup, which was placed at the end of the line, for monitoring the ion beam current. Tests were made on stable ^{39}K and on radioactive ^{44,46}K, produced from a Ta target. Tentative bunched beam collinear laser spectroscopy was performed on ^{48}K. In addition, stable ^{85}Rb was studied. These elements were surface-ionised and extracted at 30 keV. The nominal value for the high voltage of ISCOOL was 29.920 kV. The transitions chosen were the D_2 lines both for sodium and rubidium. Since these are atomic transitions, the ions were neutralised by passage through the charge exchange cell, which was filled with hot potassium vapour. The fluorescence photons were detected by two Burle 8852 photomultiplier tubes. It should be noted that during a substantial part of the tests, the tubes were operated without any cooling, so that a high rate ($\sim$ 42 kHz) of dark counts was recorded. Furthermore, the D_2 transitions for potassium and rubidium (766 nm and 780 nm, respectively) were not situated in the peak of the tube's spectral responsitivity curve. Finally, tubes designed for the infrared region have intrinsic low quantum efficiencies (5% at best, for the Burle tubes). The Coherent 899-21 Ti:Sa solid state ring laser was used (see Figure 3.5). It was pumped by an argon ion laser, model Coherent INNOVA 400 series. The wavemeter used was a Burleigh, model WA-20. This wavemeter was a Michelson interferometer equipped with an internal He-Ne laser. The laser frequency could be determined with an accuracy of 3 MHz.

6.1.1 Laser and ion beam overlap

The beam extracted from ISCOOL was steered to the COLLAPS line with minor adjustments on the voltages applied to the beam line elements. In order to maximise the detection efficiency, the ion and laser beams were tuned to produce an overlap at the light collection region. Two apertures were inserted in the COLLAPS beam line for this purpose. The first aperture had 1 mm diameter and was placed before the light collection region. The second aperture with 4 mm diameter was placed after the light collection region. In addition, a Faraday cup was installed at the end of the beam line. The last element of the setup was a Brewster window, which served to transmit the laser through without internal reflection and to help with the laser alignment. With the first aperture in place, 45% of 2 nA of ^{39}K extracted at 30 keV was measured with the last Faraday cup. With both apertures in, 27% was transmitted. It should be noted that an ion beam with a large emittance makes inevitable the employment of hard ion beam focus or more laser power (to increase the beam waist), or more generally, a combination of both. A harder focus introduces skewed ion velocities. This has a detrimental effect for the quality of the spectral data, since it will produce resonances which no longer possess a symmetrical profile, as studied by Campbell [46]. More laser power proportionally increases the laser scatter, which increases the background. Under these circumstances, the reduction of the ion beam transverse emittance provided by ISCOOL allowed the use of less laser power, because of the reduced laser beam waist now required for good atom-laser overlap. Therefore, the laser scatter at the interaction region, which is normally a dominant source of background became less

of an issue. As a concrete example, on the COLLAPS beam line typical background due to dark counts is 300 s^{-1}, whereas the background due to laser scatter is 3000 s^{-1} per mW of laser power [86]. During the online commissioning of ISCOOL, the latter source of background was reduced to $\sim$ 1500 s^{-1} per mW of laser power.

6.1.2 Timing of signals and data acquisition

For the measurements in continuous mode the scans were made in the usual way, as detailed by section 4.2. For measurements undertaken in bunched beam mode, the data acquisition was changed to account for the new time structure of the ion beam. In this mode, the timing was controlled by a function generator, model Philips 5768, which was used to generate a TTL signal to a fast-switch which was connected to the end plate electrode. The switch used was a Belhke High Voltage Push-Pull Switch, model GHTS 60. Two power supplies were connected to the switch inputs. One power supply was set to 50 V and the other to 0 V. By varying the period time in the function generator, it was possible to control the accumulation and release time of the bunches. The trap was set to accumulate for typically 100 ms and open for 100 μs. Since the fast switch was placed in the high voltage cage, it was necessary to send the TTL signal from the function generator via an optical fibre link, as schematically illustrated by Figure 6.2.

The same TTL signal which was sent to open the trap, was used to generate a gate signal with a width set to be equal to the time spread of the ion bunch. This signal was produced by a dual timer Ortec N93B. With this device, it was also possible to

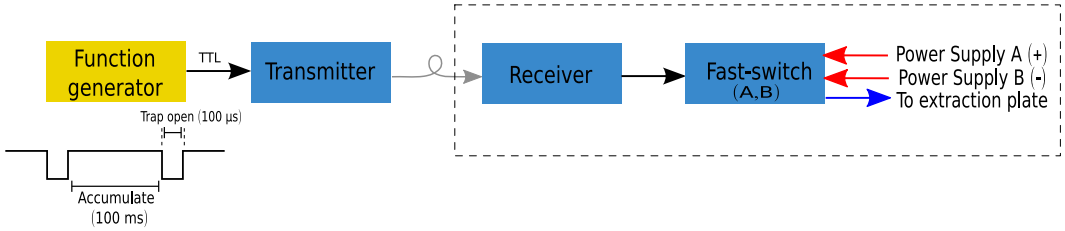

Figure 6.2: Scheme on how the signals are produced and send to ISCOOL and COLLAPS.

introduce a delay in the signal in order to account for the time of flight of the ion bunch from the cooler to the interaction region. This distance was of ~ 20 m, which for the K and Rb beams at 30 keV corresponded to a time delay of $50 - 100$ μs. A CAEN NIM-N405 3-fold logic unit was used to gate the photon events so they were registered only during the time window defined by the bunch width, thereby vetoing any background event which happened outside this time window. The modifications made in the electronics involved in the data acquisition are shown by Figure 6.3.

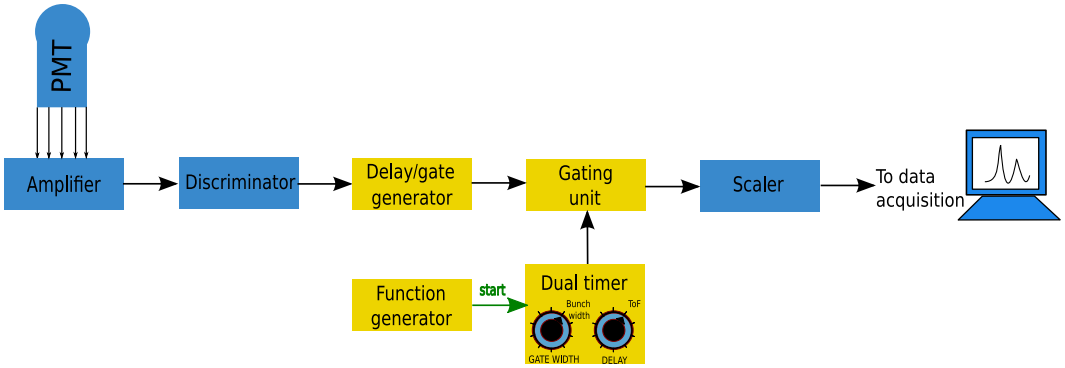

Figure 6.3: Modified electronics for the bunched beam mode of acquisition.

Although this scheme was suitable for a first demonstration of bunched beam spectroscopy, the COLLAPS data acquisition was free running in "passive" mode. Therefore, the dwell time had to be "manually" synchronised with the period imposed by the

function generator. The system was later changed so that during a scan, the data acquisition software originated a signal, which was sent to the cooler in order to release the ions. In this way, each channel in the spectrum recorded the same number of ion bunches.

Finally, since the beam energy was redefined by ISCOOL high voltage, the total voltage for a channel i was given by

$$V(\text{ch}\#i) = V_{\text{ISCOOL}} - V_{\text{Fluke}} - k \times V_i^{\text{MCP}}, \tag{6.1}$$

where $V_i^{\text{MCP}} = \frac{\Delta V}{N} \times i$ and k is the Kepco amplification factor, as explained in section 4.2. With this modification, the spectra could be converted to frequency using the relativistic Doppler shift equation (Equation 3.14).

6.2 Bunch width

During the on-line commissioning, it was possible to make the first characterisation of the ion bunch released by ISCOOL. The bunches were initially measured with the MCP detector placed at the exit of the trap. However, the downside of this type of detector is that it cannot distinguish between the ions of interest and isobaric contaminants or even molecular ions of similar mass. This ambiguity was eliminated by counting the time distribution of photons resulting from laser-induced fluorescence. For this purpose, a Stanford Research Systems SR430 Multichannel Scaler (MCS) was used to count the photons as a function of time. In this way the time-of-flight (ToF) of the ion bunch was measured. The device was triggered by the same TTL pulse which was used to open

the end plate of ISCOOL in order to release the bunch. In addition, the tuning voltage was held constant on a resonance peak. The effects of several ISCOOL parameters were investigated.

6.2.1 Accumulation times

The number of ions injected into the trap could be controlled with a movable slit placed after the HRS. Figure 6.4 summarises the measurements carried out for ^{85}Rb ions against different accumulation times, ranging from 2.5 ms to 100 ms.

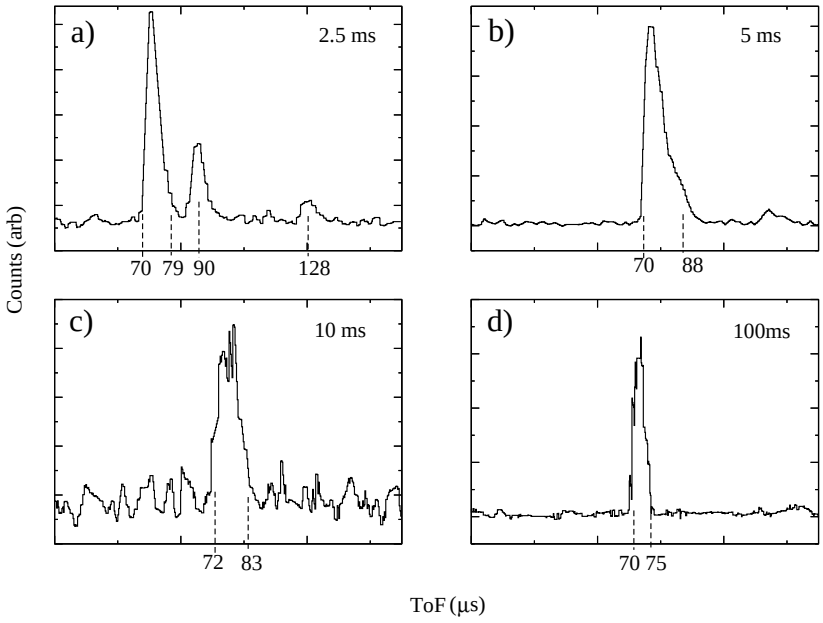

Figure 6.4: Bunch widths of ^{85}Rb. The time markers in the *x* axes were measured in μs. The accumulation times in the trap are shown in the top right hand corner. In a) and b) the number of bunched ions are 3×10^4 and 6×10^4, respectively. In c) 5×10^3 ions were bunched, whereas in d) 5×10^4 were bunched. The *y* axes are not on the same scale. Adapted from MCS display.

Figures 6.4.(a) and 6.4.(b) show the bunch widths of ions injected at ISCOOL with the same rate, but with accumulation times of 2.5 ms and 5 ms, respectively. It should be noted that a two-fold increase in the the number of accumulated ions caused the first two bunches to merge. The origin of this effect is not understood. In Figures 6.4.(c) and 6.4.(d), a similar study was performed, but with less ions injected into the trap than in 6.4.(a) and 6.4.(b). This time the investigation showed that a ten fold increase in the accumulation times helped to reduce the bunch width. Taken together, these results suggest that a compromise between the number of ions injected and accumulation times must be met in order to achieve shorter ion bunches.

Of special importance was an investigation on how space-charge effects would affect the bunch width. Figure 6.5 shows the bunch width characterization of ^{85}Rb. In this study the accumulation time was fixed at 100 ms. In Figure 6.5.(a), 1.2×10^6 ions were observed in a bunch with a time spread of 17 μs, whereas in Figure 6.5.(b), the accumulation of 5×10^4 ions resulted in a bunch 5 μs wide.

6.2.2 Gas pressure

The bunch widths were investigated for different values of the buffer gas pressure. Figure 6.6 shows the difference between the photon arrival times for ^{85}Rb ions. In Figure 6.6.(a) the gas pressure was 0.1 mbar, whereas in Figure 6.6.(b), the gas pressure was set at 0.05 mbar. The time spread of the ion bunch were the same in both cases. However, the study showed that less buffer gas induces a later arrival of the ion bunch. The origin of this effect is not understood, since intuitively it would be expected that

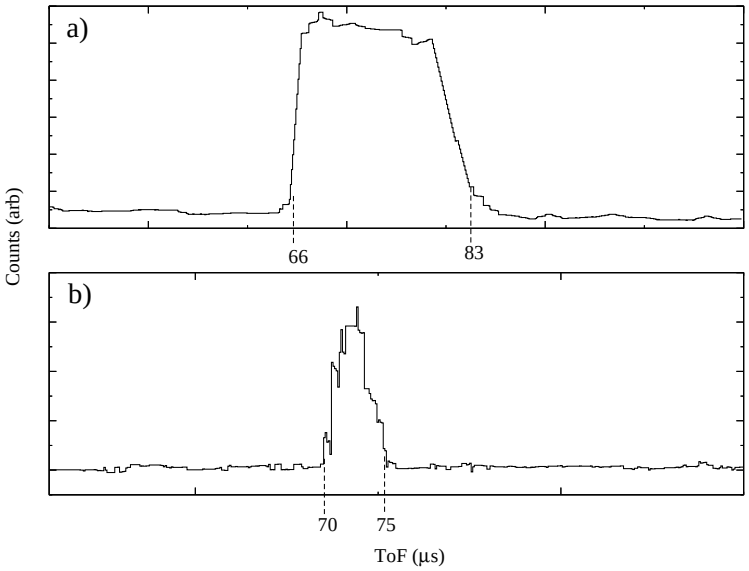

Figure 6.5: Bunch width of ^{85}Rb. The number of ion is the bunch 1.2×10^6 in a), and in b) this number is 5×10^4. The *y* axes are not on the same scale. Adapted from MCS display.

for less buffer gas, the ion bunch would have more energy and therefore would arrive earlier.

6.3 Background suppression

An often used figure of merit to assess the quality of spectral data is the signal-to-noise ratio (S/N). It is defined as the ratio between the signal count, N_S and the standard deviation of the noise count, N_B [87]. In the COLLAPS setup, the dominant source of noise is related to the random laser scatter in the light collection region and dark counts. Therefore

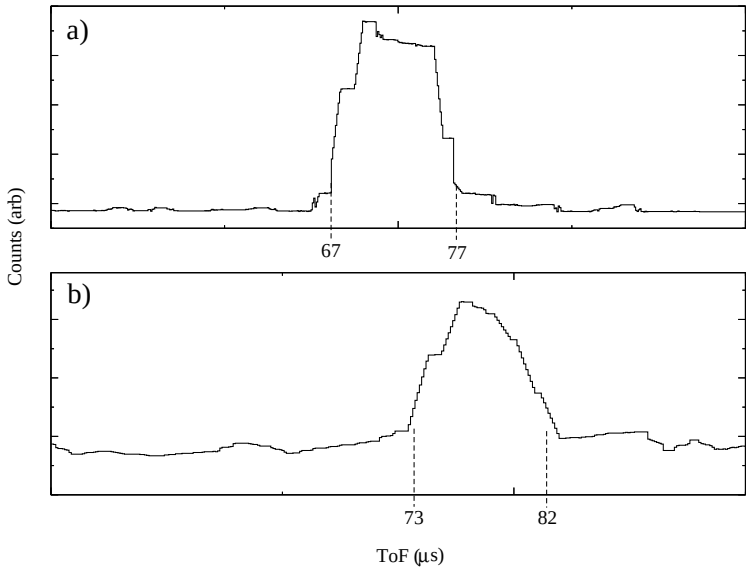

Figure 6.6: Bunch width of ^{85}Rb from the photon arrival times. In a) the buffer gas pressure is 0.1 mbar. In b) the pressure was 0.05mbar, which caused the bunch to arrive later. The *y* axes are not on the same scale. Adapted from MCS display.

$$\begin{aligned} \frac{S}{N} &= \frac{N_S}{\sqrt{N_B}} \\ &= \frac{(\varepsilon \times R_S) \times t}{\sqrt{R_B \times t}} \end{aligned} \tag{6.2}$$

where ε is the detection efficiency, which is a function of the transition strength, the detector efficiency and a geometrical efficiency (solid angle of light collector and laser-ion overlap). The detection efficiency is measured in units of photon/atom. $(\varepsilon \times R_S)$ and R_B are the signal and background rates measured in (photons/s), and t is the data collection time in one channel, measured in seconds.

If all the experimental parameters are fixed during the experiment, longer collec-

tion times are required in order to increase the signal-to-noise ratio. However, due to constraints in beam time allocation, increasing the collection time is often not feasible. In an extreme example, during the on-line commissioning of ISCOOL, $\varepsilon_K \sim 10^{-5}$ and $R_B \sim 5 \times 10^5$photons/s (2 mW of laser power plus dark counts). In order to achieve a $S/N \geq 3$ with an ISOLDE yield of ^{46}K of 10^5 ions/s, it would have been necessary to collect data for at least 28 years to scan across 200 channels, using conventional optical detection techniques. With the modifications implemented in the data acquisition electronics due to ISCOOL, the effective measurement time in a given voltage channel became a fraction of $F = t_w/t_{acc}$ of the dwell time. Therefore, the bunched beam technique is able to suppress the background by a factor of F^{-1} without throwing away any fluorescence-related data.

6.3.1 Rubidium

The first demonstration of bunched-beam spectroscopy was performed on ^{85}Rb ($I = 5/2$). The beam was accelerated to 29.9 keV. The ion current was 2.8×10^7 ions/s measured with a Faraday cup positioned after ISCOOL. The transition chosen was the $S_{1/2} \rightarrow P_{3/2}$ (D_2 line) at 780.24 nm. The hyperfine structure is shown on Figure 6.7.

The accumulation and trap-open times of ISCOOL were 10 ms and 200 μs, respectively. The time width of the ion bunch was 10 μs. Therefore the background suppression factor was $F = 10^3$. Figure 6.8 shows the results of the scans for the gated and ungated spectra. The natural linewidth of the transition is $\delta\nu(\text{nat}) = 6$ MHz. The linewidth obtained from this measurement was $\delta\nu(\text{meas}) = 19$ MHz (which cor-

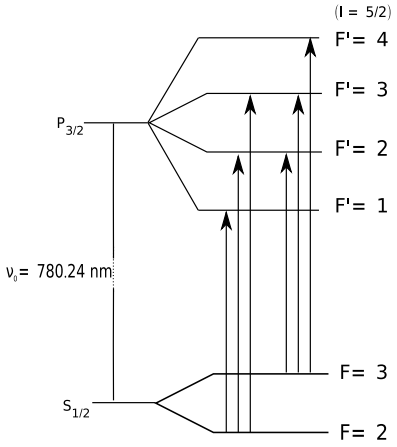

Figure 6.7: Schematic diagram of the hyperfine levels of the D_2 line of ^{85}Rb. The energy levels are not to scale.

responds to 3.4 V). Since the ISCOOL settings and beam energy during these tests were similar to those of the off-line commissioning, it is a valid assumption that the beam emittance was 3.4π mm.mrad. If 27% of the beam passed through the 1 mm aperture, this is equivalent to a circular beam with a Gaussian intensity distribution with a FWHM of 2.5 mm. Therefore the beam angular divergence was approximately 5.4 mrad. Using Equation 3.17, this gives a broadening contribution to the linewidth of $\delta\nu(\theta) \sim 5$ MHz. In order to obtain a crude estimate of the broadening caused by the energy spread $\delta\nu(e)$, the terms are added in quadrature to the natural line, which gives $\delta\nu(e) \sim 17$ MHz. This is is equivalent to an energy spread of $\delta E \approx 3$ eV, since $\frac{\delta\nu'}{\delta V} = 5.5$ MHz/V, by virtue of equation 3.16.

It is worth mentioning that even though this scan was performed with low laser power (0.04 mW), the background count rate was $42,000$ photons/s, most of which was due to dark counts, owing to the fact that the photomultiplier tubes were being operated

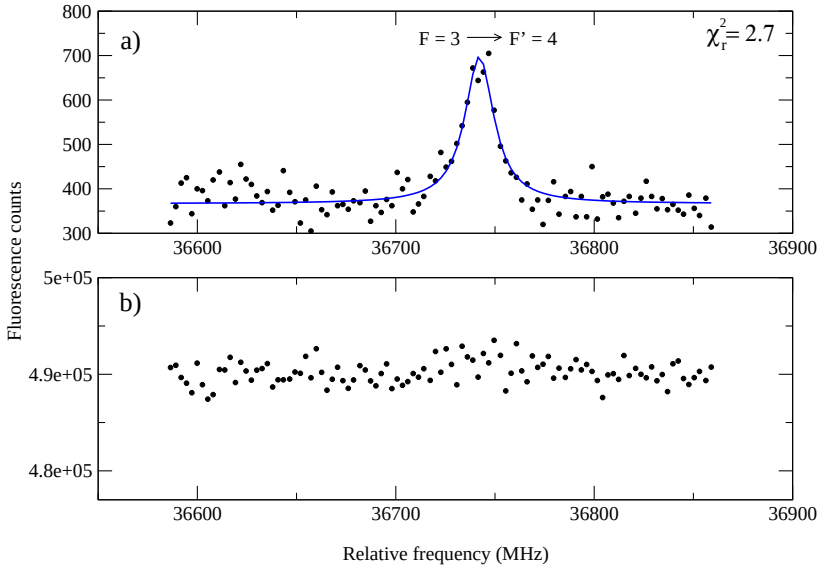

Figure 6.8: Resonance spectra of 2.8×10^7ions/s of ^{85}Rb extracted from ISCOOL and delivered to COLLAPS. After neutralization, the laser excited the $F = 3 \rightarrow F' = 4$ transition. In (a) the hyperfine structure for gated photons, and (b) ungated. The ions were accumulated for 10 ms and the gate width was 10 μs. The FWHM of the peak was 19 MHz. The total scanning time was 3.3 hours.

at ambient temperature. This situation was remedied on the penultimate day of tests, after a chiller unit was placed around the tubes. This radically reduced the dark counts to rates of 150 counts/s. Regrettably, the proton beam had already been interrupted, and therefore no further radioactive tests were possible with these improved conditions.

6.3.2 Potassium

In order to further illustrate the effect of bunching the beam for collinear laser measurements on radioactive beams, scans of the hyperfine structures of ^{44,46}K were per-

formed. After neutralization, the laser excited the D_2 line at 766.49 nm. The hyperfine structure is shown on Figure 6.9.

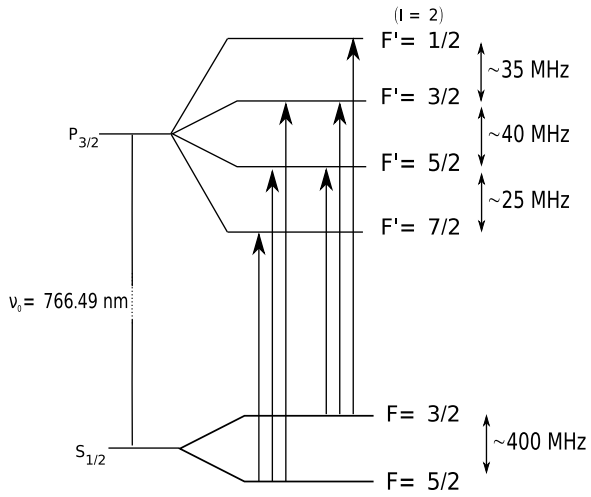

Figure 6.9: Schematic diagram of the hyperfine levels of the D_2 line of ^{44,46}K. The frequency difference between the hyperfine levels are indicated. Both isotopes have a ground state spin $I = 2$. The values for the A factors were taken from [88]. For the B factors, see text. The energy levels are not to scale.

Figures 6.10 and Figures 6.11 compare the scanned hyperfine spectra of ^{44,46}K for ungated and gated photons. The background suppression factors were $F(^{44}K) = 10^4$ and $F(^{46}K) = 2.5 \times 10^4$.

Both figures show that the 6 hyperfine components could not be fully resolved. The FHWM of the resonances were ~ 50 MHz, and therefore larger than the splittings of the hyperfine structure multiplets shown in Figure 6.9. For instance, what seems to be a single peak on the right hand side of Figures 6.10.(a) is actually composed of three fluorescence lines resulting from the excitation of $F = 5/2 \rightarrow F' = 7/2$, $F = 5/2 \rightarrow F' = 5/2$ and $F = 5/2 \rightarrow F' = 3/2$ transitions. Likewise, the peaks from

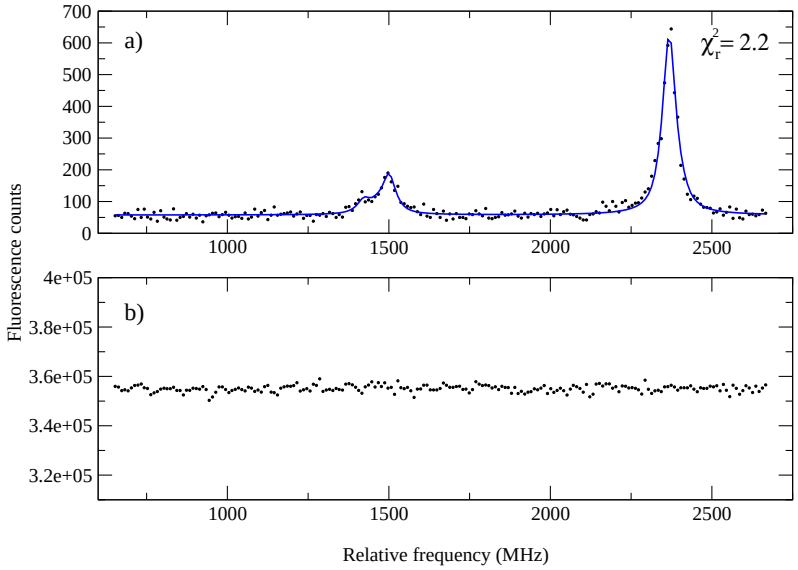

Figure 6.10: Resonance spectra of 6.4×10^5 ions/s of ^{44}K. In (a) the hyperfine structure for gated photons, and (b) ungated. The fitted line is in blue. The FWHM of each peak was $48(1)$ MHz. The ions were accumulated for 100 ms and the gate width was 10 μs. The laser power was 0.04 mW. The total scanning time was 33 minutes.

the excitations of $F = 3/2 \rightarrow F' = 5/2$, $F = 5/2 \rightarrow F' = 3/2$ and $F = 3/2 \rightarrow F' = 1/2$ compose the collapsed structure observed on the left. The observed intensity of the peaks corresponding to transitions between hyperfine multiplets $F \rightarrow F'$ did not follow Racah values (Equation 2.18). A fitting code based on χ^2 minimisation was written by the author of this thesis in order fit the observed data, which takes this effect into account by letting the peak intensities run as free fitting parameters. The code was written in C++, using the ROOT framework [89]. This offered several advantages, the main one being that the fitting method is based on the standard CERN-MINUIT library and is already implemented as a member function of ROOT function classes. In the

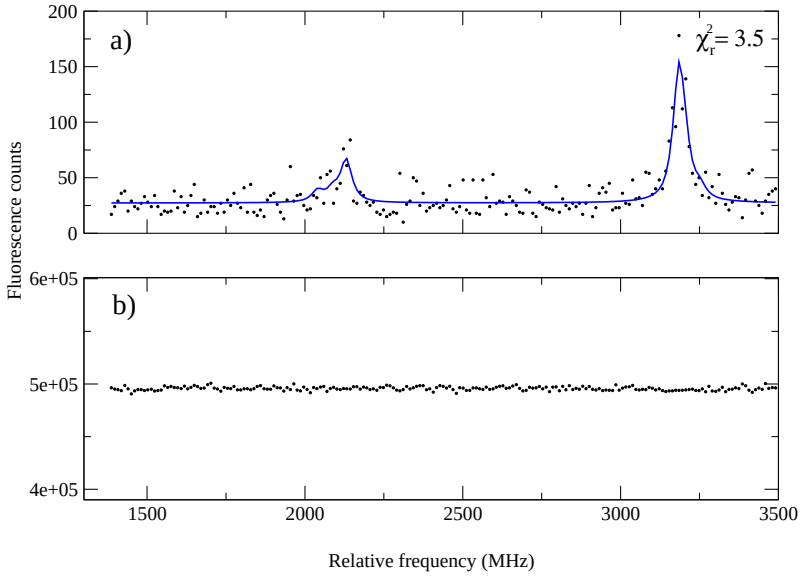

Figure 6.11: Resonance spectra of 10^5 ions/s of ^{46}K. In (a) the hyperfine structure for gated photons, and (b) ungated. The fitted line is in blue. The FWHM of each peak was 42(6) MHz. The ions were accumulated for 300 ms and the gate width was 12 μs. The laser power was 0.04 mW. The total scanning time was 22 minutes.

code, the ROOT class TGraphErrors was used. This class automatically provides the errors of each fitting parameter. In order to fit the spectrum, the hyperfine coefficient $A\,(S_{1/2})$ was fixed to literature values [88], while the value for $A\,(P_{3/2})$ was constrained using Equation 2.15. The ratio r could be calculated using figures found in [90] and [88]. A realistic lineshape for the hyperfine transitions is the Voigt profile, which is a convolution of a Gaussian and Lorentzian lineshapes. However, in order to reduce the computational time involved in the χ^2 minimization, each peak was fitted to a pseudo Voigt profile, which consisted of a weighted sum of Gaussian and Lorentzian lineshapes with different widths, as described by Bruce [91]. The resulting error of such

Table 6.1: Hyperfine structure coefficients $B\ (P_{3/2})$ and static quadrupole moments of ^{44,46}K.

A	B $P_{3/2}$ (MHz)	Q(b)
44	$+25 \pm 1.5$	$+0.52 \pm 0.3$
46	$+27.4 \pm 5.4$	$+0.57 \pm 0.11$

an approximation is $\sim 1\%$ in terms of the lineshape amplitude. The hyperfine constant $B\ (P_{3/2})$ together with the peak intensities were left as free fitting parameters. The same procedure was adopted for ^{46}K. This allowed the hyperfine coefficients $B\ (P_{3/2})$ to be measured for the first time. Once the $B\ (P_{3/2})$ hyperfine parameters were obtained, it was straightforward to extract the static spectroscopic quadrupole moments, by making use of Equation 2.20, with ^{39}K as the reference isotope. The values of the B_{ref} and Q_s^{ref} were found in [90] and [92]. Table 6.1 summarises the results. It is interesting that the data show a large B factor, albeit with low statistics. The investigation on the moments of neutron-rich potassium isotopes is the subject of a new experimental proposal, which has been approved and will take place at CERN-ISOLDE [93].

6.4 Summary

These tests account for the first demonstration of bunched beam spectroscopy with ISCOOL, and clearly show that the device has been successfully commissioned on-line. The tests also provided a starting point to find the optimal beam transport conditions in order to bring the ions to the COLLAPS line with minimal losses. The first on-line experiment using this technique was subsequently performed on neutron-rich gallium

isotopes, which is the subject of the next chapter.

CHAPTER 7

LASER SPECTROSCOPY OF GALLIUM ISOTOPES

7.1 Introduction

Following the encouraging results obtained during the on-line commissioning of ISCOOL, laser spectroscopy using cooled and bunched beams was applied for the first time in the study of neutron rich gallium isotopes. The study was a realisation of the IS457 proposal [94], and took place from the 29th of June to the 4th of July 2008. In total, 7 shifts were allocated for the initial experiment, but in effect 5 shifts were the net data collection time, due to interruptions to the proton beam. The experiment measured the hyperfine structures of $^{67-79}$Ga. This chapter presents the data set obtained and the methodology which has been developed in order to analyse the data. The analysis of the spectra allowed the spins, and hyperfine coupling constants to be determined.

7.2 Experimental details

The only stable isotopes of gallium are $A = 69$ and $A = 71$. For this experiment, a uranium carbide target unit was used (UC375) to produce neutron-rich gallium iso-

topes. The target material was 46 g/cm^2 uranium carbide, and the unit was equipped with a Nb cavity. This unit had been previously used for the production of Mn isotopes between the 10th and 29th of June 2008. During the gallium run, the target received typically half of the 40 proton pulses in a super cycle. Typically 3×10^{13} protons per pulse were delivered with an energy of 1.4 GeV. The time between each pulse had a duration of 1.2 s, totalling an average proton current of 2 μA. The RILIS photoionization setup was requested and Ga^+ was produced with an efficiency of 21% [95]. Yield measurements were performed for some isotopes with a tape station and a β counter. In those measurements, the target and line were heated with 600 and 250 A (1900° and 1900° C, respectively). Table 7.2 shows the half-lives and yields of the isotopes studied.

At this stage, all ISCOOL controls, including HV, radiofrequency and gas had been fully integrated to the ISOLDE controls network. The HRS and ISCOOL voltages were set to 50060 V and 49900 V, respectively. The platform voltage of the cooler was measured with a FUG HTV 65000 high voltage divider, which was connected to a Keithley DMM 2000 electronic display. The divider ratio was 10000 : 1. This device was calibrated against a divider used for the HRS power supply, which resulted in a readout accuracy of ± 1 V. The radiofrequency and amplitude of the trap were set to $\omega = 360$ kHz and $V_{rf} = 420$ V_{0-p} for all masses. The buffer gas pressure was 0.1 mbar. With these settings, the transmission efficiency of ISCOOL in continuous mode was $> 60\%$. In bunched mode, typical accumulation times were between 10 ms and 50 ms. The temporal width of the ion bunches were 20 μs -25 μs. The accumulation times

Table 7.1: Summary of half-lives and yields of Ga isotopes from an UCx target. The yields are given in units of ions/μ C.

A	$T_{1/2}$	Yield (literature)[a]	Yield (IS457)
67	3.2 d	–	
68	67.62 m	9.0×10^6	
69	stable	–	
70	21.14 m	2.5×10^7	
71	stable	–	
72	14.1 h	5.3×10^7	
73	4.86 h	4.8×10^5	1.8×10^9
74	8.12 m	3.9×10^7	9.8×10^8
75	126 s	3.1×10^7	2.4×10^8
76	32.6 s	1.3×10^7	
77	13.2 s	7.7×10^6	
78	5.09 s	3.9×10^6	5.0×10^7 [b]
79	2.84 s	2.6×10^6	3.0×10^7 [b]

[a] Taken from [96, 97]. There is a mistake in the quoted yield for ^{73}Ga.
[b] Extrapolated value.

used were shorter than during the on-line commissioning. This was due to the fact that there was a significant Rb isobaric contamination, up to two orders of magnitude higher than the Ga yield.

The low-lying atomic levels of Ga are shown in Figure 7.1. This diagram focuses on the levels involved in the photoionization of gallium in addition to the levels used to perform the subsequent collinear laser work. The recent upgrade of RILIS from a copper-vapour to a solid-state pump laser system provided an improvement on the final yield, since it permitted simultaneous excitation of the low-lying $^2P_{1/2}$ and $^2P_{3/2}$ states, which are almost equally populated. Moreover, this upgrade allowed more green (532

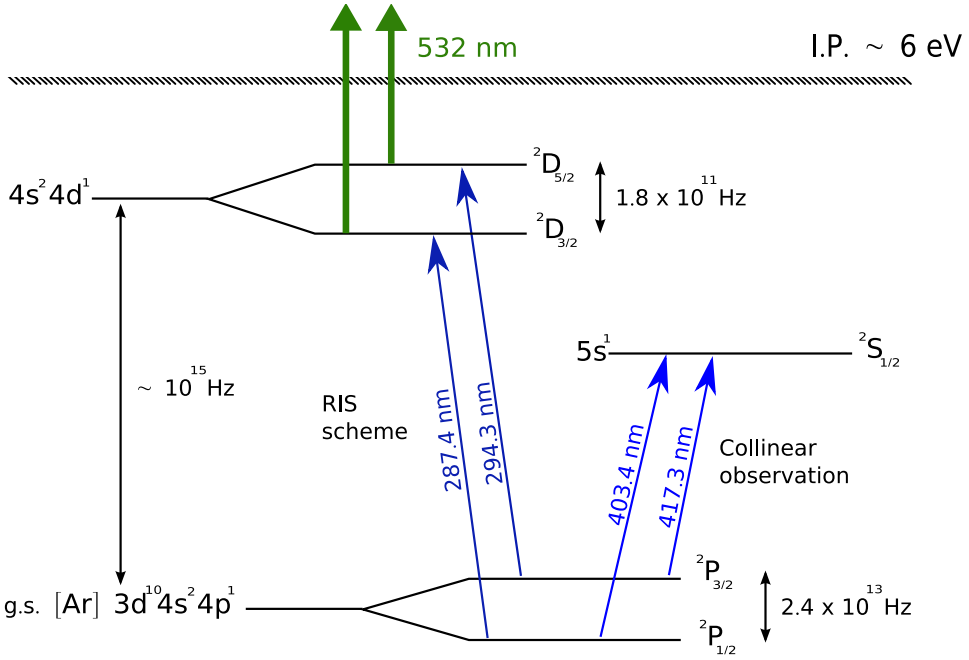

Figure 7.1: The low-lying levels of atomic gallium [98].

nm) power to be used in the final step. All in all, a relative improvement by a factor of 2 was achieved for the final Ga yield.

In order to neutralize the Ga^+ in the COLLAPS line, the charge-exchange cell was filled with sodium vapour. The temperature at the cell centre was around 250° C. With the exception of ^{69,75,76}Ga, all the other isotopes had the hyperfine structure measured in both $^2P_{1/2} \rightarrow ^2 S_{1/2}$ (403 nm) and $^2P_{3/2} \rightarrow ^2 S_{1/2}$ (417 nm) transitions. The natural linewidth of both transitions is $\sim$ 25 MHz. The branching ratios of the decays are 33% and 67%, respectively. The Ti:Sa was pumped with a Coherent Verdi V18 laser, with 15 W of pump power. The fundamental laser power was 1 W and the power of the doubled light was $0.3 - 1.5$ mW. The fundamental wavelength was monitored with a HighFinesse wavemeter with an accuracy of 3 MHz.

The data acquisition was implemented in a similar way to the scheme developed during the on-line commissioning, except that this time the trigger used to open the trap originated from the data acquisition software. The modification is shown in Figure 7.2. It is important to mention that both photomultiplier tubes suffered from multiple ringing associated with the photon signal, which could lead the data acquisition arrangement to double-count or multiple count photon events. This undesirable effect seems to be related to an impedance mismatch between the PMT and the impedance of the external load [99]. This was a recurrent problem, which was also observed during the on-line commissioning. In the IS457 experiment, this problem was dealt with by applying a dead time on the Ortec 416A gate and delay generator placed after the discriminator module. In this way, the detection of one photon event would veto any subsequent events possibly related to the spurious ringing signal for at least 11 μs, as exemplified in Figure 7.3. In this example two photons would fall within the 20 μs time window and would be counted in the channel.

7.3 Data analysis

At a glance, Figure 7.4 shows all the measured isotopes. The background suppression factor was equal to 10^3. During the experiment, several short scans were performed for each isotope, in order to determine the scan position and range. Measurement times for each spectrum in the full range took from 1 minute to 30 minutes. The FWHM of the peaks in the $P_{3/2} \rightarrow S_{1/2}$ transition was $\sim$ 75 MHz, whereas in the $P_{1/2} \rightarrow S_{1/2}$ transition it was $\sim$ 65 MHz. An important procedure adopted during the experiment

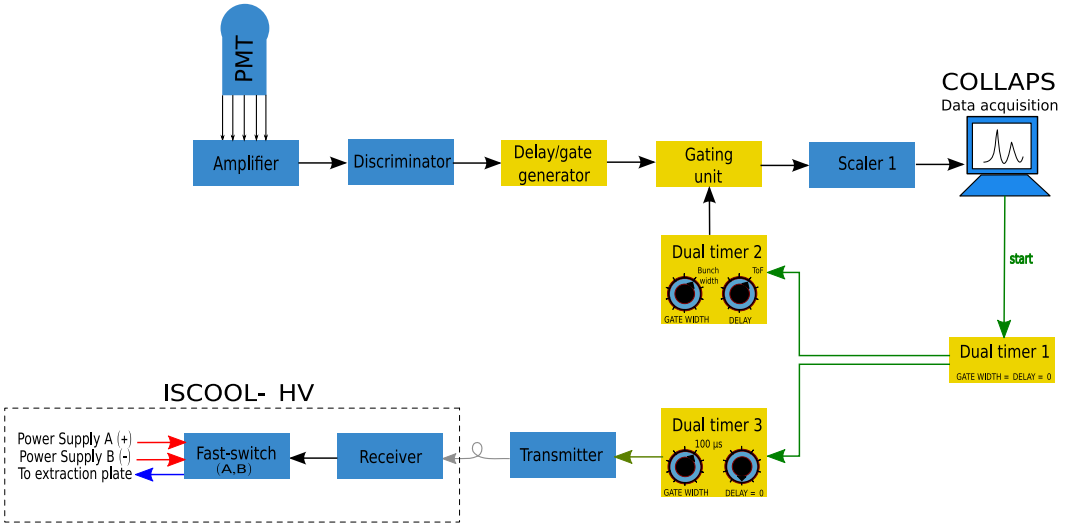

Figure 7.2: Diagram of the electronics for the bunched beam mode of acquisition used in the Ga run, with the data acquisition running in “active” mode.

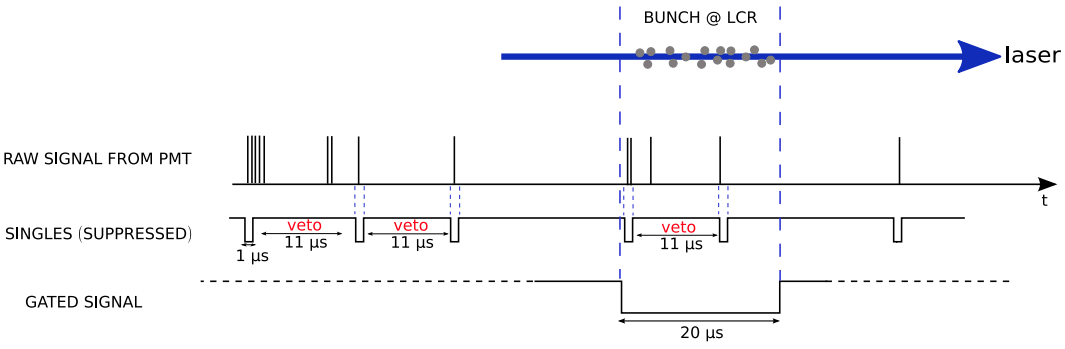

Figure 7.3: Timing of signals for bunched beam spectroscopy.

was to make a scan of a reference stable isotope in between every change of mass in the separator. This was intended to detect any drifts in the centroids of the transitions, due to drifts in the laser frequency or high voltage.

In the cases where the isotopes had the hyperfine structures measured in both $P_{1/2} \rightarrow S_{1/2}$ and $P_{3/2} \rightarrow S_{1/2}$ transitions, the methodology used for analysing the datasets consisted of a combined approach. A fitting code based on the code used to fit the on-line commissioning data was written by the author of this thesis to fit both spectra simultaneously in order to find a single χ^2_{min} in χ^2 multidimensional parameter space. This approach proved to be advantageous, because in those cases the transitions had the same hyperfine coupling constant $A\ (S_{1/2})$. Therefore, the number of fitting parameters was reduced by one and the final fit had a global χ^2 for both spectra, with a reduced error for the B hyperfine constant associated with the $P_{3/2}$ state.

It should also be mentioned that in this work an accurate determination of the magnitude of the isotope shifts was not possible due to drifts in the laser frequency and in the acceleration voltages. Taken together these effects could therefore have introduced systematic uncertainties which are difficult to quantify. In the second round of experiments which took place in May 2009, it was possible to implement short-term stabilisation of the laser. Most of the isotopes presented in this thesis were remeasured. The isotope shifts obtained from this data set are currently under analysis, and will not take part of the discussion presented in this thesis.

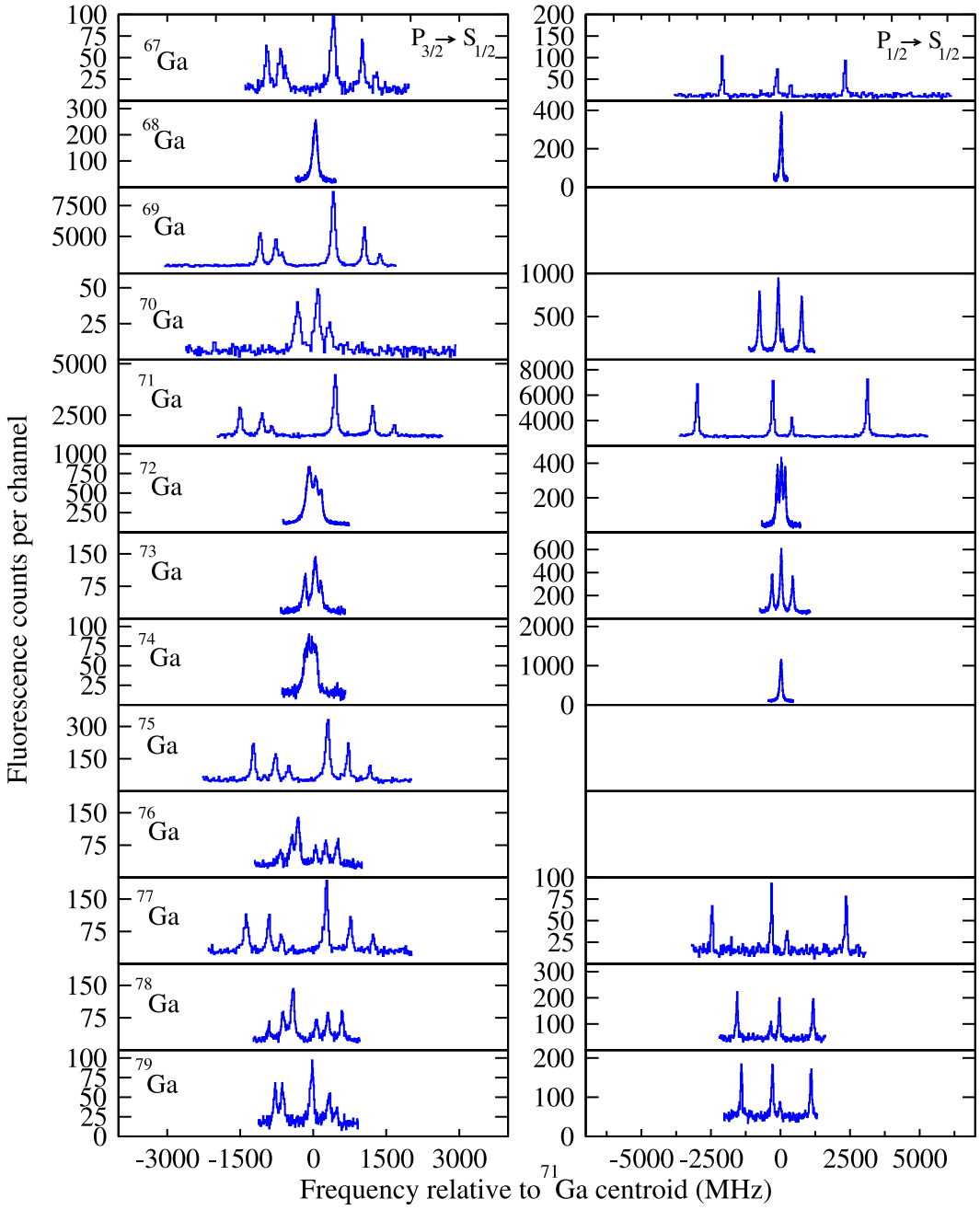

Figure 7.4: The dataset obtained in the IS457 run.

Table 7.2: Table summarizing the measured spin and hyperfine structure coupling constants of ^{67}Ga. All values are in MHz. All values are positive, unless stated otherwise. This is the convention used hereafter.

A	Source	I	$A\ (P_{1/2})$	$A\ (S_{1/2})$	$A\ (P_{3/2})$	$B\ (P_{3/2})$
^{67}Ga	This work	$3/2$	1225.8 ± 2.3	980.3 ± 1.6	176.3 ± 1.1	73.0 ± 3.3
	Ref. [100]	$3/2$	1228.86582	–	175.09736	71.95750
			± 0.00045		± 0.00015	± 0.00055

^{67}Ga

The hyperfine structure of this isotope was measured with the $P_{1/2} \rightarrow S_{1/2}$ (403 nm) and $P_{3/2} \rightarrow S_{1/2}$ (417 nm) transitions. The spectra are shown in Figure 7.5. For the $P_{1/2} \rightarrow S_{1/2}$ transition, the fitting parameters were the background, the centroid for the transition, $A\ (P_{1/2})$, $A\ (S_{1/2})$, and 4 pseudo Voigt profiles with a common width and free intensities, as described in section 6.3.2. For the $P_{3/2} \rightarrow S_{1/2}$ transition, similar parameters were fitted, including the $A\ (P_{3/2})$ and $B\ (P_{3/2})$ coupling constants. The function to be fitted had in total 22 free parameters. The fit allowed the $A\ (S_{1/2})$ hyperfine coupling constant to be determined for the first time. The results obtained are consistent with previously published values, as shown on Table 7.2.

An independent investigation was undertaken in order to assess the reliability of the error estimates given by the ROOT fitting engine in the combined analysis approach. This investigation was based on an algorithm which worked with the χ^2_{min} found by MINUIT. The algorithm, written in C++, basically froze the parameter for which the $1\ \sigma$ error was sought. An incremental perturbation was then introduced on this parameter and the χ^2 was re-evaluated, letting all the remaining fitting parameters free. As

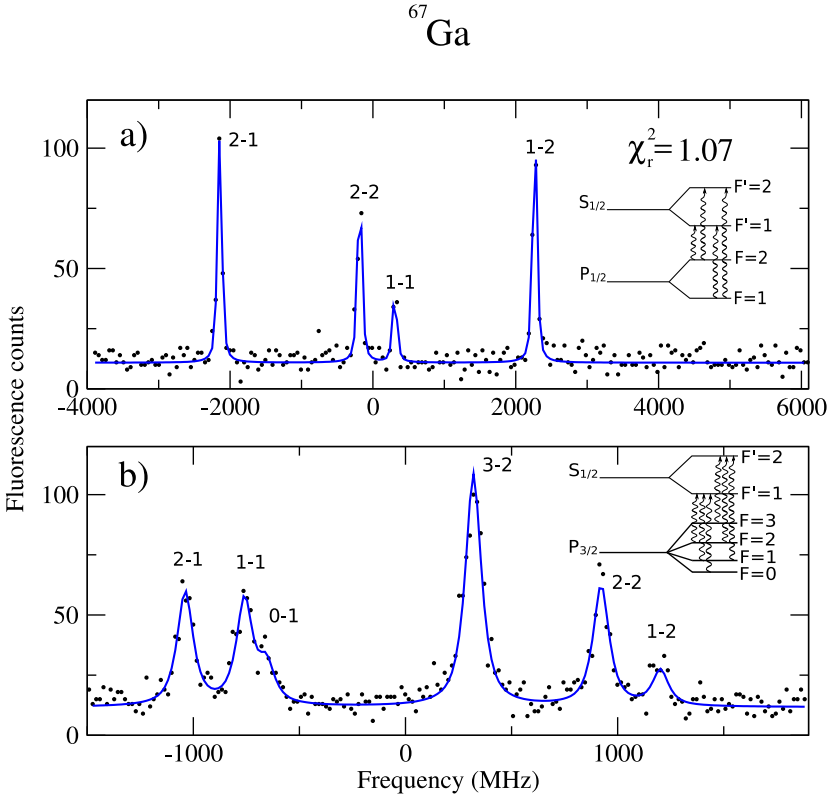

Figure 7.5: The hyperfine structure of $I = 3/2$ ground state for ^{67}Ga in the a) $P_{1/2} \rightarrow S_{1/2}$ and b) $P_{3/2} \rightarrow S_{1/2}$ transitions. The blue line indicates the fitted data, which was obtained from a simultaneous minimization of χ^2 for both spectra.

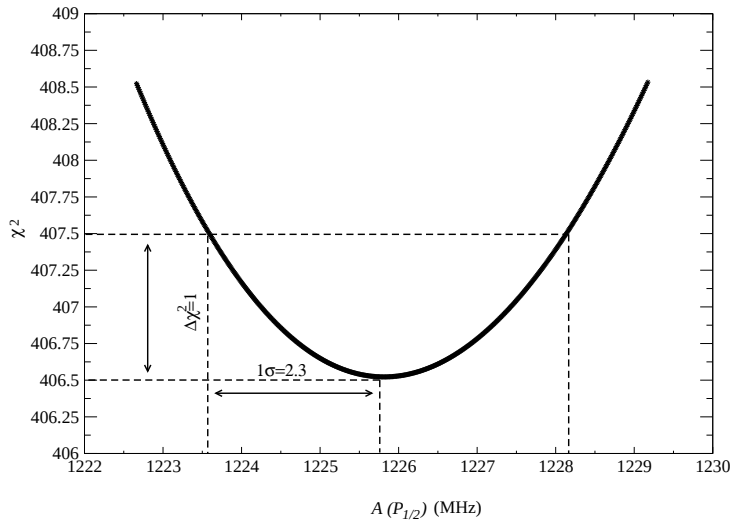

Figure 7.6: A cut on the χ^2 hypersurface against the $A\ (P_{1/2})$ parameter for the simultaneous fitting of ^{67}Ga in the $P_{1/2} \rightarrow S_{1/2}$ and $P_{3/2} \rightarrow S_{1/2}$ transitions.

an illustration, the $A\ (P_{1/2})$ hyperfine constant in the combined analysis approach was scrutinised. The result is shown in Figure 7.6. In this plot there are 651 data points which clearly fit a parabola.

A search on these data points in order to find a χ'^2_{min} which is smaller than χ^2_{min} show that indeed the output χ^2_{min} given by ROOT was the global minimum. The 1 σ error for the parameter was obtained from the condition $\Delta\chi^2 = 1$, as prescribed by [101, 102], and was found to be consistent with the error estimate of ROOT.

^{68}Ga

The spectra of ^{68}Ga were also measured for the $P_{1/2} \rightarrow S_{1/2}$ and $P_{3/2} \rightarrow S_{1/2}$ transitions, as shown in Figure 7.7. However, what is immediately noticeable is that both

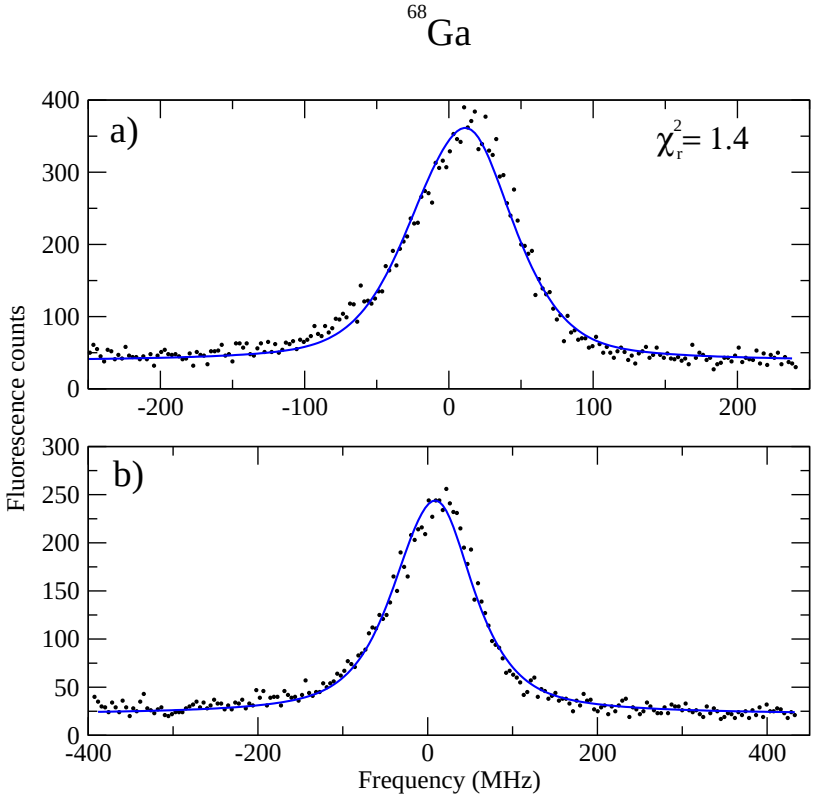

Figure 7.7: The hyperfine structure of $I = 1$ ground state for ^{68}Ga at the a) $P_{1/2} \rightarrow S_{1/2}$ and b) $P_{3/2} \rightarrow S_{1/2}$ transitions. The blue line indicates the fitted data, which was obtained from a simultaneous minimization of χ^2 for both spectra.

Table 7.3: Table summarizing the measured spin and hyperfine structure coupling constants of ^{69}Ga. All values are in MHz.

A	Source	I	$A\ (P_{1/2})$	$A\ (S_{1/2})$	$A\ (P_{3/2})$	$B\ (P_{3/2})$
^{69}Ga	This work	$3/2$	–	1070.9 ± 0.5	191.9 ± 0.2	61.7 ± 0.7
	Ref. [103]	$3/2$	1339	1069	190.8	62.5
	Ref. [39]	$3/2$	1339 ± 2	1075 ± 3	–	–

structures have completely collapsed due to the small hyperfine coupling constants. From this dataset, not even the sign of the hyperfine coefficients could be determined. In fact, during the fitting process, the hyperfine coefficients $A\ (P_{3/2})$ and $B\ (P_{3/2})$ were scaled to published values of the magnetic and quadrupole moments [18] via Equations 2.19 and 2.20, using ^{71}Ga as reference. The values of $A\ (S_{1/2})$ and $A\ (P_{1/2})$ were fixed to the ratios of ^{71}Ga, calculated from Equation 2.15,

$$r_{417} = \frac{A\ (S_{1/2})}{A\ (P_{3/2})} = +5.591 \pm 0.001, \tag{7.1}$$

$$r_{403} = \frac{A\ (S_{1/2)}}{A\ (P_{1/2})} = +0.798 \pm 0.002. \tag{7.2}$$

^{69}Ga

This isotope was only measured in the $P_{3/2} \rightarrow S_{1/2}$ transition. Figure 7.8 shows the data and fitted spectrum. Table 7.3 summarizes the hyperfine constants obtained from the fit together with previously published values. It shows that the values for the hyperfine constants of the current study are consistent with those of previous measurements.

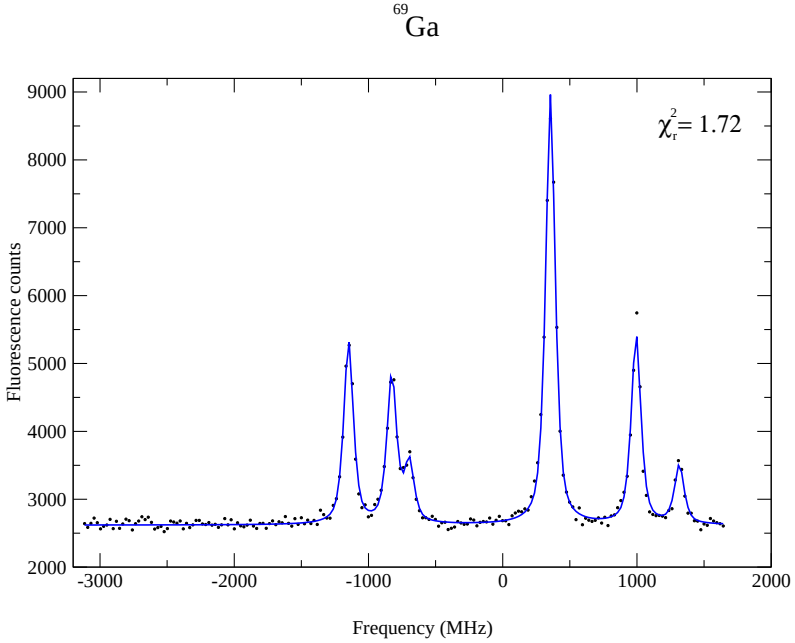

Figure 7.8: The hyperfine structure of $I = 3/2$ ground state for ^{69}Ga measured in the $P_{3/2} \rightarrow S_{1/2}$ transition. The blue line indicates the fitted data, which was obtained from a χ^2 minimization routine.

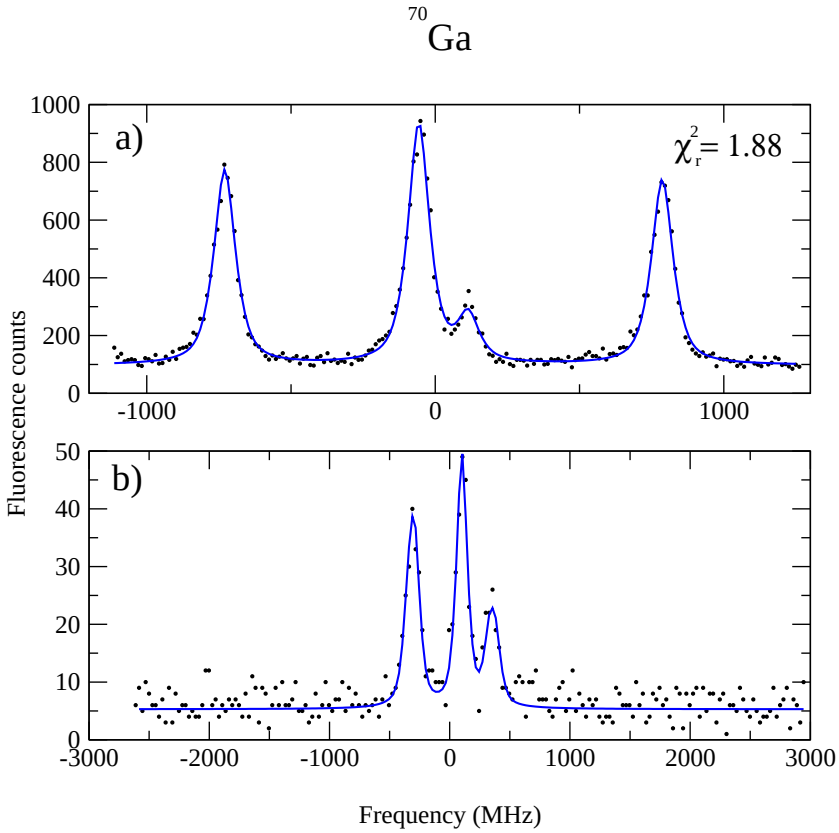

Figure 7.9: The hyperfine structure of $I = 1$ ground state for ^{70}Ga at the a) $P_{1/2} \rightarrow S_{1/2}$ and b) $P_{3/2} \rightarrow S_{1/2}$ transitions. The blue line indicates the fitted data, which was obtained from a simultaneous minimization of χ^2 for both spectra.

^{70}Ga

As Figure 7.9 shows, this isotope was measured in both transitions. Table 7.4 summarizes the fitted hyperfine constants. Note that this is the first time that these observables have been measured. The ground state spin $I = 1$ has also been confirmed. The large uncertainty in the coefficients of the $P_{3/2} \rightarrow S_{1/2}$ transition was caused by its almost collapsed structure.

Table 7.4: Table summarizing the measured spin and hyperfine structure coupling constants of ^{70}Ga. All values are in MHz.

A	Source	I	$A\,(P_{1/2})$	$A\,(S_{1/2})$	$A\,(P_{3/2})$	$B\,(P_{3/2})$
^{70}Ga	This work	1	562.5 ± 0.6	448.5 ± 0.6	76.9 ± 2.8	28.9 ± 9

^{71}Ga

This isotope was chosen to be the reference during the calibration scans. Therefore, several spectra were produced from scans performed on both transitions. Figure 7.10 shows an example of the simultaneously fitted spectra for a given dataset of ^{71}Ga runs (runs #21 and #48, respectively).

Due to the large number of calibration scans, it was possible to verify whether there were any systematic effects in the error estimate of the hyperfine coupling constants. For the purpose of this analysis the spectra from the $P_{1/2} \rightarrow S_{1/2}$ and $P_{3/2} \rightarrow S_{1/2}$ transitions were fitted separately. The error weighted average, $\bar{x}$, of a set of parameters x_i measured with an error σ_i can be computed using Equation 7.3 [104]

$$\bar{x} = \frac{\sum_i x_i w_i}{\sum_i w_i}, \tag{7.3}$$

where $w_i = 1/\sigma_i^2$ is the weight factor. The error on the average, $\bar{\sigma}_x$ is calculated from Equation 7.4

$$\bar{\sigma}_x = \frac{1}{\sqrt{\sum_i wi}} \tag{7.4}$$

Figure 7.11 shows the results for the $P_{1/2} \rightarrow S_{1/2}$ transition. The error weighted average

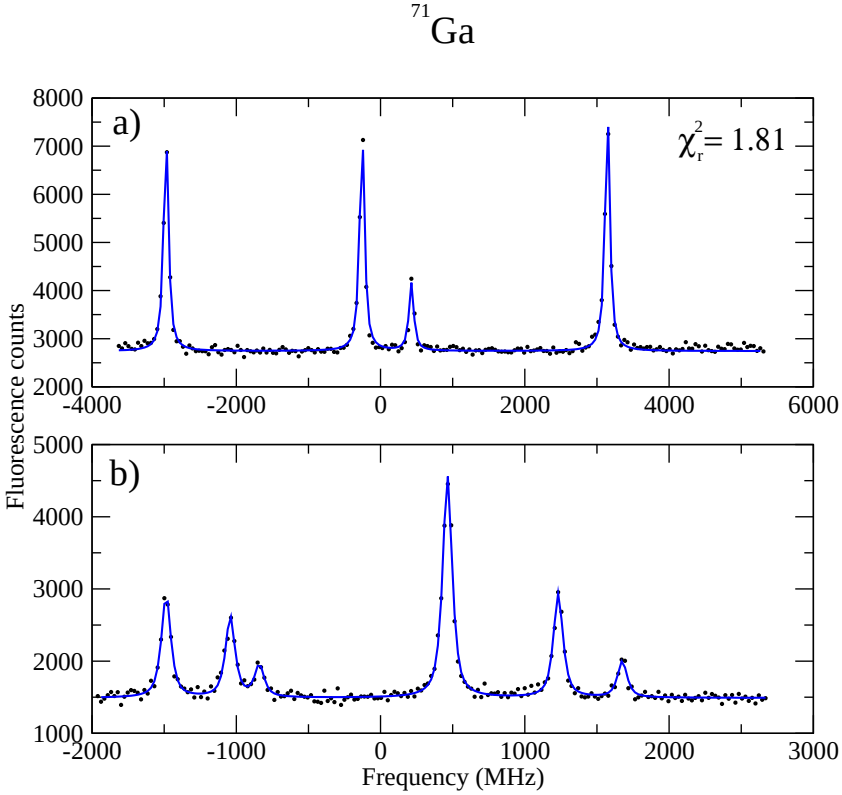

Figure 7.10: The hyperfine structure of $I = 3/2$ ground state for ^{71}Ga at the a) $P_{1/2} \rightarrow S_{1/2}$ and b) $P_{3/2} \rightarrow S_{1/2}$ transitions. The blue line indicates the fitted data, which was obtained from a simultaneous minimization of χ^2 for both spectra.

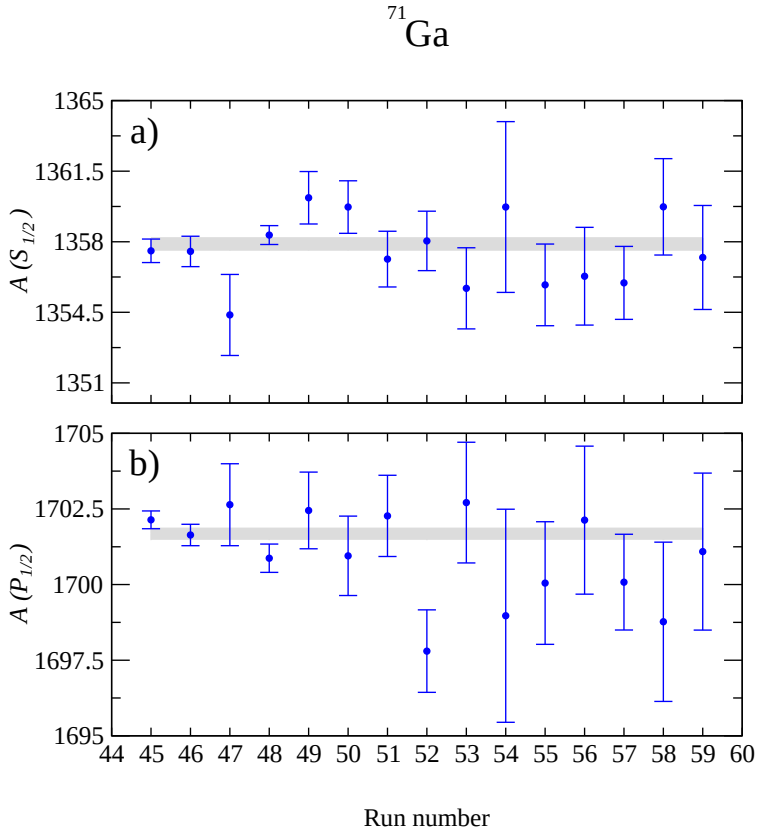

Figure 7.11: Fitted hyperfine coefficients a) $A\ (S_{1/2})$ and b) $A\ (P_{1/2})$ for ^{71}Ga for different run numbers. The grey lines indicate the error weighted average. The thickness of the line indicates the error of the mean.

for the $A\ (S_{1/2})$ coefficient was calculated to be 1357.9 ± 0.3 MHz. Analogously, for the $A\ (P_{1/2})$ coefficient the average was 1701.7 ± 0.2 MHz. To determine whether these numbers followed a normal distribution and hence whether the effect of systematic errors was negligible, a χ^2 analysis was performed with respect to the averaged mean, according to Equations 7.5

Table 7.5: Table summarising the f factors for each hyperfine structure coupling constants of ^{71}Ga in the $P_{1/2} \rightarrow S_{1/2}$ transition.

Coefficient	f
$A\ (S_{1/2})$	1.02
$A\ (P_{1/2})$	1.21

$$\begin{aligned} \chi^2 &= \sum_i^N \frac{(\bar{x}-x_i)^2}{\sigma_i^2} \\ \chi'^2 &= \sum_i^N \frac{(\bar{x}-x_i)^2}{(f\times\sigma_i)^2} = N_{dof}\ , \end{aligned} \tag{7.5}$$

where N_{dof} is the number of degrees of freedom, defined as the number of free fitting parameters (N) minus one, $N_{dof} = N-1$. The multiplicative factor f could be determined by manipulating equation 7.5, giving $f = \sqrt{\chi^2/N_{dof}}$. If $f \sim 1$, it would mean that $\chi^2 \sim N_{dof}$, and therefore, the fitted hyperfine constants followed a normal distribution; otherwise, the f factor would determine the scaling factor to be applied to the errors. For instance $f < 1$ would mean the errors were overestimated by the fitting program; conversely, $f > 1$ would suggest the errors were underestimated. The results of this analysis, summarised on Table 7.5, show that $f \sim 1$ and therefore suggest that the numbers are indeed normally distributed, without the necessity of any scaling to be applied to the final errors.

A similar study was conducted for the hyperfine constants of the $P_{3/2} \rightarrow S_{1/2}$ transition. Figure 7.12 shows the results. The error weighted average for the $A\ (S_{1/2})$, $A\ (P_{3/2})$ and $B\ (P_{3/2})$ coefficients were calculated to be 1358.1 ± 0.2 MHz, 242.9 ± 0.1

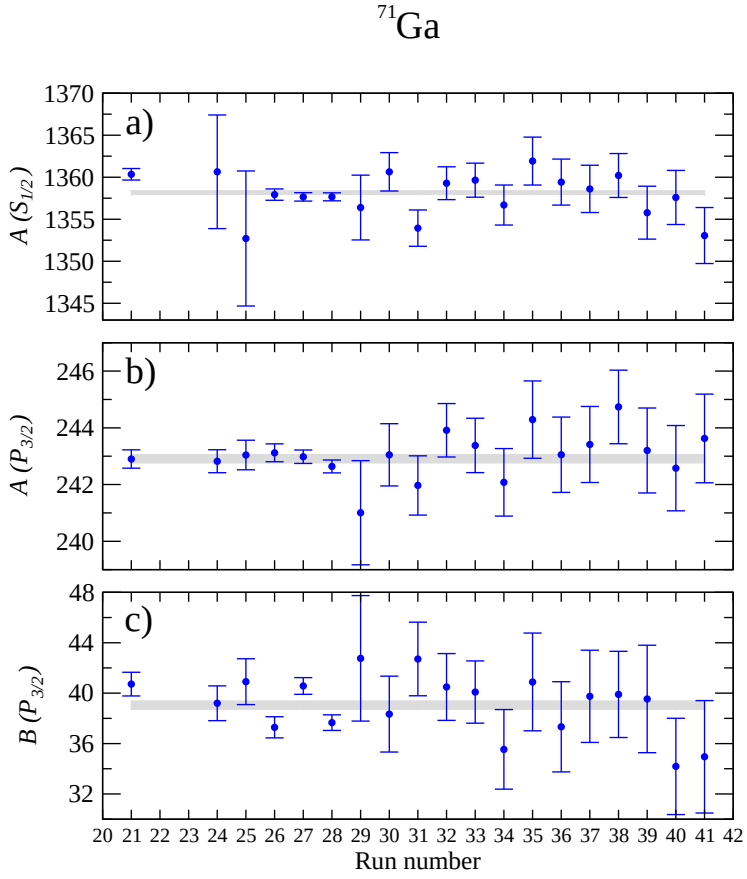

Figure 7.12: Fitted hyperfine coefficients a) $A\ (S_{1/2})$, b) $A\ (P_{3/2})$ and c) $B\ (P_{3/2})$ for ^{71}Ga for different run numbers. The grey lines indicate the error weighted average. The thickness of the line indicates the error of the mean.

MHz and 39.05 ± 0.33 MHz, respectively. A summary of the χ^2 analysis is shown on Table 7.6. Finally, the values for the hyperfine coupling constant $A\ (S_{1/2})$ was obtained from the weighted averages from the different datasets, as shown in Table 7.7. Again, there is excellent agreement between the measurements of the hyperfine constants from this work and previously published values.

Table 7.6: Table summarising the f factors for each hyperfine structure coupling constants of ^{71}Ga in the $P_{3/2} \rightarrow S_{1/2}$ transition.

Coefficient	f
$A\ (S_{1/2})$	1.18
$A\ (P_{3/2})$	0.72
$B\ (P_{3/2})$	1.2

Table 7.7: Table summarising the measured spin and hyperfine structure coupling constants of ^{71}Ga. All values are in MHz.

A	Source	I	$A\ (P_{1/2})$	$A\ (S_{1/2})$	$A\ (P_{3/2})$	$B\ (P_{3/2})$
^{71}Ga	This work	3/2	1701.7 ± 0.2^a	1358.04 ± 0.19^b	242.9 ± 0.1^c	39.05 ± 0.33^c
	Ref. [103]	3/2	1701	1358	242.4	39.4
	Ref. [39]	3/2	–	1358 ± 0.04	–	–

[a] Weighted average based on 403 nm calibration runs
[b] Weighted average based on 403 nm and 417 nm calibration runs
[c] Weighted average based on 417 nm calibration runs

^{72}Ga

The hyperfine structure of this isotope was measured in both transitions. Figure 7.13 shows the simultaneous fit of the scan performed on the $P_{1/2} \rightarrow S_{1/2}$ transition against several spectra from runs performed on the $P_{3/2} \rightarrow S_{1/2}$ transition. The fit allowed the $A\ (S_{1/2})$ hyperfine constant to be freely determined with a value consistent with the ratio given by Equation 7.2. Despite the consistency in the determination of the $B\ (P_{3/2})$ constant, as shown by Table 7.8, this value is not in agreement with the previously published value of Ehlers *et al.* [100]. However, in the same work the authors published a value for $A\ (P_{1/2})$, which is consistent with the findings from the combined

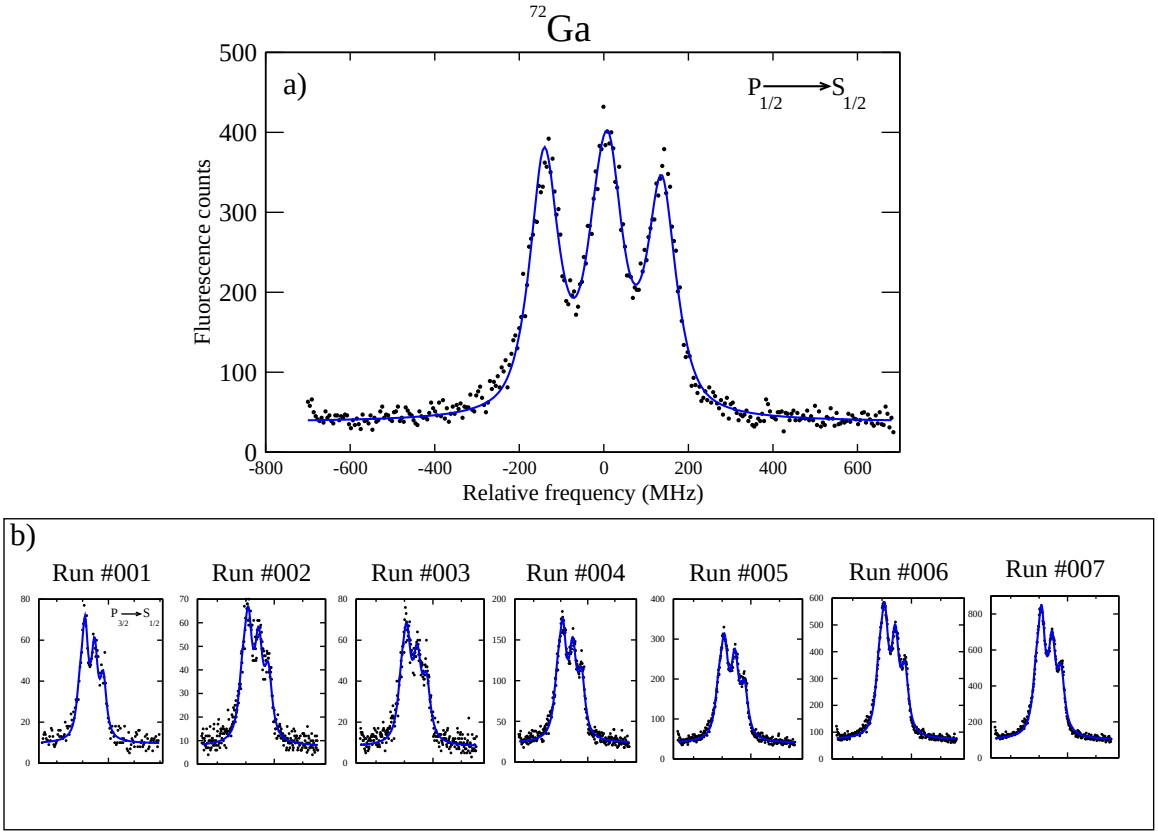

Figure 7.13: The hyperfine structure of $I = 3$ ground state for ^{72}Ga at the a) $P_{1/2} \rightarrow S_{1/2}$ and b) $P_{3/2} \rightarrow S_{1/2}$ transitions. The blue line indicates the fitted data. See text for details.

analysis approach. Finally, by constraining B $(P_{3/2})$ to the published value, a considerably worse fit is obtained. The new measurements on ^{72}Ga in May 2009 helped to solve this inconsistency. Section 7.4 is dedicated to the discussion of this issue.

The results of the combined analysis using run # 007 as the best spectrum for the $P_{3/2} \rightarrow S_{1/2}$ transition are shown in Table 7.9.

Table 7.8: Fitted values of $B\,(P_{3/2})$ for different runs of ^{72}Ga.

Run #	$B\,(P_{3/2})$ (MHz)
001	252 ± 20
002	248 ± 13
003	236 ± 11
004	241 ± 7
005	243 ± 27
006	239 ± 4
007	235 ± 4

Table 7.9: Table summarising the measured spin and hyperfine structure coupling constants of ^{72}Ga. All values are in MHz.

A	Source	I	$A\,(P_{1/2})$	$A\,(S_{1/2})$	$A\,(P_{3/2})$	$B\,(P_{3/2})$
^{72}Ga	This work	3	-43.7 ± 0.4	-35.5 ± 0.3	-6.35^{a}	235 ± 4
	Ref. [100]	3	-43.90076	–	-6.25698	193.67365
			± 0.00015		± 0.00011	± 0.0008

[a]This value was scaled using the ratio r_{417}

^{73}Ga

The hyperfine structure measurements of ^{73}Ga were performed on the $P_{1/2} \rightarrow S_{1/2}$ and $P_{3/2} \rightarrow S_{1/2}$ transitions. The results are shown in Figure 7.14. It is somewhat surprising that Figures 7.14.(a) and 7.14.(b) have relatively collapsed structures. If this isotope had $I = 3/2$, like ^{67,69,71}Ga, there would be 4 peaks in the $P_{1/2} \rightarrow S_{1/2}$ transition and 6 peaks in the $P_{3/2} \rightarrow S_{1/2}$, on the grounds of angular momentum coupling rules. However, assuming $I = 3/2$ in the fitting process led to $r_{417} = +5.09 \pm 0.21$ (compared to $+5.591 \pm 0.001$ in Equation 7.1) and large values for χ^2, which is a manifestation

Table 7.10: Table summarising the measured spin and hyperfine structure coupling constants of ^{73}Ga. All values are in MHz.

Isotope	Source	Spin	$A\ (P_{1/2})$	$A\ (S_{1/2})$	$A\ (P_{3/2})$
^{73}Ga	This work	$1/2$	412.8 ± 1.3	328.6 ± 1.2	60.1 ± 1.2
	Ref. [105]	$3/2$	–	–	–

of the incompatibility of this dataset with the $I = 3/2$ assumption. On the other hand, by assuming $I = 1/2$, three peaks result from the angular momentum coupling rules and selection rules for allowed transitions between hyperfine substates, and the ratio $A\ (S_{1/2})/A\ (P_{3/2}) = +5.48 \pm 0.11$, which is in good agreement with the value given in Equation 7.1. The conclusion that emerges from this analysis is that $I = 1/2$. As a consequence, $B\ (P_{3/2}) = 0$. All the hyperfine coupling constants were determined for the first time, as shown in Table 7.10.

^{74}Ga

The hyperfine structures of ^{74}Ga were measured in the $P_{1/2} \rightarrow S_{1/2}$ and $P_{3/2} \rightarrow S_{1/2}$ transitions. Apart from tentative spin assignments made on the basis of β decay studies [106, 107], a consensus around the ground-state spin for this isotope does not exist in the literature. During the fit, spin values ranging from $I = \{2,3,4,5,6,7\}$ were tested and judged on the basis of the quality of fits produced. However, the main difficulty associated with this assessment was the fact that the structures were collapsed in both transitions. In order to overcome this problem, the fitting routine allowed the hyperfine coupling coefficient $A\ (S_{1/2})$ to run as a free parameter, and $A\ (P_{1/2})$ and $A\ (P_{3/2})$ were scaled from $A\ (S_{1/2})$ according to the ratios given by Equations 7.2

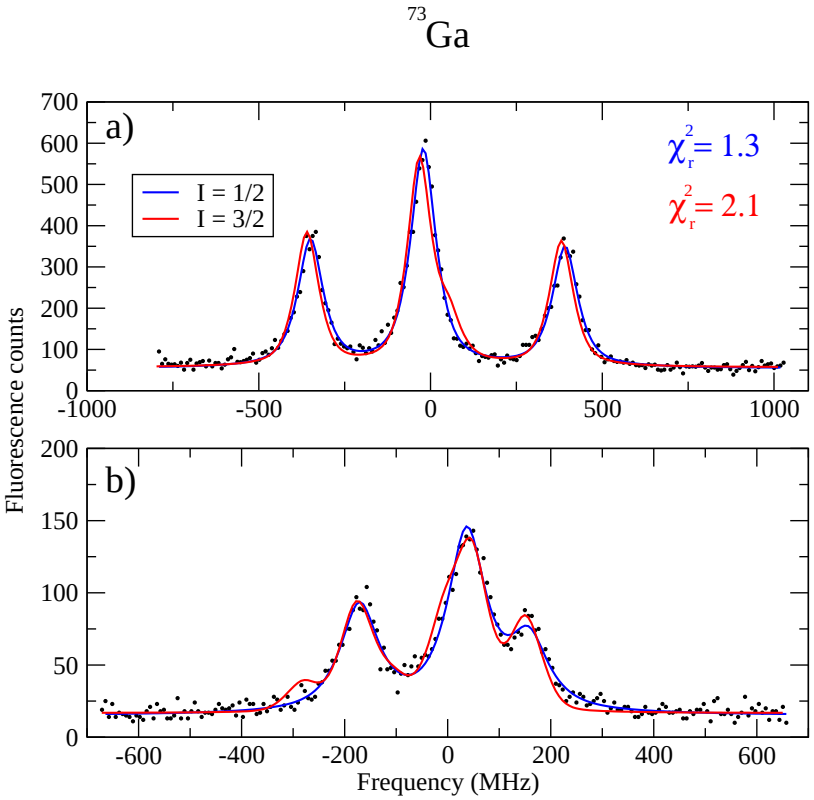

Figure 7.14: The hyperfine structures for ^{73}Ga at the a) $P_{1/2} \rightarrow S_{1/2}$ and b) $P_{3/2} \rightarrow S_{1/2}$ transitions. The blue line indicates the fitted data for $I = 1/2$, whereas the red line indicates the fit for $I = 3/2$. In both cases the fits were obtained from a simultaneous minimization of χ^2 for both spectra.

and 7.1. To prevent the fitting program from arbitrarily assigning zero values to some peaks, a lower bound on the peak intensities was imposed to be comparable with the background level. Figure 7.15 shows a variation of χ^2 for different possible ground-state spins. In order to discern between different spin assumptions, the confidence level $n\sigma$ was used, where n was calculated from [108]

$$n = \sqrt{\frac{\chi^2 - \chi^2_{min}}{\chi^2_{min}/Ndof}}. \tag{7.6}$$

In this case, $Ndof = 380$. The confidence level was computed from the standard error function $p(\%) = erf(n/\sqrt{2})$. From inspecting Figure 7.15, it becomes immediately clear that $I = 2$ can be discarded with a confidence level of 99.99%. However, it is hard to decide from spins 3 and 4 ($p \sim 57\%$ in favour of $I = 4$). It is clear that $I > 5$ can be discarded with a confidence greater than 98.5%. Figure 7.16 shows the spectra fitted for $I = 4$. However, since $I = 3$ cannot be completely ruled out, the hyperfine structure coupling constants will be given for these two spin candidates. Table 7.3 summarises the findings.

^{75}Ga

In this work, the hyperfine structure of ^{75}Ga was measured with the $P_{3/2} \rightarrow S_{1/2}$ transition only. Figure 7.17 shows the data and fitted spectra, for $I = 3/2$. The data was also fitted for $I = 5/2$; however, the fit gave a ratio $A\ (S_{1/2})/A\ (P_{3/2}) = 4.99 \pm 0.03$, which is many standard deviations away from the ratio given by Equation 7.1, and hence could be discarded. The main results obtained in this analysis are summarized

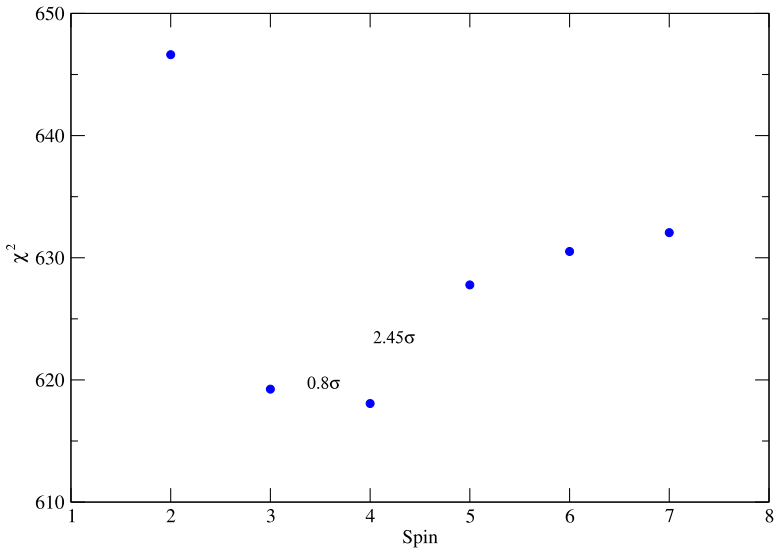

Figure 7.15: χ^2 as a function of possible spin assignment for ^{74}Ga. The numbers show the confidence levels relative to the minimum (I=4).

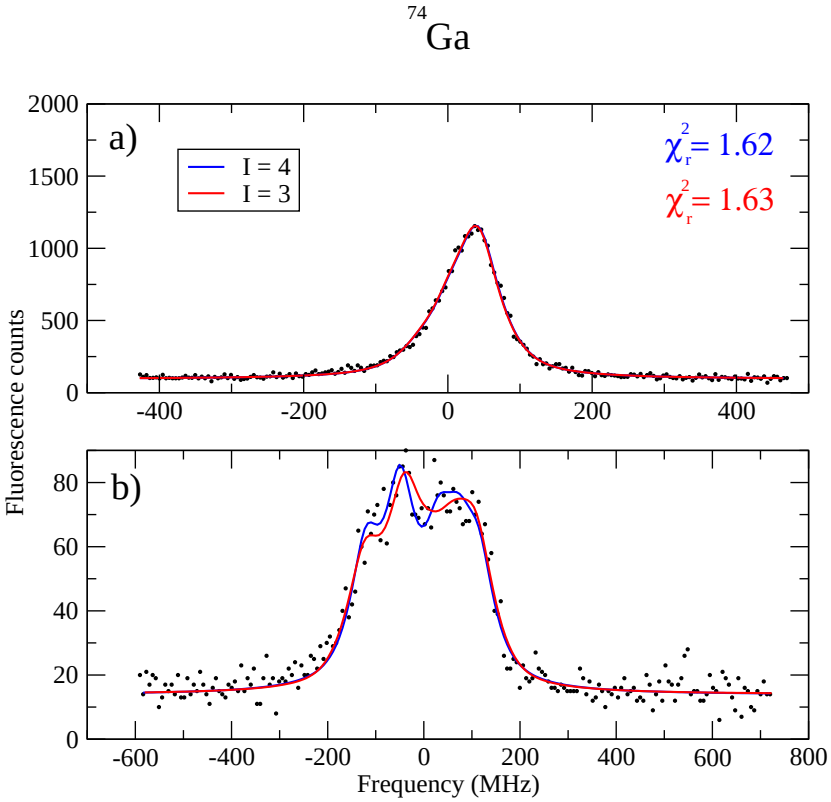

Figure 7.16: The hyperfine structures for ^{74}Ga at the a) $P_{1/2} \rightarrow S_{1/2}$ and b) $P_{3/2} \rightarrow S_{1/2}$ transitions. The blue line indicates the fitted data for $I = 4$, whereas the red line indicates the fit for $I = 3$. In both cases the fits were obtained from a simultaneous minimization of χ^2 for both spectra.

Table 7.11: Table summarising the measured spin and hyperfine structure coupling constants of ^{74}Ga. All values are in MHz. Using positive or negative values for the magnetic hyperfine coupling constants produce equally good fits.

A	Source	I	$A\ (P_{1/2})$	$A\ (S_{1/2})$	$A\ (P_{3/2})$	$B\ (P_{3/2})$
^{74}Ga	This work	3	12.9[a]	10.3 ± 0.4	1.85[a]	189.6 ± 8.6
	This work	4	10.3[a]	8.2 ± 0.3	1.47[a]	226.9 ± 7.3
	Ref. [106]	$(3,4)$	–	–	–	–
	Ref. [107]	$(4,5)$	–	–	–	–

[a]This value was scaled using the ratios r_{403} and r_{417}.

Table 7.12: Table summarising the measured spin and hyperfine structure coupling constants of ^{75}Ga. All values are in MHz.

A	Source	I	$A\ (P_{1/2})$	$A\ (S_{1/2})$	$A\ (P_{3/2})$	$B\ (P_{3/2})$
^{75}Ga	This work	$3/2$	–	973.5 ± 1.3	174.3 ± 0.6	-102.9 ± 1.8
	Ref. [109]	$(3/2)$	–	–	–	–
	Ref. [110]	$(1/2,3/2)$	–	–	–	–

on Table 7.12.

^{76}Ga

The analysis of the hyperfine structure for ^{76}Ga was based on data from the $P_{3/2} \rightarrow S_{1/2}$ transition. In order to determine the ground-state spin and the hyperfine coupling constants of this isotope, a procedure identical to the one performed on ^{75}Ga was conducted. Two spin candidates, $I = \{2,3\}$ were used in the fits. By checking the ratio of $A\ (S_{1/2})/A\ (P_{3/2})$ for both cases, it was possible to rule out the $I = 3$ possibility, since in this case the ratio was $r_{417} = +5.21 \pm 0.05$, whereas for $I = 2$, the ratio was

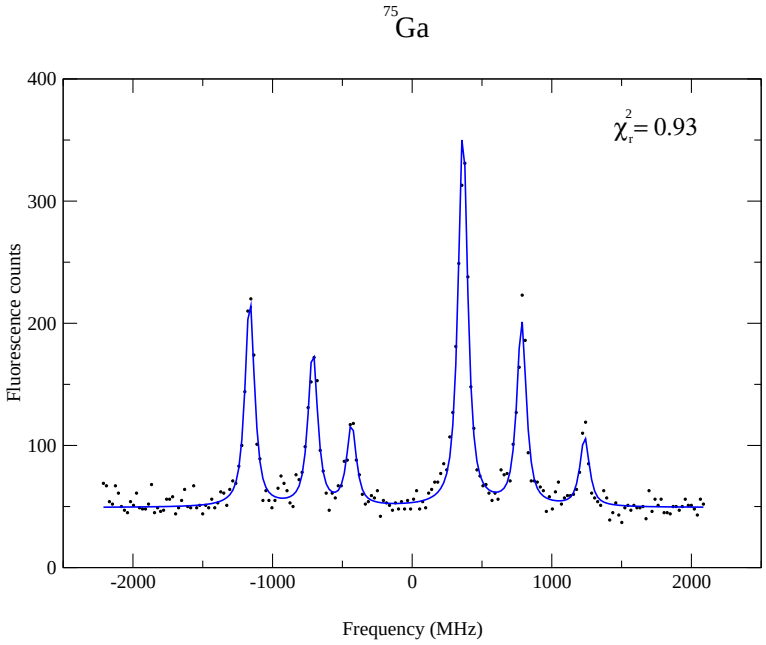

Figure 7.17: The hyperfine structure of $I = 3/2$ ground state for ^{75}Ga at the $P_{3/2} \rightarrow S_{1/2}$. The blue line indicates the fitted data.

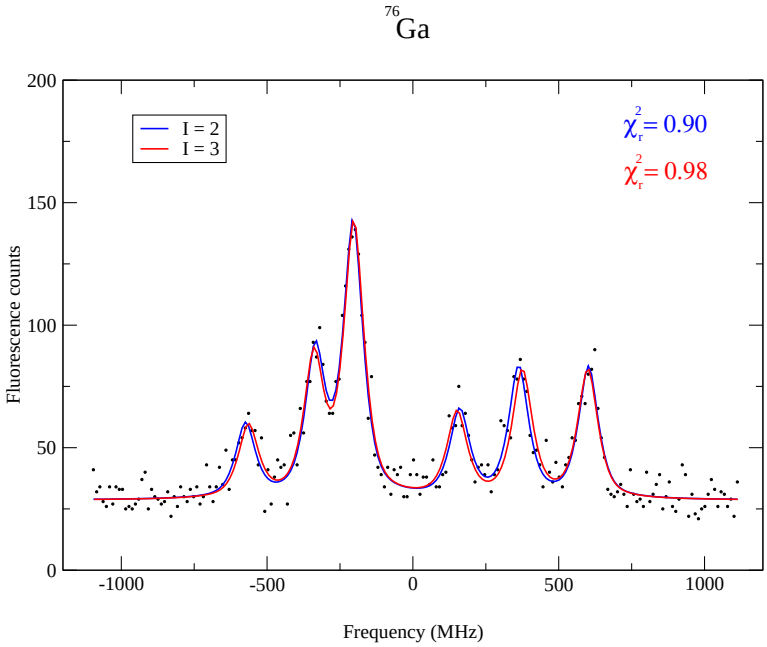

Figure 7.18: The hyperfine structure for ^{76}Ga at the $P_{3/2} \rightarrow S_{1/2}$ transition. The blue line indicates the fitted data for $I = 2$, whereas the red line indicates the fit for $I = 3$.

$r_{417} = +5.64 \pm 0.06$. In addition, on the basis of the χ^2 of both fits, a hypothesis test gives a confidence level better than 4σ in favour of $I = 2$. In summary, the spectra allowed a firm spin assignment as well as a determination of the hyperfine constants for ^{76}Ga. Table 7.13 shows the results.

^{77}Ga

The ^{77}Ga isotope was measured in both atomic transitions. Figure 7.19 shows the data and the fits for both spectra, for $I = 3/2$. The fits allowed the hyperfine constants for ^{77}Ga to be extracted. Table 7.14 summarises the results. Note that the ratio $A\ (S_{1/2})/A\ (P_{3/2}) = +5.58 \pm 0.02$, which is consistent with Equation 7.1. This result,

Table 7.13: Table summarising the measured spin and hyperfine structure coupling constants of ^{76}Ga. All values are in MHz.

A	Source	I	$A\ (P_{1/2})$	$A\ (S_{1/2})$	$A\ (P_{3/2})$	$B\ (P_{3/2})$
^{76}Ga	This work	2	–	-374.6 ± 1.5	-66.4 ± 0.6	117.2 ± 2.9
	Ref. [111]	(3)	–	–	–	–
	Ref. [112]	(2)	–	–	–	–

Table 7.14: Table summarising the measured spin and hyperfine structure coupling constants of ^{77}Ga. All values are in MHz.

A	Source	I	$A\ (P_{1/2})$	$A\ (S_{1/2})$	$A\ (P_{3/2})$	$B\ (P_{3/2})$
^{77}Ga	This work	3/2	1341.7 ± 2.2	1070.5 ± 1.5	191.7 ± 0.7	-77.1 ± 2.5
	Ref. [112]	(3/2)	–	–	–	–

in conjunction with the quality of the fits serve as reliable grounds to confirm $I = 3/2$.

^{78}Ga

The hyperfine structure of ^{78}Ga was measured in both transitions. The fitting code tested three spin candidates, $I = \{2,3,4\}$. By analysing the ratios of the hyperfine coupling constants $A\ (S_{1/2})/A\ (P_{3/2})$ for each case, as shown on Figure 7.20, it was possible to rule out the $I = \{3,4\}$ possibilities, and make an unequivocal assignment of $I = 2$ for the ground-state spin of ^{78}Ga. It is worth noting that the possibility of having $I = 1$ as the ground-state spin could easily be discarded since the number of peaks on the $P_{3/2} \rightarrow S_{1/2}$ transition would have to be 5, and not 6, as observed. The spectra shown in Figure 7.21 shows the fitted data for both transitions. It becomes evident that $I = 2$. Table 7.15 summarizes the results.

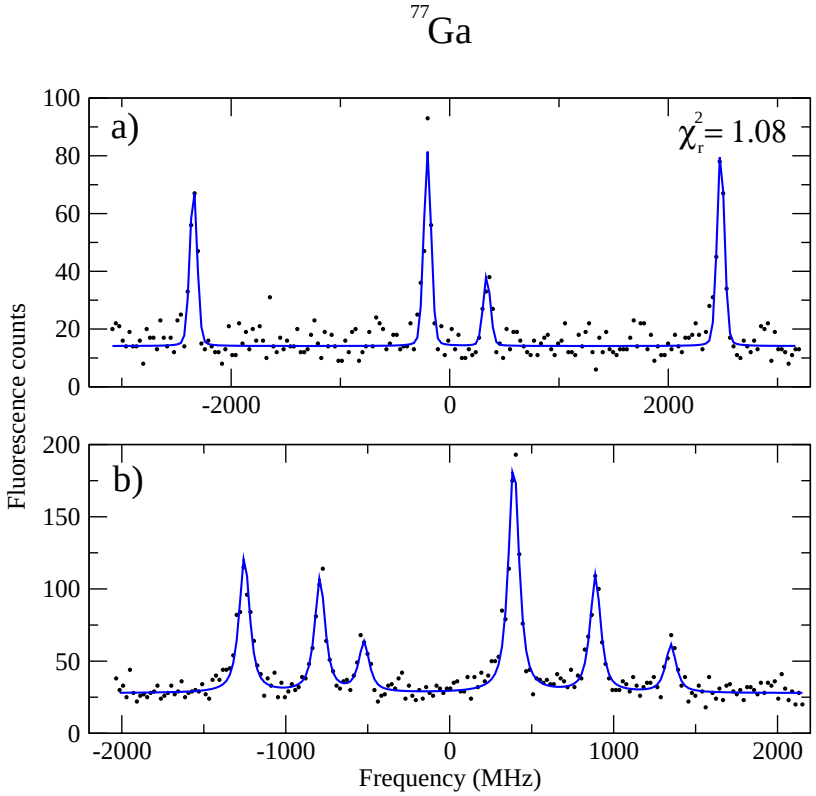

Figure 7.19: The hyperfine structure of $I = 3/2$ ground state for ^{77}Ga at the a) $P_{1/2} \rightarrow S_{1/2}$ and b) $P_{3/2} \rightarrow S_{1/2}$ transitions. The blue line indicates the fitted data, which was obtained from a simultaneous minimization of χ^2 for both spectra.

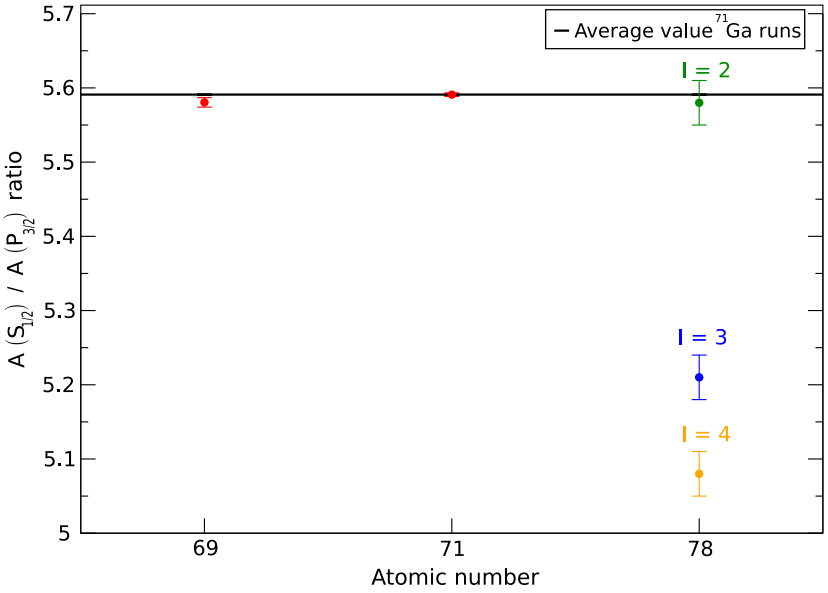

Figure 7.20: The r_{417}-values for ^{78}Ga against different spin assignments, compared to some systematics of stable ^{69,71}Ga.

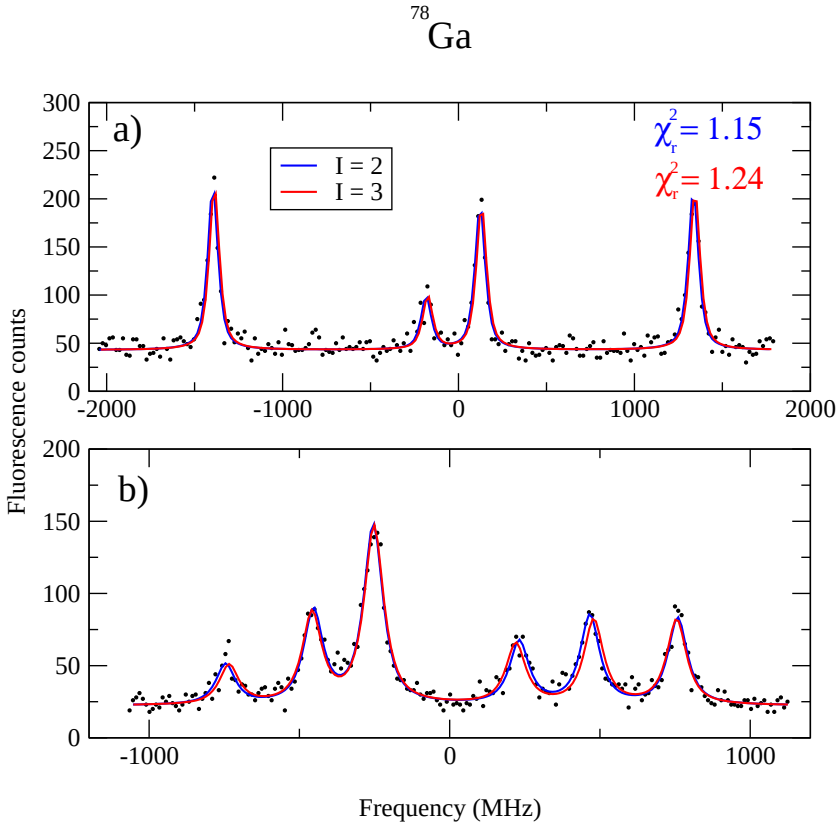

Figure 7.21: The hyperfine structure of $I = \{2,3\}$ possibilities for ^{78}Ga at the a) $P_{1/2} \rightarrow S_{1/2}$ and b) $P_{3/2} \rightarrow S_{1/2}$ transitions.

Table 7.15: Table summarising the measured spin and hyperfine structure coupling constants of ^{78}Ga. All values are in MHz.

A	Source	I	$A\,(P_{1/2})$	$A\,(S_{1/2})$	$A\,(P_{3/2})$	$B\,(P_{3/2})$
^{78}Ga	This work	2	-607.6 ± 0.9	-484.9 ± 0.8	-86.9 ± 0.5	119.7 ± 2.4
	Ref. [113, 114]	(3)	–	–	–	–

^{79}Ga

The hyperfine structure of ^{79}Ga was measured in both transitions. Two possible candidates for the ground-state spin are $I = \{3/2, 5/2\}$. Figure 7.22 shows the fits for both cases. Based on the χ^2 comparisons, it is not possible to determine the spin. The ratios $A\,(S_{1/2})/A\,(P_{3/2})$ are $+5.55 \pm 0.07$ and $+5.65 \pm 0.09$ for $I = 3/2$ and $I = 5/2$, respectively. Thus, this method cannot distinguish between the spins either.

In order to gain further information which could help in deciding on the ground-state spin candidates for ^{79}Ga, an investigation into the behaviour of the relative intensities of the peaks was undertaken. Although these intensities deviate from the predictions of Equation 2.18, the empirical values obtained from the dataset were exploited. Figure 7.23 shows each hyperfine peak of the odd-Ga isotopes measured in the $P_{1/2} \rightarrow S_{1/2}$ and $P_{3/2} \rightarrow S_{1/2}$ transitions. The average value of those intensities was calculated only using the calibration runs of ^{71}Ga, which are indicated with blue circles. In the Figure, the position of the points for the hyperfine peaks of ^{67,75,77,79}Ga isotopes are related to the measurements performed between the calibration runs. In the case of ^{79}Ga, the values for the intensities were obtained based on a fitting assuming $I = 3/2$. This can be justified by the fact that fitting ^{79}Ga with $I = 5/2$ did not

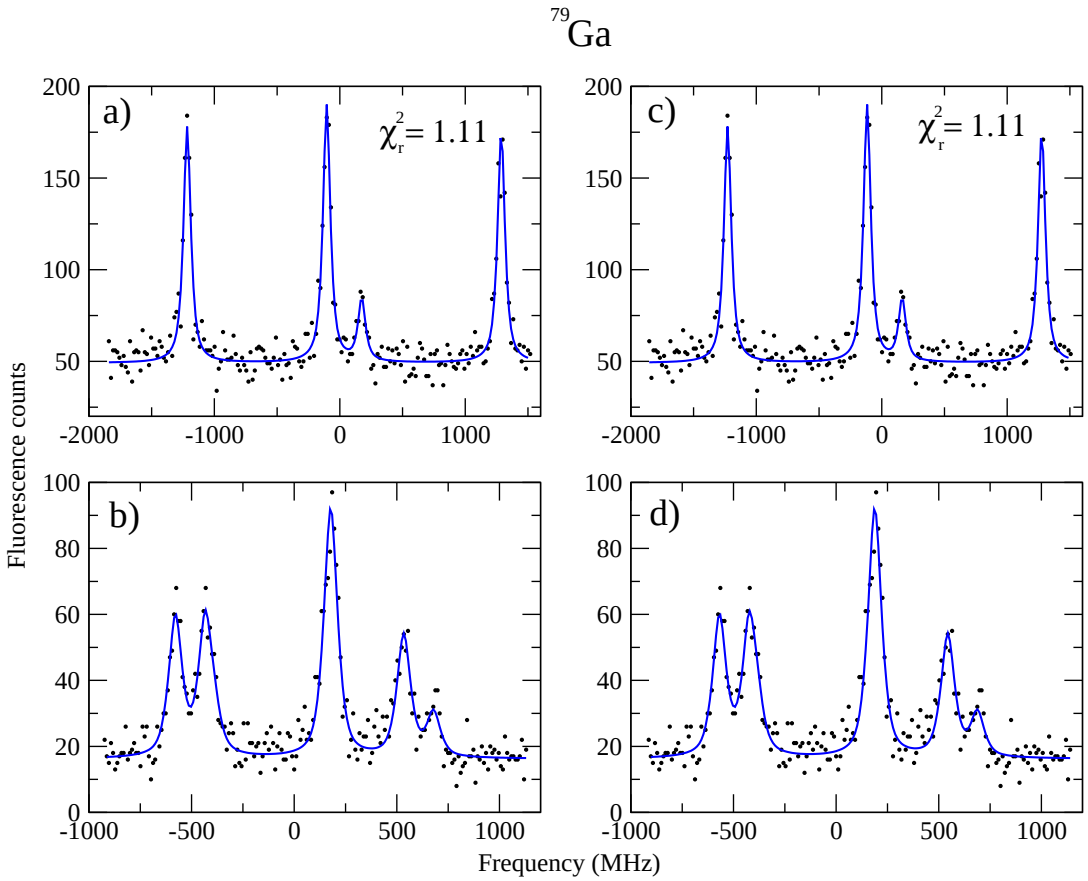

Figure 7.22: The hyperfine structure of ^{79}Ga at the a) $P_{1/2} \rightarrow S_{1/2}$ and b) $P_{3/2} \rightarrow S_{1/2}$ transitions, assuming $I = 3/2$. The spectra c) and d) show the same spectra, assuming $I = 5/2$. The blue line indicates the simultaneously fitted data.

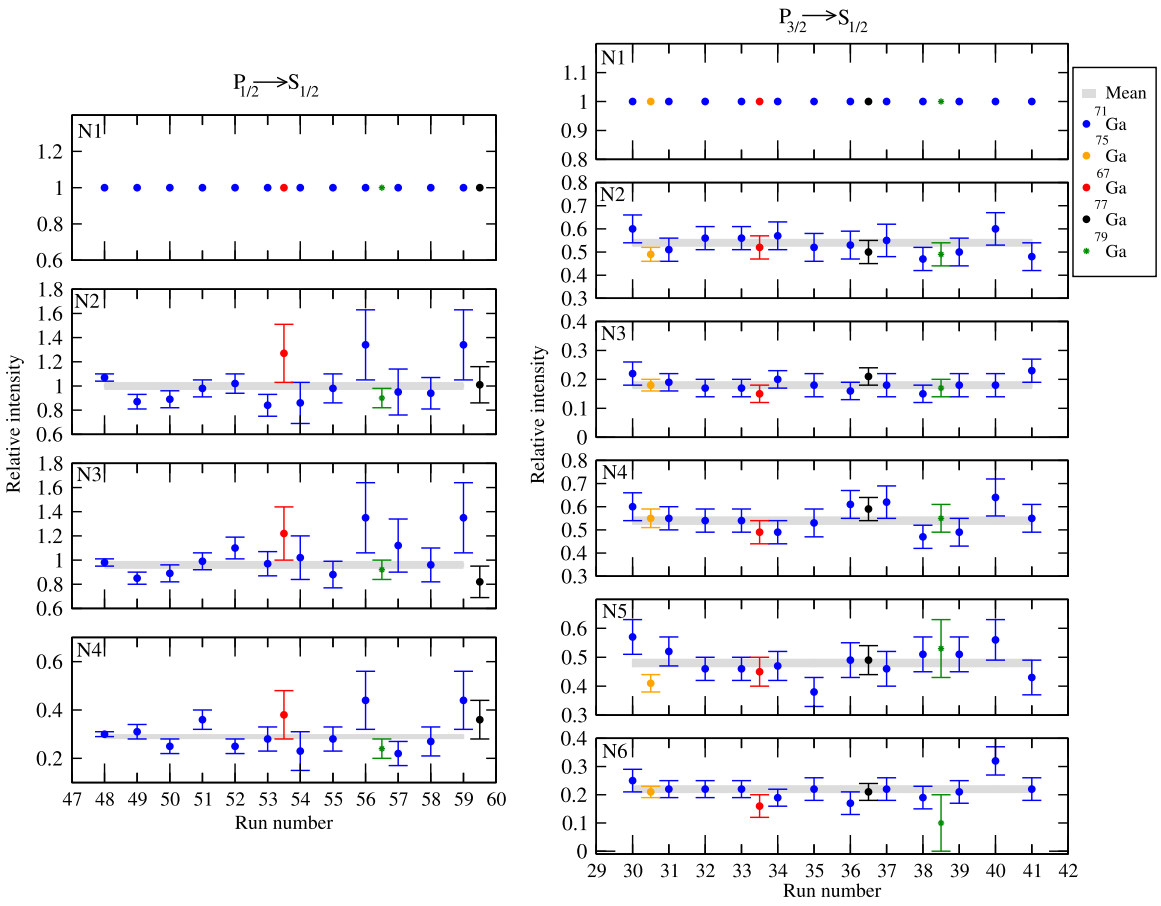

Figure 7.23: Relative intensities of all $I = 3/2$ odd-Ga isotopes in the $P_{1/2} \rightarrow S_{1/2}$ (left) and $P_{3/2} \rightarrow S_{1/2}$ (right) transitions, normalised to $N1$. The grey lines indicate the error weighted averages. The thickness of the lines indicate the error of the average. See text for details.

Table 7.16: Relative intensities for the $P_{1/2} \rightarrow S_{1/2}$ transition of ^{71,79}Ga. normalised to N_1. $N_1 : F = 2 \rightarrow F' = 2$; $N_2 : F = 2 \rightarrow F' = 1$; $N_3 : F = 1 \rightarrow F' = 2$; $N_4 : F = 1 \rightarrow F' = 1$. Add one to F and F' if $I = 5/2$ is considered.

Peak	Racah ($I = 3/2$)	Racah ($I = 5/2$)	^{71}Ga ($I = 3/2$)[a]	^{79}Ga ($I = 3/2, 5/2$)[b]
N_1	1	0.8	1	1.11 ± 0.09
N_2	1	1	1.00 ± 0.02	1
N_3	1	1	0.96 ± 0.02	1.02 ± 0.06
N_4	0.2	0.28	0.29 ± 0.01	0.27 ± 0.04

[a] Averaged values.
[b] In this case N_2 was chosen for the normalisation.

change the relative intensities significantly. In the case of the $P_{1/2} \rightarrow S_{1/2}$ transition, run #59 was the last calibration performed on ^{71}Ga. When looking at the $P_{3/2} \rightarrow S_{1/2}$ transition data, it is noteworthy the striking consistency within these intensities and the calibration runs, which show that the relative intensities remained constant for the duration of the experiment.

Tables 7.16 and 7.17 provide the average relative intensities for the hyperfine peaks in the $P_{1/2} \rightarrow S_{1/2}$ and $P_{3/2} \rightarrow S_{1/2}$ transitions, respectively. The Tables also show the theoretical predictions based on Racah intensities assuming $I = 3/2$ and $I = 5/2$. Table 7.16 is quite revealing in several ways. First, it is clear that for the $P_{1/2} \rightarrow S_{1/2}$ transition in ^{71}Ga, N_4 has an experimental value 50% greater than what would be expected from Racah intensities. This trend is consistent with what was observed in the case of ^{79}Ga, assuming $I = 3/2$. On the other hand, looking at the Racah predictions in the case of $I = 5/2$ for N_1 in the $P_{1/2} \rightarrow S_{1/2}$ transition, the experimental value should have been reduced by 25%, which was not the case, and yet the experimental value for

Table 7.17: Relative intensities for the $P_{3/2} \rightarrow S_{1/2}$ transition of ^{71,79}Ga. $N_1 : F = 3 \rightarrow F' = 2$; $N_2 : F = 2 \rightarrow F' = 2$; $N_3 : F = 1 \rightarrow F' = 2$; $N_4 : F = 2 \rightarrow F' = 1$; $N_5 : F = 1 \rightarrow F' = 1$; $N_6 : F = 0 \rightarrow F' = 1$. Add one to F and F' if $I = 5/2$ is considered. The '/'on N_5 and N_6 indicates that the fitting programme produced different outputs for the intensities when fitting the dataset using $I = \{3/2, 5/2\}$ as candidates.

Peak	Racah ($I = 3/2$)	Racah ($I = 5/2$)	^{71}Ga ($I = 3/2$)[a]	^{79}Ga ($I = 3/2, 5/2$)
N_1	1	1	1	1
N_2	0.35	0.43	0.54 ± 0.01	0.49 ± 0.05
N_3	0.07	0.12	0.18 ± 0.01	0.17 ± 0.03
N_4	0.35	0.34	0.54 ± 0.01	0.55 ± 0.06
N_5	0.35	0.43	0.48 ± 0.01	$0.53 \pm 0.01 / 0.49 \pm 0.13$
N_6	0.14	0.33	0.22 ± 0.01	$0.1 \pm 0.1 / 0.13 \pm 0.13$

[a] Averaged values.

Table 7.18: Table summarising the measured spin and hyperfine structure coupling constants of ^{79}Ga. All values are in MHz.

A	Source	I	$A\ (P_{1/2})$	$A\ (S_{1/2})$	$A\ (P_{3/2})$	$B\ (P_{3/2})$
^{79}Ga	This work	$3/2$	695.8 ± 1.5	556.1 ± 1.2	100.1 ± 1.2	55.3 ± 4.2
	Ref. [115]	$(3/2)$	–	–	–	–

N_1 for ^{79}Ga is consistent with the experimental value of ^{71}Ga. The findings suggest that $I = 3/2$ is the ground state-spin. This result and the hyperfine coupling constants of ^{79}Ga are shown on Table 7.18.

7.4 A second experiment

In May 2009, beam time was allocated in order to complete the IS457 initial proposal. During this experiment, $0.1 - 2.0$ mW laser was available, and the typical

power was used ($0.3 - 0.4$ mW). The laser beam was expanded to a larger waist ($\sim$ 3 mm). Therefore, a lower power density laser beam was delivered to the light collection region. In addition, this arrangement has increased the overlap with the ion beam. From this work, it was possible to re-measure the hyperfine structures of ^{69,71,72,73,74,75,76,77,78,79}Ga in the $P_{3/2} \rightarrow S_{1/2}$ transition. The data is still under analysis and the preliminary results obtained are in agreement with the findings discussed in this thesis. In addition, the hyperfine structures of ^{80,81,82}Ga were measured for the first time. Relevant for the completion of this thesis was the investigation of the discrepancy between the B hyperfine coupling constant in ^{72}Ga obtained from the previous IS457 campaign and the result from the 1960's. In addition, the ambiguity around the ground-state spin assignment for ^{79}Ga necessitated further investigation.

^{72}Ga revisited

In Section 7.3 an important issue was raised, which concerned a discrepancy in the value of the B hyperfine coupling constant for ^{72}Ga between measurements performed in the first round of IS457 experiments, and previously measured values. The experiment was repeated, with different laser intensities. Figures 7.24.(a) and 7.24.(b) show the data for 0.1 mW and 0.3 mW, respectively. The fits for these datasets were performed as before, with B $(P_{3/2})$ left as a free parameter, and the magnetic the hyperfine coupling constants A $(S_{1/2})$ and A $(P_{3/2})$ fixed to the literature values. The FWHM of the resonances were found to be narrower, 60 ± 2 MHz, for the case of lower laser power than in the case of 0.2 mW, which was 68 ± 1 MHz. The B factor for 0.2 mW

was found to be $+239 \pm 5$ MHz, whereas for 0.1 mW, $B\ (P_{3/2}) = +197 \pm 6$ MHz, a value which is now in agreement with the literature value.

The result of this study demonstrates that a variation in the laser intensity can account for a shift in the centroid positions of the resonances in the case of an overlapping hyperfine structure. This problems is also considered later when optical pumping effects were modelled.

^{79}Ga revisited

Figure 7.25 shows the hyperfine structure of ^{71,79,81}Ga measured with the same laser power (0.35 mW). The blue spectra shown in the Figures 7.25(b) and 7.25(c) correspond to fits of ^{79}Ga and ^{81}Ga, with the ground-state spin assumed to be $I = 3/2$ and $I = 5/2$, respectively. Table 7.19 also shows the ratios between the hyperfine coefficients $A\ (S_{1/2})/A\ (P_{3/2})$ obtained from fits for different spin possibilities. It follows that assigning $I = 3/2$ to ^{79}Ga and $I = 5/2$ to ^{81}Ga is consistent with the ratio of the magnetic hyperfine coupling constants for ^{71}Ga, of which the spin is known. The change in the distribution of the peak intensities relative to the reference isotope $\left(^{71}\text{Ga, I} = 3/2\right)$ is shown on Table 7.20. Here is further strong evidence to establish the ground-state spin of ^{79}Ga as $I = 3/2$.

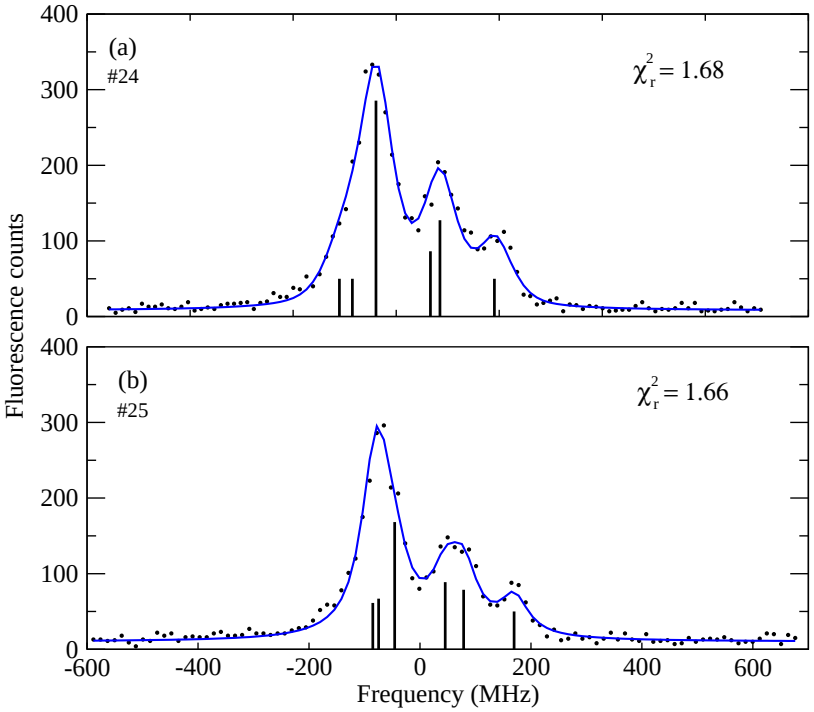

Figure 7.24: The hyperfine structures of ^{72}Ga for 0.2 mW in (a), and 0.1 mW in (b). The blue line indicates the fitted data. The black lines are to mark the positions of the hyperfine peaks. The magnetic hyperfine constants were fixed, whereas $B\ (P_{3/2})$ was left as free parameter. The 6 component intensities were also left as free fitting parameters.

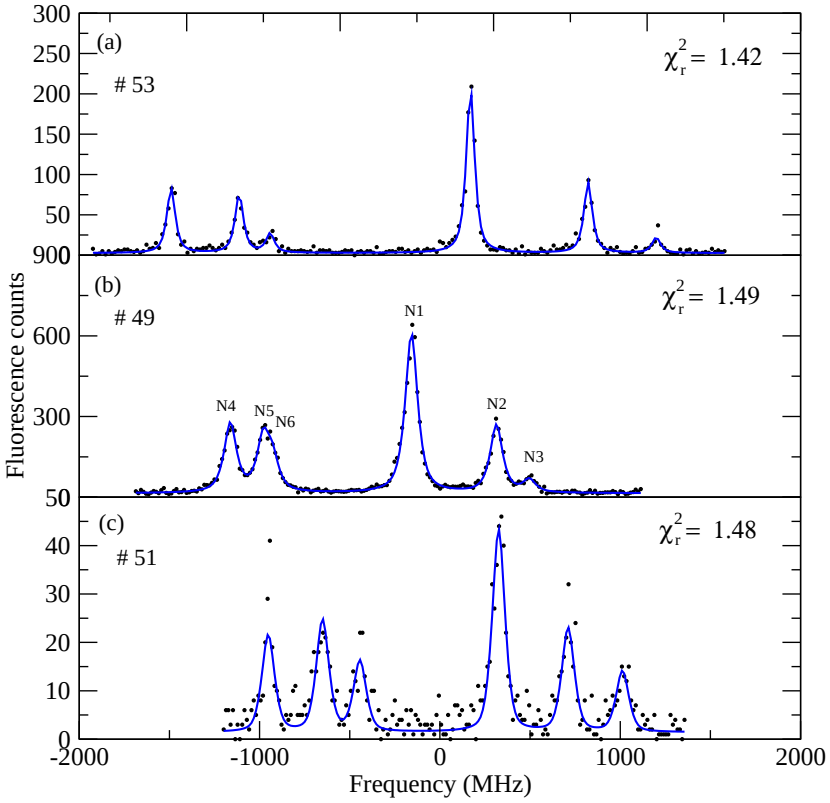

Figure 7.25: The hyperfine structures of ^{71}Ga in (a), ^{79}Ga in (b) and ^{81}Ga in (c) at the $P_{3/2} \rightarrow S_{1/2}$ transition. The blue line indicates the fitted data. See text for details.

Table 7.19: The ratio between the hyperfine coupling constants $A\ S_{1/2}$ and $A\ P_{3/2}$, for different spin assignments. The absolute values were obtained from fitting the dataset of the recent IS457 campaign of May 2009. The reference ratio based on 2008 data is $+5.591(1)$.

A	I	$A\ (S_{1/2})/A\ (P_{3/2})$
79	**3/2**	$\mathbf{+5.64 \pm 0.02}$
	5/2	$+5.73 \pm 0.02$
81	3/2	$+5.96 \pm 0.04$
	5/2	$\mathbf{+5.62 \pm 0.04}$

Table 7.20: Relative intensities for the $P_{3/2} \rightarrow S_{1/2}$ transition of ^{71,79,81}Ga, normalised to N_1. $N_1 : F = 3 \rightarrow F' = 2$; $N_2 : F = 2 \rightarrow F' = 2$; $N_3 : F = 1 \rightarrow F' = 2$; $N_4 : F = 2 \rightarrow F' = 1$; $N_5 : F = 1 \rightarrow F' = 1$; $N_6 : F = 0 \rightarrow F' = 1$. Add one to F and F' if $I = 5/2$ is considered.

Peak	Racah ($I = 3/2$)	Racah ($I = 5/2$)	^{71}Ga	^{79}Ga	^{81}Ga
N_1	1	1	1	1	1
N_2	0.35	0.43	0.43 ± 0.03	0.42 ± 0.01	0.51 ± 0.06
N_3	0.07	0.12	0.09 ± 0.01	0.07 ± 0.01	0.30 ± 0.04
N_4	0.35	0.34	0.39 ± 0.03	0.43 ± 0.01	0.47 ± 0.06
N_5	0.35	0.43	0.35 ± 0.03	0.32 ± 0.03	0.55 ± 0.06
N_6	0.14	0.33	0.11 ± 0.01	0.18 ± 0.03	0.34 ± 0.05

7.5 Optical pumping simulation

In order to understand the changes in the relative intensities of the hyperfine transitions observed during the gallium experiments, and the change of the resonance centroids in ^{72}Ga with laser power, an optical pumping model was developed by the author of this thesis. The model is an extension of the original work of Yordanov [116], and is based on the semiclassical approach and weak-field approximation [42]. The main change made in the original formalism was the addition of hyperfine "leak" states, corresponding to decay from the $S_{1/2}$ level into the $P_{1/2}$ energy level, when exciting the $P_{3/2} \rightarrow S_{1/2}$ transition. Following the notation of Yordanov, the time evolution of the electronic population occupancies of each m_F substate is given by the rate equations

$$\begin{aligned} \dot{N}_i &= -N_i \sum_{j=0}^{g-1} (A_{ij} + D_{ij}) + \sum_{j=0}^{g-1} N_j D_{ij}, \qquad 0 \leq i \leq g' - 1 \\ \dot{N}_i &= \sum_{j=0}^{g-1} N_j (A_{ji} + D_{ji}) - N_i \sum_{j=0}^{g-1} D_{ji}, \qquad g' - 1 \leq i \leq g - 1, \end{aligned} \tag{7.7}$$

where $g' = (2I+1)(2J+1)$ is the degeneracy of the upper state and g is the total degeneracy, which also includes the leak state. A_{ij} is the Einstein spontaneous emission coefficient of either the resonant transition or of the leak state, which can be readily obtained from the lifetime of the atomic transitions multiplied by $3-j$ and $6-j$ symbols [117], and is shown by Equation 7.8. For the $S_{1/2} \rightarrow P_{3/2}$ decay, $\tau = 9.72$ ns and for the $S_{1/2} \rightarrow P_{1/2}$ decay, $\tau = 20.3$ ns.

$$A_{ij} = \frac{(2F_i+1)(2F_j+1)(2J_i+1)}{\tau} \begin{Bmatrix} J_j & F_j & I \\ F_i & J_i & 1 \end{Bmatrix}^2 \begin{pmatrix} F_j & 1 & F_i \\ -m_{F_j} & \Delta m_F & m'_{F_i} \end{pmatrix}^2 \tag{7.8}$$

The $D_{ij}(D_{ji})$ matrix elements are related to the Einstein $B_{ij}(B_{ji})$ stimulated emission/absorption coefficients[1] times the radiation spectral density $\rho(\nu)$. The latter quantities are directly related to the optical absorption cross section (see Equation 3.3) and the laser intensity (W/m^2), as shown by Equation 7.9.

$$D_{ij} = B_{ij}\rho(\nu) = \frac{\sigma(\nu)I}{h\nu} \tag{7.9}$$

The saturation intensity for the $P_{3/2} \rightarrow S_{1/2}$ transition is $I_{sat} \sim 250$ W/m^2 [103]. The laser was linearly polarised, which implies $\Delta m_F = 0$ for the absorption of radiation. The decay is unrestricted with respect to the polarisation of the emitted photons, therefore $\Delta m_F = \pm 1,\ 0$. The final fluorescence decay rate R is given by

$$R = \sum_{\substack{0 \leq i \leq g' \\ g' < j < g-1}} N_i A_{ij} \tag{7.10}$$

The system of coupled first-order differential equations 7.7 was integrated numerically using the fourth-order Runge-Kutta method with fixed step size. The routine was written in C, with some features of C++, and executed in the ROOT framework. The integration was performed in two steps. First, the atoms interact with the laser from the point they are formed in the charge-exchange cell (see Figure 4.4) until the sample reaches the detection setup and passes in front of the light interaction region. In terms

[1] The Einstein A and B coefficients are related by : $A_{ij} = \frac{8\pi h\nu^3}{c^3} B_{ij}$

Table 7.21: The change in the FWHM of the resonances for different laser intensities.

I (W/m^2)	FWHM (MHz)
30	35.360 ± 0.003
60	37.979 ± 0.002
120	44.237 ± 0.002

of distance, this corresponds to $\sim$ 35 cm. If ^{71}Ga ions are accelerated by 30 kV, then the time-of-flight corresponds to 1.22 μs. The second integration occurs for the sample passing in front of the photomultiplier tube, which is equivalent to an extra integration time of approximately 200 ns. During this time, the total decay rate is computed cumulatively. The model also incorporates the effect of a residual Doppler broadening caused by 1 eV energy spread of the ion beam, by numerically convoluting atoms with different velocity classes. Figure 7.26 shows the simulated spectra of ^{71}Ga for different laser intensities. The simulated spectra were fitted with the same programme used to analyse the real data. From the fits, the widths of the resonances were obtained, and tabulated on Table 7.21.

It is important to mention that for the lowest intensity used in the simulation (30 W/m^2), the model gives a FWHM = 26 MHz, if the residual Doppler broadening is neglected. This is indeed close to the transition natural line. Experimentally, the narrowest linewidth observed was 48.9 ± 2.3 MHz for 0.11 mW laser beam passing through a $\sim$ 3 mm collimating aperture, which would correspond to a power density of $\sim$ 20 W/m^2.

It is also instructive to investigate the change in the absolute values of the transition

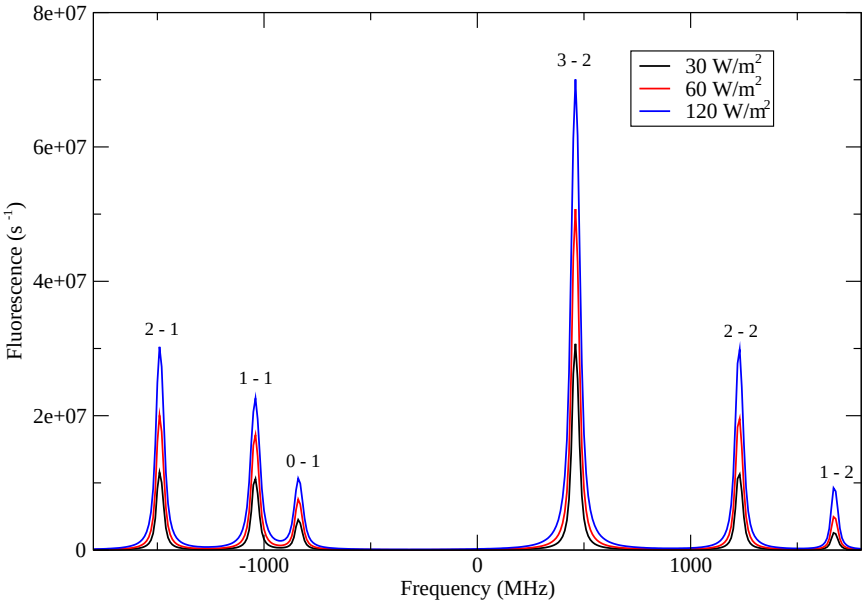

Figure 7.26: Simulation of the hyperfine structure for ^{71}Ga on the for the $P_{3/2} \rightarrow S_{1/2}$ transition, for different intensities.

Table 7.22: The simulated relative intensities of ^{71}Ga($I = 3/2$) for different laser intensities. The errors on the relative intensities are small ($\sim 10^{-5}$).

Peak	Racah	30 W/m^2	60 W/m^2	120 W/m^2
N_1	1	1	1	1
N_2	0.35	0.367	0.376	0.394
N_3	0.07	0.078	0.086	0.099
N_4	0.35	0.368	0.379	0.397
N_5	0.35	0.351	0.345	0.335
N_6	0.14	0.143	0.144	0.146

strengths, as well as the relative intensities. These are directly related to how the electronic populations of the hyperfine levels evolve as a function of pumping time and laser intensity. As an illustrative example, Figure 7.27 shows the results for the changes in populations for strongest transition, $F = 3 \rightarrow F' = 2$.

Relative intensities

The optical pumping model offered some insights in understanding the observed changes in the relative intensities. For the simulated spectra shown in Figure 7.26, the relative intensities obtained from the χ^2 minimization are tabulated on Table 7.22. Qualitatively, the simulation is in good agreement with the results shown on Table 7.20 for ^{71}Ga. Another outstanding feature that arises from this exercise is that the commensurate increase on the relative intensity of N_3 with the power density is correctly reproduced by the modelling.

The optical pumping model was also used to investigate the hyperfine structure of ^{72}Ga. The simulation was performed for different intensities in a similar way to

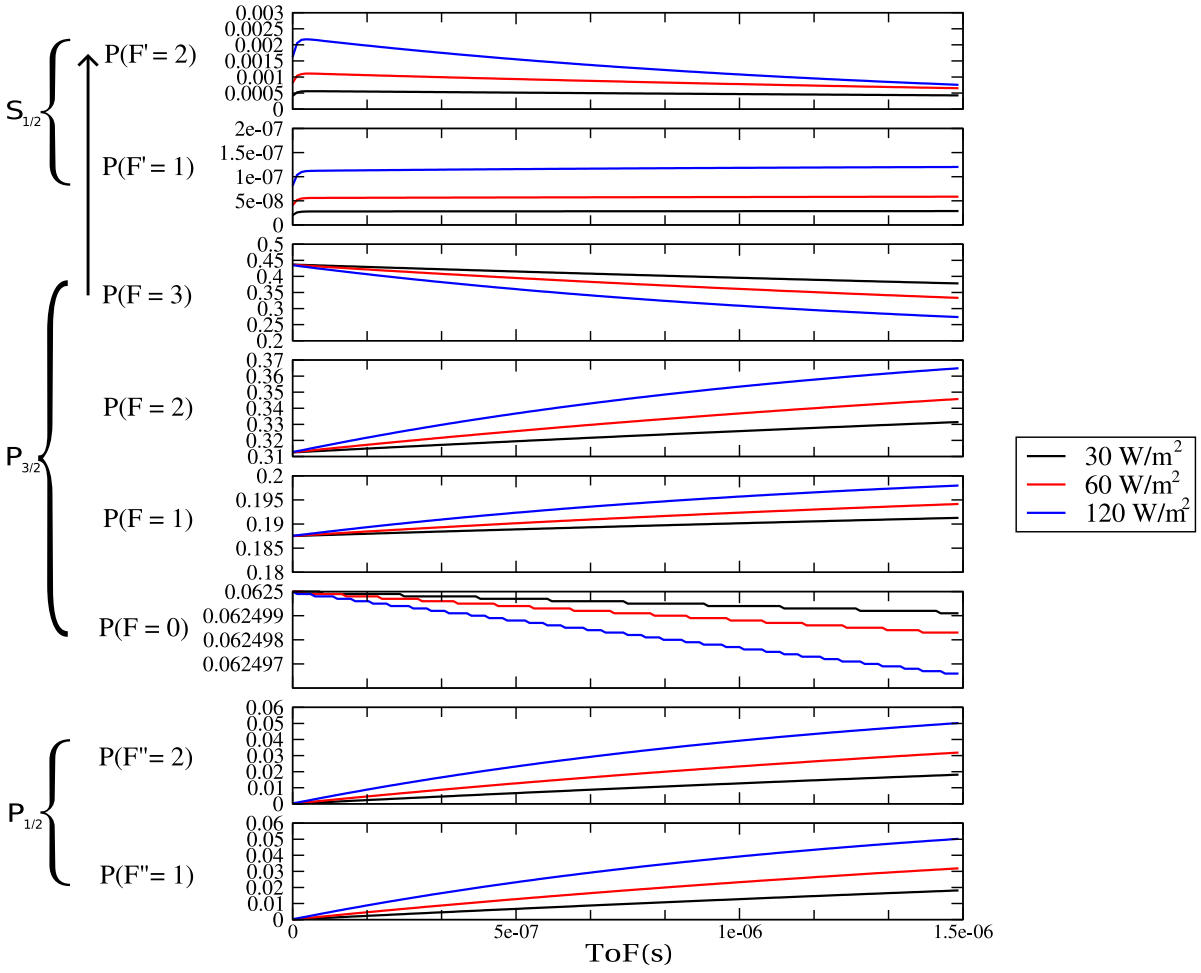

Figure 7.27: Simulation of the time evolution of the normalised population occupancies of the hyperfine levels for ^{71}Ga, with the atoms of a given velocity class on resonance with the linearly polarised laser tuned on the $N_1 : F = 3 \rightarrow F' = 2$ transition, for different intensities.

^{71}Ga. However, the simulation fails to reproduce the shift on the transition centroids for an increase on the laser intensity. The reason for the disagreement between the model and experimental data is not yet understood. Furthermore, the model cannot explain the relative intensities of the data taken on the first round of measurements. It is believed that the experiment was performed with intensities beyond saturation, since higher laser intensities were then used (more power and tighter focus were applied). In addition, a poor ion-optics setting in the first experiment could be the cause of a non-uniform atom-laser overlap, so that different groups of atoms would start interacting with the laser at different points in space. Therefore, in a more realistic model, a careful convolution of the time distribution of the optical pumping would have to be taken into account. On the basis of this study it is recommended that in the case of overlapping hyperfine structures with the same atomic structure such as gallium, care must be taken with the laser power used. If a reference isotope exists with a well-resolved hyperfine structure, it would be desirable to make a measurement with the lowest possible laser power in order to recover Racah relative intensities.

7.6 Summary

The analysis of the dataset obtained in the first round of experiments of the IS457 campaign allowed most of the spins and the hyperfine coupling constants to be unambiguously determined. For the scans performed on both transitions, the simultaneous fitting approach was rather beneficial for the determination of the hyperfine coupling constants. The second experimental campaign helped to clarify some pending issues

Table 7.23: Table summarising the measured hyperfine structure coupling constants of Ga isotopes. No brackets after the values indicate the parameter has been constrained in the fitting process.

A	I	$A\,(P_{1/2})$ (MHz)	$A\,(S_{1/2})$ (MHz)	$A\,(P_{3/2})$ (MHz)	$B\,(P_{3/2})$ (MHz)
67	$3/2$	$+1225.8 \pm 2.3$	$+980.3 \pm 1.6$	$+176.3 \pm 1.1$	$+73 \pm 3.3$
68	1	$+11.6$	$+9.3$	$+1.7$	$+10.8$
69	$3/2$		$+1070.9 \pm 0.5$	$+191.9 \pm 0.2$	$+61.7 \pm 0.7$
70	1	$+562.5 \pm 0.6$	$+448.5 \pm 0.6$	$+76.9 \pm 2.8$	$+28.9 \pm 9)$
71	$3/2$	$+1701.7 \pm 0.2$	$+1358.04 \pm 0.19$	$+242.9 \pm 0.1$	$+39.05 \pm 0.33$
72	3	-43.7 ± 0.4	-35.5 ± 0.3	-6.35	$+197 \pm 6$
73	$1/2$	$+412.8 \pm 1.3$	$+328.6 \pm 1.2$	$+60.1 \pm 1.2$	$-$
74	(3)	$+12.9$	$+10.3 \pm 0.4$	$+1.85$	$+189.6 \pm 8.6$
	(4)	$+10.3$	$+8.2 \pm 0.3$	$+1.47$	$+226.9 \pm 7.3$
75	$3/2$		$+973.5 \pm 1.3$	$+174.3 \pm 0.6$	-102.9 ± 1.8
76	2		-374.6 ± 1.5	-66.4 ± 0.6	$+117.2 \pm 2.9$
77	$3/2$	$+1341.7 \pm 2.2$	$+1070.5 \pm 1.5$	$+191.7 \pm 0.7$	-77.1 ± 2.5
78	2	-607.6 ± 0.9	-484.9 ± 0.8	-86.9 ± 0.5	$+119.7 \pm 2.4$
79	$3/2$	$+695.8 \pm 1.5$	$+556.1 \pm 1.2$	$+100.1 \pm 1.2$	$+55.3 \pm 4.2$

related to ^{72,79}Ga. The optical pumping model was helpful in order to clarify the origin of the changes in the observed relative intensities. Table 7.23 summarises the results. From the hyperfine constants obtained, the nuclear moments can be promptly extracted. The next chapter will discuss these results in more detail.

CHAPTER 8

DISCUSSION

8.1 Ground-state spins and nuclear moments

From each hyperfine coupling constant obtained from the fits of the data presented in the previous chapter, the corresponding moments were derived using Equations 2.19 and 2.20, and using ^{71}Ga as reference. For the determination of the magnetic dipole moment, a weighted average was performed between $\mu(P_{1/2})$, $\mu(S_{1/2})$ and $\mu(P_{3/2})$, except when the ratios between the magnetic hyperfine coupling constants were fixed. Tables 8.1 and 8.2 summarise the results.

8.2 The odd-A nuclei

Magnetic dipole moments

The magnetic dipole moment, μ_I, which first appeared in Equation 2.10 is now formally defined as the expectation value of the $\mathbf{T}^1(n)$ operator in a state with maximum M_I projection, $\mid IM_I = I\rangle$

$$\mu_I \equiv \langle II \mid \mathbf{T}^1(n) \mid II\rangle, \tag{8.1}$$

Table 8.1: Table summarising the measured moments of the odd-*A* Ga isotopes. No sign next to the numbers indicate that the sign of the moment was unknown. Previously published data taken from [18].

		Previous work			This work	
A	I^{π}	μ(nm)	Q_s(b)	I	μ(nm)	Q_s(b)
67	$3/2^-$	$+1.8507$	0.195	$3/2$	$+1.8483$	$+0.1981$
		± 0.0003	± 0.005		± 0.0022	± 0.0091
69	$3/2^-$	$+2.01659$	$+0.17$	$3/2$	$+2.0211$	$+0.1675$
		± 0.00005	± 0.03		± 0.0009	± 0.0024
71	$3/2^-$	$+2.56227$	$+0.106$	$3/2$	$-$	$-$
		± 0.00002	± 0.003			
73	$3/2^-$	$-$	$-$	$1/2$	$+0.207$	0
					± 0.005	
75	$3/2^-$	$-$	$-$	$3/2$	$+1.8370$	-0.2793
					± 0.0023	± 0.0055
77	$3/2^-$	$-$	$-$	$3/2$	$+2.0201$	-0.209
					± 0.0021	± 0.007
79	$(3/2^-)$	$-$	$-$	$3/2$	$+1.0485$	$+0.15$
					± 0.0016	± 0.01

where the operator $\mathbf{T}^1(n)$ has contributions from the orbital ($\mathbf{L}$) and spin ($\mathbf{S}$) terms which comes from the currents of the individual nucleons[1] [12]:

$$\mathbf{T}^1(n) = \mu_N \sum_n (g_{ln}\mathbf{L}_{z,n} + g_{sn}\mathbf{S}_{z,n}). \tag{8.2}$$

The constant $\mu_N = \frac{e\hbar}{2m_p}$ is the nuclear magneton, where m_p is the proton mass. The terms g_l and g_s are the orbital and spin gyromagnetic ratios, or *g-factors*. For a free proton $g_l = +1$ and $g_s = +5.585694713 \pm 0.000000046$, whereas for a neutron $g_l = 0$

[1] This operator omits meson exchange currents. For a detailed discussion, see [118], pg. 18.

Table 8.2: Table summarising the measured moments of even-*A* Ga isotopes. No sign next to the numbers indicate that the sign of the moment was unknown. Previously published data taken from [18].

		Previous work			This work	
A	I^{π}	μ(nm)	Q_s(b)	I	μ(nm)	Q_s(b)
68	1^+	0.01175	0.0277	1	–	–
		±0.00005	±0.0014			
70	1^+	–	–	1	+0.5644	+0.078
					±0.0004	±0.024
72	3^-	−0.13224	+0.52	3	−0.13396	+0.53
		±0.00002	±0.01		±0.00005	±0.01
74	$(3,4)^-$	–	–	(3)	+0.03138	+0.51
					±0.00011	±0.02
				(4)	+0.03303	+0.61
					±0.00012	±0.02
76	$(2,3)^+$	–	–	2	−0.941	+0.3181
					±0.0034	±0.0083
78	(3^+)	–	–	2	−1.22	+0.325
					±0.01	±0.007

and $g_s = -3.82608545 \pm 0.0000009$, [119]. For a nucleus in a state with angular momentum I, $\mu_I = g_I I \mu_N$, where g_I is the nuclear g-factor. In terms of a single nucleon the operator $\boldsymbol{\mu}$ is given by

$$\boldsymbol{\mu} = \mathbf{T}^1(n) = \mu_N(g_l \mathbf{j}_z + g_s \mathbf{s}_z)/\hbar \tag{8.3}$$

For $\mathbf{j} = \mathbf{l} + \mathbf{s}$, it can be shown [12] (p. 154) that

$$\langle \boldsymbol{\mu} \rangle = \begin{cases} [j g_l + (g_s - g_l)/2]\,\mu_N, & \text{for j= l+ 1/2,} \\ [j g_l - (g_s - g_l)/2 \times j/(j+1)]\,\mu_N, & \text{for j= l - 1/2.} \end{cases} \tag{8.4}$$

The values obtained from Equation 8.4 are the *Schmidt estimates* for the magnetic-moments in a single particle picture. However, this is a rather simplified picture which only works in a small number of cases. In fact the nuclear currents produced by other nucleons should also be taken into account and therefore effective g-factors need to be used. Typically $g_s^{eff} = 0.6 \times g_s^{free}$ [12]. Using a renormalised $g_s^{eff} = +3.34$ for the proton, the measurements of the ground-state spins of ^{67,69,71,75,77,79}Ga can somewhat be accommodated in the framework of the nuclear shell model, in which the three valence protons occupy the single-particle π $p_{3/2}$ orbital. Figure 8.1 shows the magnetic dipole moments of the neighbours of odd-A gallium isotopes, whose ground-state spins are $I = 3/2$.

The experimental values of the magnetic moments of gallium fall slightly below the values of its odd-A copper neighbours, except for $N = 44$, when the moment of gallium becomes higher than for copper, and $N = 42$ when the gallium ground-state spin is not $3/2$. A comparison between odd-A copper and gallium isotopes reveals an increase in the magnetic moments, approaching the Schmidt line for $N = 40$. This is expected, because as the neutrons completely fill the fp shell (at $N = 40$), there is no first-order core polarization contribution from the neutrons (the spin-orbit partners ν $p_{1/2}$,$p_{3/2}$ and ν $f_{5/2}$,$f_{7/2}$ are filled, therefore $1p-1h$ excitations are blocked) and the pure π $p_{3/2}$ configuration should dominate.

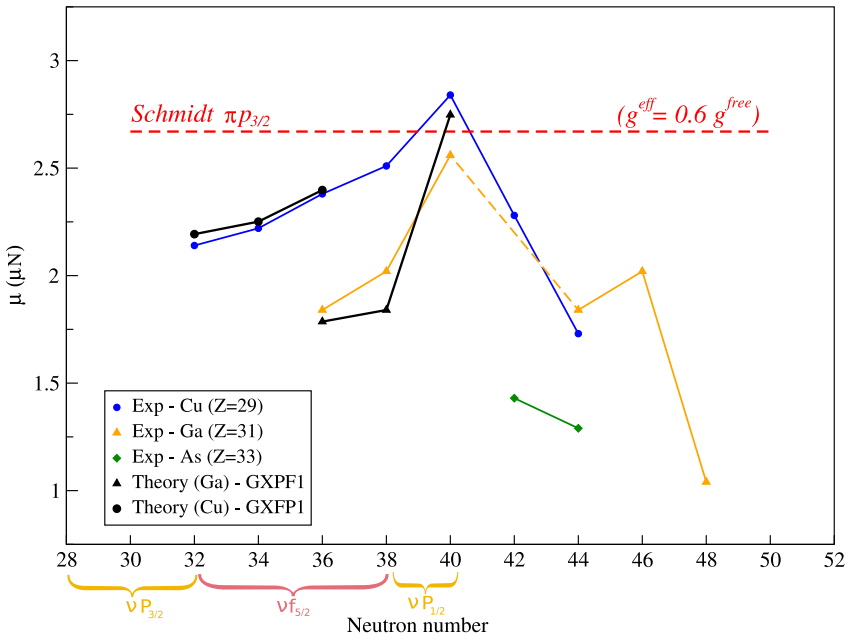

Figure 8.1: The magnetic dipole moments in the vicinity of odd-A gallium isotopes. Only the isotopes with $I = 3/2$ are included. The error bars are small compared to the symbol size. The moments for copper and arsenic are taken from [18, 120]. The theoretical shell model values using the GXPF1 interaction were taken from [121]. The value of the magnetic moment of ^{73}Cu ($N = 44$) is an unpublished value of recent collinear laser studies performed with ISCOOL [22].

Electric quadrupole moments

The spectroscopic electric quadrupole moment, Q_s, which appeared in Equation 2.13 is a measure of how much the nuclear charges deviate from a spherical distribution. It is defined in terms of the expectation value of the $\mathbf{T}^2(n)$ operator in a state with maximum M_I projection, $\mid IM_I = I\rangle$

$$Q_s \equiv \langle II \mid \mathbf{T}^2(n) \mid II\rangle, \tag{8.5}$$

where the operator $\mathbf{T}^2(n) = \rho_N(\mathbf{r}_N) r_N^2 Y_2^0(\theta,\phi)$, with ρ_N the nuclear charge density. For a point particle, the quadrupole moment becomes [12]

$$Q_s = \mp \frac{(2I-1)}{(2I+2)} \frac{\tilde{e}}{e} \langle r^2 \rangle, \tag{8.6}$$

where $\tilde{e}$ is an effective charge, which results from truncations in the model space and from the introduction of effective operators and $\langle r^2 \rangle$ is the nuclear mean square charge radius. The negative sign occurs for a particle orbiting outside a closed shell. The positive sign corresponds to a hole. The first possibility gives an oblate deformation, whereas the second one leads to a prolate deformation. The result from Equation 8.6 has been used as an estimate of the quadrupole moment, using the radial dimension of a single particle (hole) in a three-dimensional harmonic oscillator potential (see reference [122], pg. 209), with $N = 3$. The effective charge was taken to be $\tilde{e} \approx e$. From this estimate $Q_s = 0.11$ b. With this simple shell model assumption, the sign of the Q_s is explained for $N \leq 40$ from a proton hole configuration, since $(\pi\ p_{3/2})^3 \equiv$

$(\pi\, p_{3/2})^{-1}$. It is also instructive to consider whether the gallium isotopes are deformed. In this case, the nucleus is considered to have an intrinsic quadrupole moment Q_0. The spectroscopic quadrupole moment is then the projection of Q_0 along the quantization axis. Both quantities are related by [19]

$$Q_s = \frac{3I^2 - I(I+1)}{(I+1)(2I+3)} Q_0. \tag{8.7}$$

The intrinsic quadrupole moment does not depend on the nuclear spin and is often parametrized as a function of a *deformation parameter* β [19]

$$Q_0 = \frac{3ZR_{av}^2}{\sqrt{5\pi}} \beta(1+0.36\beta), \tag{8.8}$$

where Z is the number of protons and $R_{av} = 1.2\, A^{1/3}$ fm. For well-deformed nuclei, $\beta = 0.2 - 0.3$ [11]. Using as an estimate for gallium ($I = 3/2$, $A \approx 70$ and $\beta = 0.1$) gives $Q_s = 0.12$ b, which is comparable to the single particle estimate for the $\pi\ p_{3/2}$ proton. Using $\beta = 0.2$ gives $Q_s = 0.24$ b. This suggests that the gallium isotopes are indeed near spherical, and therefore it encourages shell model calculations to be performed in this region. Figure 8.2 shows the evolution of the measured quadrupole moments of odd-A gallium isotopes, in addition to the theoretical calculations using GXPF1 interaction [121].

The figure shows a drop in deformation as the $N = 40$ subshell is filled, which gives a single-particle character to the configuration. This complements the conclusion drawn from the analysis of the magnetic moments. Again, the theory correctly reproduces the observations up to $N = 40$.

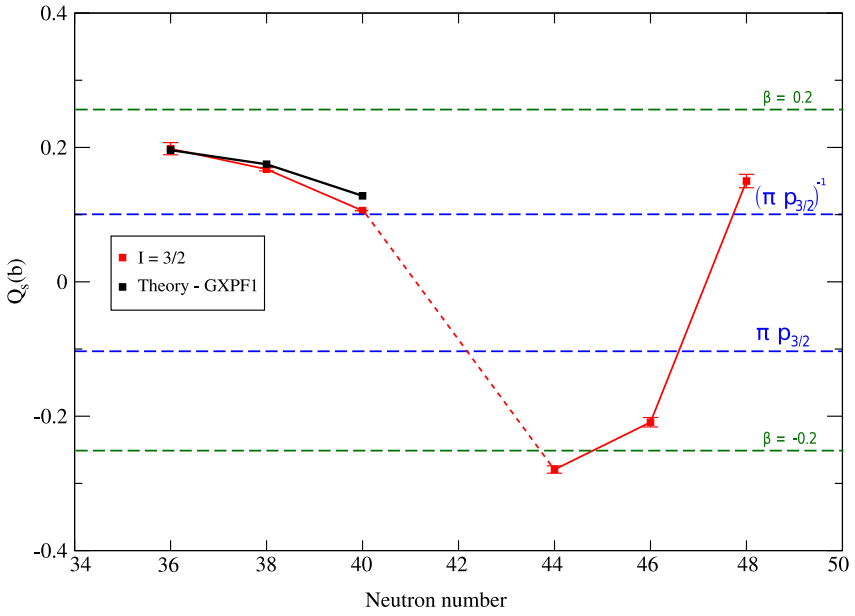

Figure 8.2: The electric quadrupole moment of odd-A gallium isotopes. The blue lines are the single particle estimates for a harmonic oscillator potential. The green lines are estimates for a nuclear deformation $|\beta| = 0.2$. The GXPF1 theoretical values were taken from [121].

The present study of the odd-A gallium isotopes produced results which corroborate the recent findings of Stefanescu and collaborators [123], which were based on the analysis of high-spin data detected with the GAMMASPHERE array. The authors have identified a $g_{9/2}$ proton band and observed a systematic lowering of $17/2$, $13/2$, $9/2$ levels as the sub-shell is filled at $N = 40$. For ^{73}Ga, however, the authors were unable to make an unequivocal ground-state spin assignment, despite observations of a severe depression of the high spin states. Theoretically, a recent work by Yoshinaga, Higashiyama and Regan showed that by including the fp shell and the $g_{9/2}$ orbital in shell model calculations designed to understand the high-spin data on ^{75,77,79}Ga, they could correctly reproduce the trend which shows an $I = 1/2$ level decreasing in energy as N approaches 42 [124], as shown by Figure 8.3. The authors also managed to correctly assign the ground-state spin of ^{79}Ga.

8.3 The even-A nuclei

In the case of the odd-odd nuclei, the nuclear g-factor, and hence the magnetic dipole moment can be tentatively estimated from the coupling of a proton occupying an orbital with angular momentum $\pi\, J_1$ and a neutron occupying an orbital $\nu\, J_2$, with g-factors, g_1 and g_2. In this picture the possible total angular momenta for a nucleus follow the triangular relation and can assume values from $|\, I-J\,| \ldots I+J$. To illustrate this point, a simple vector model is shown by Figure 8.4. For $\mathbf{J} = \mathbf{J_1} + \mathbf{J_2}$ and $\boldsymbol{\mu} = g\mathbf{J}$ in units of μ_N, it follows that

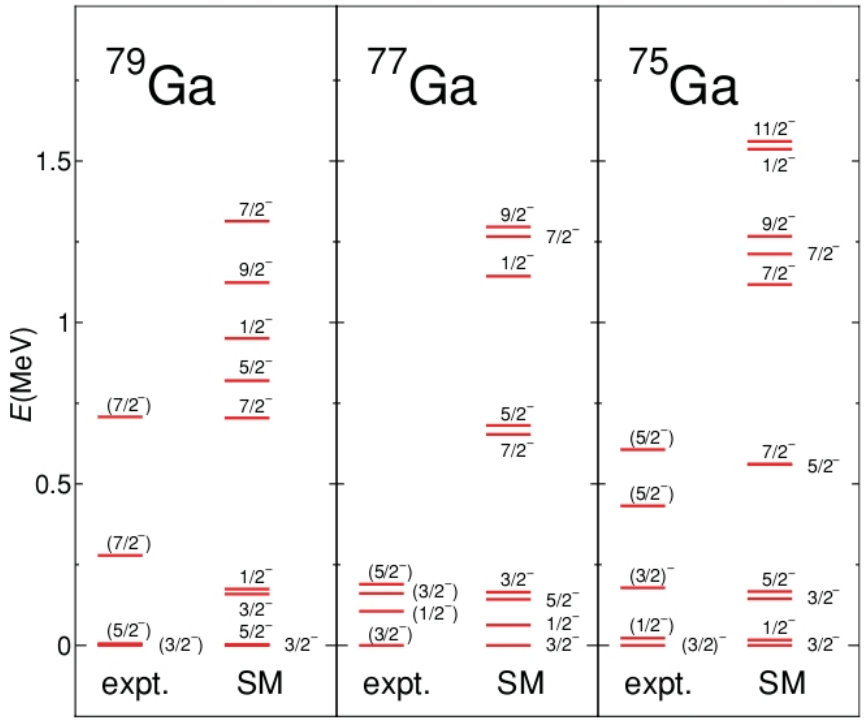

Figure 8.3: Results of recent shell model calculations compared to high-spin data on neutron rich gallium isotopes. Taken from [124].

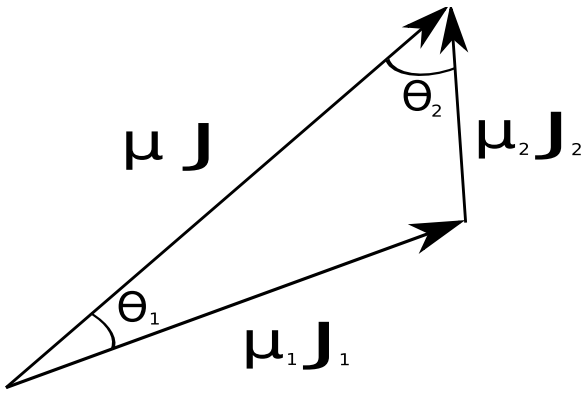

Figure 8.4: The coupling of two nucleons with angular momentum J_1 and J_2 to a state with angular momentum J.

$$
\begin{aligned}
g &= \frac{|\,\mu\,|}{|\,J\,|} \\
&= \frac{|\,\mu_1\,|\cos\theta_1 + |\,\mu_2\,|\cos\theta_2}{|\,J\,|} \\
&= g_1\,|\,J_1\,|\,\frac{\mathbf{J}\cdot\mathbf{J_1}}{|\,J\,|^2|\,J_1\,|} + g_2\,|\,J_2\,|\,\frac{\mathbf{J}\cdot\mathbf{J_2}}{|\,J\,|^2|\,J_2\,|} \\
&= \frac{g_1+g_2}{2} + \frac{g_1-g_2}{2}\left[\frac{J_1(J_1+1)-J_2(J_2+1)}{J(J+1)}\right]
\end{aligned}
\tag{8.9}
$$

The equation derived in 8.9 is the *Landé formula* [125]. Likewise, the quadrupole moments can be estimated from additivity rules using an expression involving $3-j$ and $6-j$ symbols, which can be found in reference [12], for example. The resultant nuclear spin J will depend on the relative orientation of the individual spins and in some cases it can be predicted using Nordheim's empirical rules [126]:

$$J = |\,J_1 - J_2\,|, \quad \text{if } L_1+J_1+L_2+J_2 \text{ is even,} \tag{8.10}$$

$$|\,J_1 - J_2\,| < J \leq J_1 + J_2, \quad \text{if } L_1+J_1+L_2+J_2 \text{ is odd.} \tag{8.11}$$

The measured values of the moments for odd-odd gallium isotopes are more difficult to reconcile with a simple single-particle picture, because there is more than a single particle (hole) occupying the proton and neutron orbitals, and therefore the occupancy of each nucleon could be such that $j_i \neq J_i$. In this case, the use of recoupling rules for the total angular momentum such as the seniority scheme is necessary [125]. Notwithstanding, using Nordheim's rule 1 (Equation 8.10) the spins and parities of ^{68,70}Ga are consistent with $\pi\ p_{3/2} \otimes \nu\ f_{5/2}$ and $\pi\ p_{3/2} \otimes \nu\ p_{1/2}$ configurations. However, the moments of these isotopes cannot be explained by Equation 8.9. For instance,

in the case of ^{70}Ga ($I = 1^+$), if the protons were arranged as in $^{71}_{31}Ga_{40}$ ($I = 3/2^-$, $\mu = +2.56\ \mu_N$) and the neutrons as in $^{71}_{32}Ge_{39}$($I = 1/2^-$, $\mu = +0.54\ \mu_N$), the resultant moment from the Landé formula would be $+2.32\ \mu_N$, which compares poorly with the measured value ($+0.56\ \mu_N$).

For the case of ^{72}Ga, its ground-state spin has negative parity. It is this isotope that marks the onset of deformation. This should be understood by the fact that the $\nu\ g_{9/2}$ orbital is starting to fill. The ground state spin of this isotope is in agreement with the revised empirical rule ($R3$) of Brennan and Bernstein [127], which states that $J = J_1 + J_2 - 2$, for $\pi\ p_{3/2} \otimes \nu\ (g^3_{9/2})_{7/2}$. However, the magnetic moments are not in such good agreement ($\mu_{exp} = -0.13396 \pm 0.00005\ \mu_N$, $\mu_{\rm emp} = -0.47\ \mu_N$).

The data obtained from the laser measurements of ^{74}Ga permits ambiguities in the ground-state spin assignment between $I = \{3,4\}$. The problem in fitting the data is compounded by the possible presence of a 9.5 s 0^+ isomer in the spectra. However, fitting the spectra for either spin configurations led to the conclusion that the quadrupole moment was large and positive. Turning to other experimental evidence, it is possible to constrain the value of $I_{g.s.}$. The observation on the β decay of ^{74}Ga to ^{74}Ge with the subsequent γ de-excitations of the daughter made by Ythier and collaborators [106] in 1959 led them to suggest that the ground-state spin of ^{74}Ga could be $2 \leq I \leq 5$. Later, Eichler *et al.* in 1962 suggested that $I = 4^-$ or $I = 5^-$ would be good candidates. In their work, the authors argued that this assignment would be consistent with the absence of strong beta decays to the first and second 2^+ states in ^{74}Ge. Camp, Fielder and Foster [111] in 1971, this time using high purity germanium

detectors, which improved the resolution of the observed γ rays also suggested the possibility of $I = \{3^-, 4^-\}$. Finally, the last decay study involving ^{74}Ga was performed by van Klinken and Taff in 1974 [128]. In this work, the authors compared their experimental results to calculations performed by Schwartz on jj coupling including an unrestrained number of protons and neutrons in the orbitals [129]. The authors could then build a theoretical level ordering based on a residual proton-neutron interaction, which led them to suggested more assertively that $I = 4^-$ was the ground state for a neutron configuration of $\nu\ (g^3_{9/2})_{9/2}$ or $\nu\ (g^3_{9/2})_{7/2}$, or a mixture of both. In the present work, the simultaneous fitting procedure on both atomic spectra described in the previous chapter, indicates that the $I = \{2, 5\}$ possibilities could be ruled out. With the accumulated body of experimental data presented it is therefore plausible that ^{74}Ga has a $I = 4$ ground-state spin assignment.

As for ^{76,78}Ga, the ground-state spins had only been tentatively assigned based on decay studies. The observation on the β decay of ^{76}Ga to ^{76}Ge made by Camp and Foster [130] led them to suggest that the ground-state spin of ^{76}Ga could be $I = 3^-$. However, in observing the decay of ^{76}Zn to ^{76}Ga, Ekström and collaborators [112] suggested that the ground-state spin of ^{76}Ga would be $I = 2^+$. Similarly, β decay studies of ^{78}Ga to ^{78}Ge made by Lewis *et al.* [113] and later the study led by Wohn *et al.* [114] on the decay of ^{78}Zn pointed to three possible ground-state spins for ^{78}Ga : $I = 2^-, 3^\pm$ or 4^-. Using the $\log ft$ values[2], they ruled out $I = \{2, 4\}$ as potential candidates, and were led to conclude that $I = 3^+$ was the ground state spin of ^{78}Ga.

[2] $\log ft$ is the *comparative half-life*. This concept appears in the Fermi theory of beta decay. For a brief introduction to this theory, see Krane [11].

The hyperfine structure measurements of the present work were able to resolve this matter, and it was found that the ground-state spin assignment of ^{76,78}Ga isotopes was $I = 2$. It is likely that this state has negative parity that arises from a coupling of $\pi\, f_{5/2} \otimes \nu\, (g_{9/2})^3$ as suggested for ^{72}Cu [131]. However, a firm parity assignment has to be made in connection with the decay scheme of these isotopes, and perhaps the schemes might also have to be reinterpreted. The data on the quadrupole moments also revealed that ^{76,78}Ga have to a good approximation the same underlying nuclear structure. The quadrupole moments for both isotopes show a relative decrease with respect to ^{72,74}Ga, which is an indication of a drop in collectivity as N approaches 50. It should be noted that the only existing shell model calculation on the moments of odd-odd gallium isotopes was carried out for ^{68}Ga, by Honma *et al.* [121] using the GXPF1 interaction. Regrettably, the sign of the quadrupole moment for ^{68}Ga is not known, but in absolute terms this interaction is able to indicate that ^{68}Ga is almost spherical($Q_{exp} = 0.0277 \pm 0.0014$ (b), $Q_{\mathrm{GXPF1}} = -0.013$ (b)).

8.4 The region landscape

The results presented in this work offer a complementary view to the existing body of knowledge which has been so far accumulated in the region. For instance, when the data on the nuclear moments are seen in connection with recent mass measurements that span $N = 28$ to $N = 50$ [132–134], as shown in Figure 8.5, it seems that $N = 40$ is still a valid sub-shell for gallium.

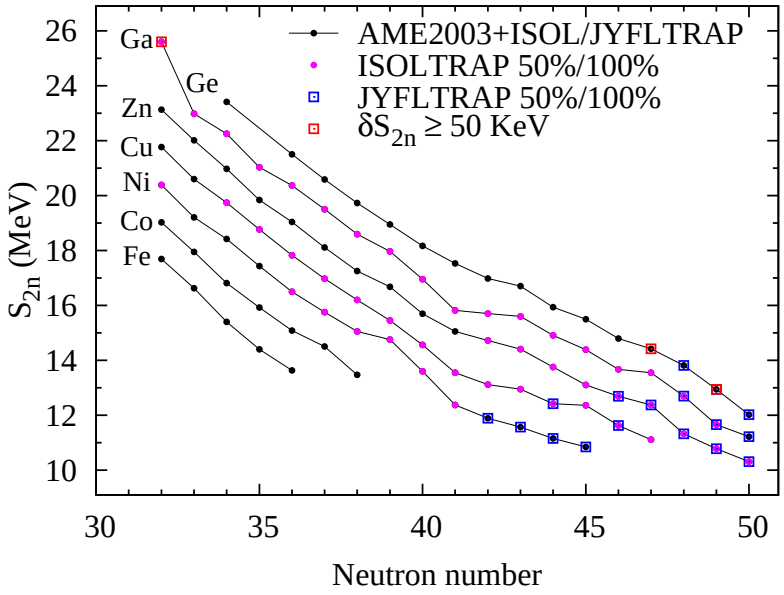

Figure 8.5: Two neutron separation energy (S_{2n}) close to $N = 40$. 100% means that the (S_{2n}) calculation was made with two new measured masses, whereas 50% means that the value used for one of the two masses was taken either from JYFLTRAP or ISOLTRAP measurements and the other value was taken from the AME2003 [135]. Courtesy of Ari Jokinen [136].

On the whole, in order to summarise the abundance of data available for this region, Figure 8.6 puts into perspective the recent achievements. Of the many outstanding features of this chart, it is important to stress the change in parity for the ground-state of Ge and Ga at $N = 41$, which indicates that the neutrons are occupying different harmonic oscillator shells. This is a manifestation of the fact that the fp shell is a rather transitional region, since there are strong single-particle and collective effects which coexist. Gallium in particular poses more difficulty for theoreticians since it has 3 protons outside the $Z = 28$ core. This thesis has produced a wealth of new data on spins and moments for neutron-rich gallium isotopes, where neutrons are filling the $g_{9/2}$ shell. It is hoped that these results will stimulate theoretical effort to extend the shell model into this region. Experimental results will also soon become available on changes of the mean-square charge radii, which is an additional measure of shell structure effects. The correlations between the radii and quadrupole deformations (Q_s) will be interesting to see. Though still scarce, more data are becoming available on the $B(E2)$ transition probabilities, which hopefully will help to complete the picture of the evolution of the nuclear structure in this region.

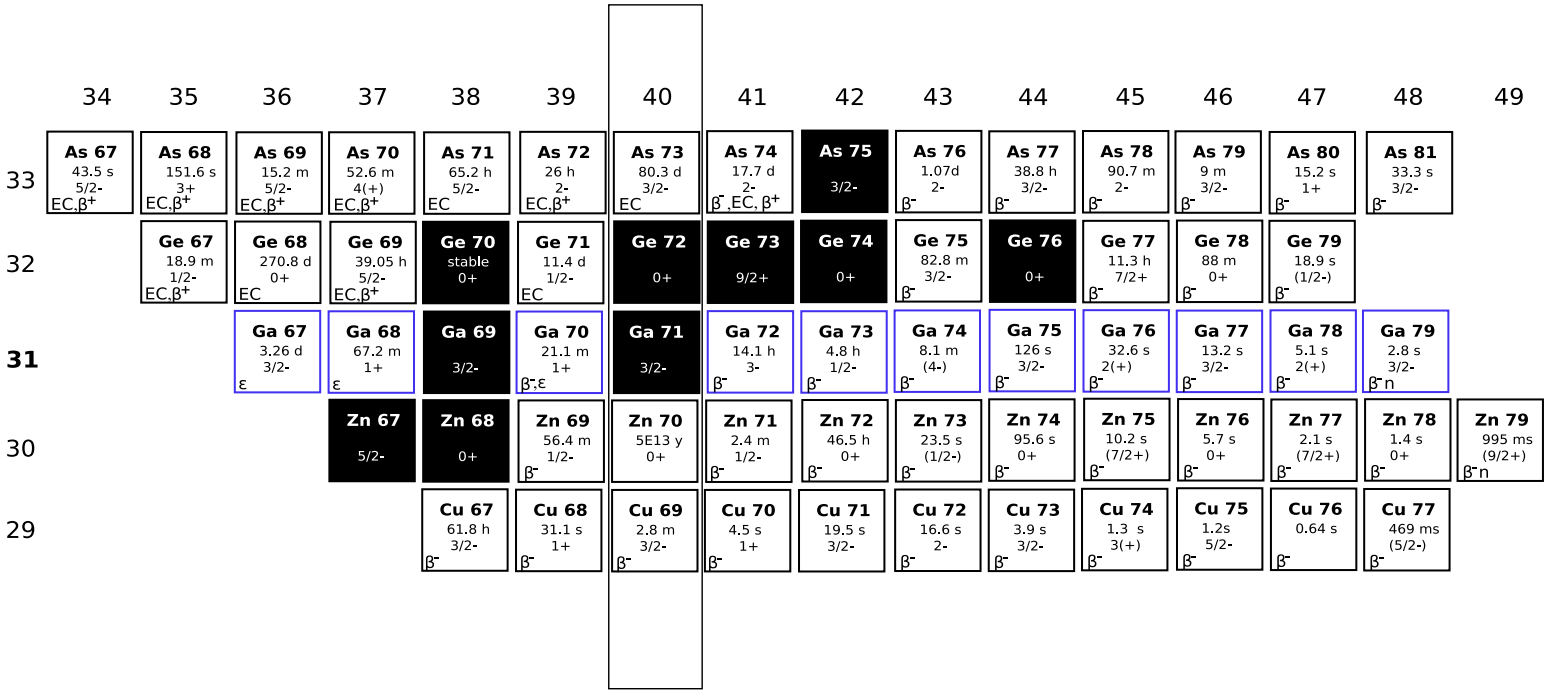

Figure 8.6: An overview of Ga and the neighbouring isotopes. Data taken from [137]. The values of the ground-state spin of $^{72-75}$Cu are based on unpublished values of recent collinear laser studies performed with ISCOOL.

CHAPTER 9

CONCLUSIONS AND OUTLOOK

In the course of this Ph.D. research, ISCOOL was commissioned off-line and on-line at CERN-ISOLDE. The results of the off-line commissioning showed that ISCOOL performed in compliance with its design specifications. The result of the on-line commissioning presented in this work constituted a first demonstration of bunched-beam spectroscopy at CERN-ISOLDE. The first on-line experiment using cooled and bunched beams at ISOLDE ran successfully in July 2008 on neutron-rich gallium isotopes. The programme set to measure the neutron-rich copper isotopes ran subsequently in the summer of 2008. The spectra obtained from these two experiments allowed several ground-state and isomeric spins and moments to be determined. In May 2009, the programme of measurements for the IS457 proposal was completed. From these recent measurements, it was possible to confirm the moments and ground-state spin assignments of the neutron-rich gallium isotopes obtained in the previous run, and presented in this thesis. In addition, these measurements spanned neutron-rich gallium isotopes beyond the $N = 50$ neutron magic number, adding new information on the spins and moments of ^{79,80,80m,81,82}Ga. From this dataset the isotope shifts of ^{69,71,72,73,74,75,76,77,78,79,80,80m,81,82}Ga will be reliably obtained. It is also planned that

the gallium programme will be extended to the neutron-deficient gallium isotopes, and an addendum to the original IS457 proposal is being drafted. In terms of ISOLDE machine development, in 2009 it is planned that the "kick" extraction of the ion bunches will be investigated with ISCOOL. In this method, the last three DC segments of the ion trap can be pulsed, improving the time focusing of the ion bunch. In the near future, ISCOOL will be of fundamental importance for the Manchester-led collinear resonance ionization spectroscopy beam line (CRIS), which is under construction at ISOLDE, and will allow experiments with unprecedented sensitivity and yet with the high resolution required for hyperfine structure studies in the optical region. Indeed, ISCOOL has opened new avenues to perform optical measurements across a much wider area of the nuclear landscape.

REFERENCES

[1] M. G. Mayer and J. H. D. Jensen. *Elementary Theory of Nuclear Shell Structure*. John Willey & Sons, 1955.

[2] J. Carlson and R. Schiavilla. Structure and dynamics of few-nucleon systems. *Rev. Mod. Phys.*, 70:743–841, 1998.

[3] H. Yukawa. Meson theory in its developments - nobel lecture, 1949.

[4] T. Hamada and I. D. Johnston. A potential model representation of two-nucleon data below 315 MeV. *Nucl. Phys.*, 34:382–403, 1962.

[5] R. Machleidt. The theory of nuclear forces: Is the never-ending story coming to an end? *Nucl. Phys. A*, 790:17–23, 2007.

[6] B. R. Martin and G. Shaw. *Particle Physics*. Willey, 1997.

[7] N. Ishii, S. Aoki, and T. Hatsuda. Nuclear Force from Lattice QCD. *Phys. Rev. Lett.*, 99:022001–1–4, 1995.

[8] M. G. Mayer. On Closed Shells in Nuclei.II. *Phys. Rev.*, 75:1969–1970, 1949.

[9] M. G. Mayer. Nuclear Configurations in the Spin-Orbit Coupling Model. I. Empirical Evidence. *Phys. Rev.*, 78:16–21, 1950.

[10] O. Haxel, J. H. D. Jensen, and H. E. Suess. On the "Magic Numbers" in Nuclear Structure. *Phys. Rev.*, 75:1766–38, 1949.

[11] K. S. Krane. *Introductory Nuclear Physics*. Wiley, 1988.

[12] K. Heyde. *The Nuclear Shell Model*. Springer-Verlag, 1994.

[13] A. Ozawa, T. Kobayashi, T. Suzuki, K. Yoshida, and I. Tanihata. New magic number, N= 16, near the neutron drip line. *Phys. Rev. Lett.*, 84(24):5493–5495, 2000.

[14] D. Guillemaud-Mueller, C. Detraz, M. Langevin, F. Naulin, M. de Saint-Simon, C. Thibault, F. Touchard, and M. Epherre. β-decay schemes of very neutron-rich sodium isotopes and their descendants. *Nucl. Phys. A*, 426:37–76, 1984.

[15] T. Motobayashi, Y. Ikeda, K. Ieki, M. Inoue, N. Iwasa, T. Kikuchi, M. Kurokawa, S. Moriya, S. Ogawa, H. Murakami, S. Shimoura, Y. Yanagisawa, T. Nakamura, Y. Watanabe, M. Ishihara, T. Teranishi, H. Okuno, and R. F. Casten. Large deformation of the very neutron-rich nucleus ^{32}Mg from intermediate-energy Coulomb excitation. *Phys. Lett. B*, 346:9–14, 1995.

[16] H. Simon, D. Aleksandrov, T. Aumann, L. Axelsson, T. Baumann, M. J. G. Borge, L. V. Chulkov, R. Collatz, J. Cub, W. Dostal, B. Eberlein, Th. W. Elze,

H. Emling, H. Geissel, A. Grünschloss, M. Hellström, J. Holeczek, R. Holzmann, B. Jonson, J. V. Kratz, G. Kraus, R. Kulessa, Y. Leifels, A. Leistenschneider, T. Leth, I. Mukha, and G. Münzenberg. Direct experimental evidence for strong admixture of different parity states in ^{11}Li. *Phys. Rev. Lett.*, 83:496–499, 1999.

[17] H. Keller, R. Anne, D. Bazin, R. Bimbot, J. G. M. Borge, J. M. Corre, S. Dogny, H. Emling, D. Guillemaud-Mueller, P. G. Hansen, P. Hornshoj, F. Humbert, P. Jensen, B. Jonson, M. Lewitowicz, A. C. Mueller, R. Neugart, T. Nilsson, G. Nyman, F. Pougheon, M. G. Saint-Laurent, G. Schrieder, O. Sorlin, O. Tengblad, and K. W. Rolander. Search for forbidden β-decays of the drip line nucleus ^{12}Be. *Z. Phys. A*, 348:61–62, 1994.

[18] N. J. Stone. Table of nuclear magnetic dipole and electric quadrupole moments. *At. Data Nucl. Data Tables*, 90:75–176, 2005.

[19] J. Billowes and P. Campbell. High-resolution laser spectroscopy for the study of nuclear sizes and shapes. *J. Physics G*, 21:707–739, 1995.

[20] E. W. Otten. *Treatise on Heavy-Ion Science*, chapter 7. Plenum Press, 1989.

[21] H.-J. Kluge and W. Nörtershäuser. Lasers for nuclear physics. *Spectrochimica Acta Part B*, 58:1031–1045, 2003.

[22] K. T. Flanagan. Private communication, 2009.

[23] P. K. Ghosh. *Ion Traps*. Oxford Universtity Press, 1995.

[24] D. Leibfried, R. Blatt, C. Monroe, and D. Wineland. Quantum dynamics of single trapped ions. *Reviews of Modern Physics*, 75:281–323, 2003.

[25] A. Nieminen, P. Campbell, J. Billowes, D. H. Forest, J. A. R. Griffith, J. Huikari, A. Jokinen, I. D. Moore, R. Moore, G. Tungate, and J. Äystö. On-Line Ion Cooling and Bunching for Collinear Laser Spectroscopy. *Phys. Rev. Lett.*, 88:094801–1:4, 2002.

[26] B. H. Bransden and C. J. Joachain. *Physics of Atoms and Molecules*. Longman Publishing, 1983.

[27] W. Pauli. *Writings on Physics and Philosophy*. Springer, 1994.

[28] G. W. F. Drake. *Springer Handbook of Atomic, Molecular, and Optical Physics*. Springer, 2005.

[29] G. K. Woodgate. *Elementary atomic structure*. Springer, 1970.

[30] P. C. Magnante and H. H. Stroke. Isotope shift between ^{209}Bi and 6.3-day ^{206}Bi. *J. Opt. Soc. Am.*, 59:836–841, 1969.

[31] S. Büttgenbach. Magnetic Hyperfine Anomalies. *Hyperfine Interact.*, 20:1–64, 1984.

[32] H. H. Stroke, R. J. Blin-Stoyle, and Jaccarino V. Configuration Mixing and the Effects of Distributed Nuclear Magnetization on Hyperfine Structure in odd-A Nuclei. *Phys. Rev.*, 123:1326–1348, 1961.

[33] D. S. Hughes and C. Eckart. The Effect of the Motion of the Nucleus on the Spectra of Li I and Li II. *Phys. Rev.*, 36(4):694–698, 1930.

[34] K. Heilig and A. Steudel. Changes in mean-square nuclear charge radii from optical isotope shifts. *At. Data Nucl. Data Tables*, 14:613–638, 1974.

[35] L. D. Landau and E. M. Lifshitz. *Quantum Mechanics*. Pergamon Press, 1977.

[36] G. Fricke, C. Bernhardt, K. Heilig, L. A. Schaller, L. Schellenberg, E. B. Shera, and De Jager, C. W. Nuclear ground state charge radii from electromagnetic interactions. *At. Data Nucl. Data Tables*, 60:177–285, 1995.

[37] E. C. Seltzer. K x-ray isotope shifts. *Phys. Rev.*, 188:1916–1919, 1969.

[38] G. Torbohm, G. Fricke, and A. Rosén. State-dependent volume isotope shifts of low-lying states of group-iia and -iib elements. *Phys. Rev. A*, 31:2038–2053, 1985.

[39] J. H. M. Neijzen and A. Dönszelmann. Hyperfine structure and isotope shift measuremets in neutral gallium and indium with a pulsed dye laser. *Physica*, 98C:235–241, 1980.

[40] H. G. Kuhn. *Atomic Spectra*. Longmans, 1963.

[41] C. J. Foot. *Atomic Physics*. Oxford Press, 2005.

[42] W. Demtröder. *Laser Spectroscopy*. Springer, 2003.

[43] E. Otten. *Investigation of Short-Lived Isotopes by Laser Spectroscopy*. Harwood, 1989.

[44] S. L. Kaufman. High-resolution laser spectroscopy in fast beams. *Opt. Comm.*, 17:309, 1976.

[45] W. H. Wing, G. A. Ruff, W. E. Lamb Jr., and J. J. Spezeski. Observation of the Infrared Spectrum of the Hydrogen Molecular Ion HD^+. *Phy. Rev. Lett.*, 36:1488, 1976.

[46] P. Campbell. *Nuclear Ground State Properties of Stable and Radioactive Isotopes by Ultraviolet Laser Spectroscopy*. PhD thesis, University of Manchester, 1994.

[47] P. F. Moulton. Spectroscopic and laser characteristics of Ti:$A1_2O_3$. *J. Opt. Soc. Am. B*, 3:125–133, 1995.

[48] G. Holtom and O. Teschke. Design of a Bifefringent Filter for High-Power Dye Lasers. *IEEE J. Quantum Electron.*, QE-10:577–579, 1974.

[49] W. Koechner. *Solid-State Laser Engineering*. Springer, 2006.

[50] Spectra-Physics. *WAVETRAIN® User's Manual*, 2002.

[51] E. D. Black. An introduction to Pound-Drever-Hall laser frequency stabilization. *Am. J. Phys.*, 68:79–87, 2000.

[52] Jørgen Koch. A Device Producing Ion Beams Homogeneous as to Mass and Energy. *Phys. Rev.*, 69:238, 1946.

[53] J. Äystö. CERN's longest serving experimental facility. *Phys. Rep.*, 403-404:459–469, 2004.

[54] R. W. Geithner. *Nuclear Moments and Differences in Mean Square Charge Radii of Short-Lived Neon Isotopes by Collinear Laser Spectroscopy*. PhD thesis, University of Mainz, 2002.

[55] B. A. Marsh. *In-Source Laser Resonance Ionization at ISOL Facilities*. PhD thesis, University of Manchester, 2007.

[56] M. Petersson. A Monte Carlo method for the simulation of buffer gas cooling inside a radio frequency quadrupole. Master's thesis, Linköping University, IFM, 2002.

[57] I. Podadera. *New developments on preparation of cooled and bunched radioactive ion beams at ISOL - facilities : The ISCOOL project and The rotating wall cooling*. PhD thesis, Universitat Politecnica de Catalunya, 2006.

[58] P. H. Dawson. *Quadrupole Mass Spectrometry and its applications*. Elsevier, 1976.

[59] M. Abramowitz and I.A Stegun. *Handbook of Mathematical Functions*. Dover, 1970.

[60] B. van der Pol and M. J. O. Strutt. On the Stability of the Solutions of Mathieu's Equation. *Philos. Mag.*, 5:18–38, 1928.

[61] M. Drewsen and A. Brøner. Harmonic linear Paul trap: Stability diagram and effective potentials. *Phys. Rev. A*, 62:045401, 2000.

[62] A. Nieminen. *Manipulation of low energy radioactive ion beams with and RFQ cooler; Application to collinear laser spectroscopy*. PhD thesis, University of Jyväskylä, 2002.

[63] A. M. G. Dezfuli. *Injection, Cooling and Extraction of Ions from a Very Large Paul Trap*. PhD thesis, McGill University, 1996.

[64] H. Wollnik. *Optics of Charged Particles*. Academic Press, 1987.

[65] F. Wenader, J. Lettry, and M. Lindroos. Tranverse emittance investigation of the isolde target-ion sources. *Nucl. Instrum. Methods Phys. Res. B*, 204:261–266, 2003.

[66] C. W. V. Fong. *Phase Space Dynamics in a Linear RFQ Trap for Time-of-Flight Mass Spectrometry*. PhD thesis, McGill University, 2001.

[67] A. J. Lichtenberg. *Phase-Space Dynamics of Particles*. John Wiley Sons, 1969.

[68] H. Goldstein. *Classical Mechanics*. Addison-Wesley, 1980.

[69] T. Kim. *Buffer Gas Cooling of Ions in a Radio Frequency Quadrupole Ion Guide*. PhD thesis, McGill University, 1997.

[70] W. M. Itano, J. C. Berquist, J. J. Bollinger, and Wineland D. J. Cooling methods in ion traps. *Physica Scripta*, T59:106–120, 1995.

[71] F. G. Major and H. G. Dehmelt. Exchange-Collision Technique for the rf Spectroscopy of Stored Ions. *Phy. Rev.*, 170:91–107, 1968.

[72] D. J. Douglas and J. B. French. Collisional focusing effects in radio frequency quadrupoles. *J. Am. Soc. Mass Spectrom.*, 3:398–408, 1992.

[73] A. Jokinen, M. Lindroos, E. Molin, M. Petersson, and The ISOLDE Collaboration. Rfq-cooler for low-energy radioactive ions at isolde. *Nucl. Instrum. Methods Phys. Res. B*, 204:86–89, 2003.

[74] L. A. Viehland and E. A. Mason. Transport properties of gaseous ions over a wide energy range, iv. *Atomic Data and Nuclear Data Tables*, 60:37–95, 1995.

[75] M. D. Lunney and R. B. Moore. Cooling of mass-separated beams using a radiofrequency quadrupole ion guide. *Int. J. Mass Spec.*, 190/191:153–160, 1999.

[76] H. Franberg, P. Delahaye, J. Billowes, K. Blaum, R. Catherall, F. Duval, O. Gianfrancesco, T. Giles, A. Jokinen, M. Lindroos, D. Lunney, E. Mané, and I. Podadera. Off-line commisioning of the ISOLDE cooler. *Nucl. Instrum. Meth. Phys. Res. B*, 266:4502–4, 2008.

[77] G. Huchet. Mesures d′émittance d′un faisceau d′ions intense séparé en masse. Master's thesis, Université de Paris Sud (XI), 2002.

[78] NTG Neue Technologien. *Profile- and Emittance-Analyzer Manual*, 2001.

[79] HeatWave Labs. *TB-118 Aluminosilicate Ion Sources*, 2002.

[80] D. A. Dahl. *SIMION 3D Version* 7.0 *User's Manual*, 2000.

[81] J. Äystö, A. Jokinen, and The EXOTRAPS Collaboration. Ion bean coolers in nuclear physics. *J. Phys. B*, 36:573–584, 2003.

[82] K. Rudolph. *NG-VFO400/200-1200 sinus oscillator, version 1.3*, 2007.

[83] T. Tallinen. The ISCOOL test bench control system. Technical report, CERN, 2005.

[84] G. Jesse. Chemical analysis by SEM/EDX of an 0.250 Ion Source Na - "ISCOOL" RFQ cooler for ISOLDE, 2006.

[85] E. Mané, J. Billowes, K. Blaum, P. Campbell, B. Cheal, P. Delahaye, K. T. Flanagan, D. H. Forest, H. Franberg, C. Geppert, T. Giles, A. Jokinen, M. Kowalska, R. Neugart, G. Neyens, W. Nörtershäuser, I. Podadera, G. Tungate, P. Vingerhoets, and D. T. Yordanov. An ion cooler-buncher for high sensitivity collinear laser spectroscopy at ISOLDE. *Eur. Phys. J. A*, DOI 10.1140/epja/i2009-10828-0, 2009.

[86] M. Kowalska. *Ground state properties of neutron-rich Mg isotopes - the "island of inversion" studied with laser and* β*-NMR spectroscopy*. PhD thesis, University of Mainz, 2006.

[87] D. Skoog, F. J. Holler, and T. A. Nieman. *Principles of Instrumental Analysis*. Saunders, 1997.

[88] F. Touchard, P. Guimbal, S. Büttbenbach, R. Klapisch, M. De Saint Simon, J. M. Serre, and C. Thibault. Isotope shifts and hyperfine structure of $^{38-47}$K by laser spectroscopy. *Phys. Lett. B*, 108:169–171, 1982.

[89] R. Brun and F. Rademakers. ROOT - An object oriented data analysis framework. *Nucl. Instrum. Meth. Phys. Res. A*, 389:81–86, 1987.

[90] S. Falke, E. Tiemann, C. Listdat, H. Schnatz, and G. Grosche. Transition frequencies of the *D* lines of ^{39}K, ^{40}K, and ^{41}K measured with a femtosecond laser frequency comb. *Phys. Rev. A*, 74:032503–1:9, 2006.

[91] S. D. Bruce, J. Higinbotham, I. Marshall, and Beswick P. H. An Analytical Derivation of a Popular Approximation of the Voigt Function for Quantification of NMR Spectra. *J. Mag. Res.*, 142:57–63, 2000.

[92] V. Kellö and A. J. Sadlej. The quadrupole moment of the ^{39}K and ^{41}K nuclei from microwave data for KF and KCl. *Chem. Rev. Lett.*, 292:403–410, 1998.

[93] G. Neyens. Ground-state properties of K-isotopes from laser and β-NMR spectroscopy. *CERN INTC*, 003:P254, 2009.

[94] J. Billowes, K. Blaum, P. Campbell, B. Cheal, P. Delahaye, K. T. Flanagan, D. H. Forest, A. Jokinen, P. Lievens, E. Mané, I. D. Moore, G. Neyens, R. Neugart,

H. H. Stroke, G. Tungate, D. T. Yordanov, J. Äystö, and the ISOLDE collaboration. Laser spectroscopy of gallium isotopes using the ISCOOL RFQ cooler. *CERN-INTC*, page 224, 2007.

[95] U. Köster. *Ausbeuten und Spektroskopie radioaktiver Isotope bei LOHENGRIN und ISOLDE*. PhD thesis, Technischen Universität München, 1999.

[96] U. Köster. Intense radioactive-ion beams produced with the ISOL method. *Eur. Phys. J. A*, 15:255–263, 2002.

[97] U. Köster, T. Behrens, C. Clausen, P. Delahaye, V. N. Fedoseyev, L. M. Fraile, R. Gernhäuser, T. J. Giles, A. Ionan, T. kröll, H. Mach, B. Marsh, M. Sliverstov, T. Sieber, E. Siesling, E. Tengborn, F. Wenader, and J. Van de Walle. ISOLDE beams of neutron-rich zin isotopes: yields, release, decay spectroscopy. *AIP Conf. Proc.*, 798:315–323, 2005.

[98] C. H. Corliss and W. R. Bozman. Experimental transition probabilities for spectral lines of seventy elements. Derived from the nbs tables of spectral-line intensities. *Natl. Bur. Stand. Monogr*, 53:III – XVII, 1962.

[99] T. Bezboruah, K. Boruah, and P. K. Boruah. An improved resistive amplification network for fast timing photomultiplier tubes. *Measurement*, 37:131–4, 2005.

[100] V. J. Ehlers, Y. Kabasakal, H. A. Shugart, and O. Tezer. Hyperfine structure of ^{67}Ga and ^{72}Ga. *Phys. Rev.*, 176:25–42, 1968.

[101] D. Cline and M. S. Lesser. Error estimation in non-linear least square anaylsis of data. *Nucl. Instrum. Methods*, 82:291–293, 1970.

[102] P. R. Bevington and D. K. Robinson. *Data reduction and error anaylsis for the physical sciences*. McGrall-Hill, 2003.

[103] O. M. Maragò, B. Fazio, P. G. Gucciardi, and E. Arimondo. Atomic gallium laser spectroscopy with violet/blue diode lasers. *Appl. Phys. B*, 77:809–815, 2003.

[104] R. J. Barlow. *Statistics: a guide to the use of statistical methods in the physical sciences*. Wiley, 1986.

[105] C. Ythier, R. K. Girgis, R. A. Ricci, and R. Van Lieshout. The decay of ^{73}Ga. *Nuc. Phys.*, 9:108–115, 1958.

[106] C. Ythier, W. Schoo, B. L. Schram, H. L. Polak, R. K. Girgis, R. A. Ricci, and R. Van Lieshout. On the decay of ^{74}Ga. *Physica*, 25:694–702, 1959.

[107] E. Eichler, G. D. O'Kelley, R. L. Robinson, J. A. Marinsky, and N. R. Johnson. Nuclear levels of ^{74}Ge. *Nuc. Phys.*, 36:425–644, 1962.

[108] Riisager. K. Private communication, 2009.

[109] M. C. Chacko, L. Dorikens-Vanpraet, and M. Dorikens. The decay of ^{75}Ga to levels in ^{75}Ge. *Z. Phys. A*, 267:359–365, 1974.

[110] G. Rotbard, G. LaRana, M. Vergnes, G. Berrier, J. Kalifa, F. Guilbault, and R. Tamisier. ^{70,72,74,76}Ge(d, ^{3}He)^{69,71,73,75}Ga reactions at 26 MeV. *Phys. Rev. C*, 18:86–95, 1978.

[111] D. C. Camp, D. R. Fielder, and B. P. Foster. Energy levels in ^{74}Ge from the decay of ^{74}Ga. *Nuc. Phys. A*, 163:145–160, 1971.

[112] B. Ekström, B. Fogelberg, P. Hoff, E. Lund, and A. Sangariyavanish. Decay Properties of $^{75-80}$Zn and Q_β-Values of Neutron-Rich Zn and Ga Isotopes. *Physica Scripta*, 34:614–623, 1986.

[113] D. A. Lewis, John C. Hill, F. K. Wohn, and M. L. Gartner. Decay of mass-separated ^{78}Ga to levels in even-even ^{78}Ge. *Phys. Rev. C*, 22:2178–2185, 1980.

[114] F. K. Wohn, John C. Hill, and D. A. Lewis. Decay of mass-separated ^{78}Zn. *Phys. Rev. C*, 22:2547–2554, 1980.

[115] P. Hoff and B. Fogelberg. Properties of strongly neutron-rich isotopes of germanium and arsenic. *Nuc. Phys. A*, 368:210–236, 1981.

[116] D. T. Yordanov. *From ^{27}Mg to ^{33}Mg: transition to the Island of inversion* . PhD thesis, University of Leuven, 2007.

[117] I. I. Sobel'man. *Introduction to the Theory of Atomic Spectra*. Pergamon, 1972.

[118] B. Castel and I. S. Towner. *Modern Theory of Nuclear Moments*. Clarendon Press, 1990.

[119] P. J. Mohr, B. N. Taylor, and D. B. Newell. CODATA recommended values of the fundamental physical constants: 2006. *Rev. Mod. Phys.*, 80(2):633, 2008.

[120] N. J. Stone, K. van Esbroeck, J. Rikovska Stone, M. Honma, T. Giles, M. Veskovic, G. White, A. Wöhr, V. I. Mishin, V. N. Fedoseyev, U. Köster, P. F. Mantica, and W. B. Walters. Nuclear dipole moment of ^{71}Cu from online beta-NMR measurements. *Phys. Rev. C*, 77:014315–1:3, 2008.

[121] M. Honma, T. Otsuka, B. A. Brown, and T. Mizusaki. New effective interaction for pf-shell nuclei and its implications for the stability of the $N = Z = 28$ closed core. *Phys. Rev. C*, 69:034335–1:33, 2004.

[122] A. Bohr and B. R. Mottelson. *Nuclear Structure - Volume 1: Single-Particle Motion*. World Scientific, 1998.

[123] I. Stefanescu, W. B. Walters, R. V. F. Janssens, R. Broda, M. P. Carpenter, C. J. Chiara, B. Fornal, B. P. Kay, F. Kondev, W. Krolas, T. Lauritsen, C. J. Lister, E. A. McCuthan, T. Pawlat, D. Seweryniak, J. R. Stone, N. Stone, J. Wrzesinski, and S. Zhu. Identification of the $g_{9/2}$ proton-band in the neutron-rich ^{71,73,75,77}Ga populated in deep-inelastic reactions. *Submitted to Phys. Rev. C*, 2009.

[124] N. Yoshinaga, K. Higashiyama, and P. H. Regan. High-spin structure of neutron-rich Se, As, Ge, and Ga isotopes. *Phys. Rev. C*, 78:044320–1–12, 2008.

[125] K. Heyde. *Basic Ideas and Conceps in Nuclear Physics*. Institute of Physics Publishing, 1972.

[126] L. W. Nordheim. β-Decay and the Nuclear Shell Model. *Phys. Rev.*, 78:294, 1950.

[127] M. H. Brennan and A. M. Bernstein. jj Coupling Model in Odd-Odd Nuclei. *Phys. Rev.*, 120:927–933, 1960.

[128] J. van Klinken and L. M. Taff. Isomeric state in ^{74}Ga. *Phys. Rev. C*, 9:2252–2260, 1974.

[129] C. Schwartz. The Ground States of Odd-Odd Nuclei. *Phys. Rev.*, 94:95–99, 1954.

[130] D. C. Camp and B. P. Foster. Energy levels in ^{76}Ge from the decay of ^{76}Ga. *Nuc. Phys. A*, 177:401–417, 1971.

[131] J.-C. Thomas, H. De Witte, M. Gorska, M. Huyse, K. Kruglov, Y. Kudryavtsev, D. Pauwels, N. V. S. V. Prasad, K. Van de Vel, P. Van Duppen, J. Van Roosbroeck, S. Franchoo, J. Cederkall, H. O. U. Fynbo, U. Georg, O. Jonsson, U. Köster, L. Weissman, W. F. Mueller, V. N. Fedosseev, V. I. Mishin, D. Fedorov, A. De Maesschalck, and N. A. Smirnova. β-decay properties of ^{72}Ni and ^{72}Cu. *Phys. Rev. C*, 74:054309–1:16, 2006.

[132] C. Guénaut, G. Audi, D. Beck, K. Blaum, G. Bollen, P. Delahaye, F. Herfurth, A. Kellerbauer, H.-J. Kluge, D. Lunney, S. Schwarz, L. Schwikhard, and

C. Yazidjian. Is $N = 40$ magic? An analysis of ISOLTRAP mass measurements. *Eur. Phys. J. A*, 25:33–34, 2005.

[133] S. Rahaman, J. Hakala, V.-V. Elomaa, T. Eronen, U. Hager, A. Jokinen, A. Kankainen, I. D. Moore, H. Penttilä, S. Rinta-Antila, J. Rissanen, A. Saastamoinen, C. Weber, and J. Äystö. Masses of neutron-rich Ni and Cu isotopes and the shell closure at $Z = 28$, $N = 40$. *Eur. Phys. J. A*, 34:5–9, 2007.

[134] J. Hakala, S. Rahaman, V.-V. Elomaa, T. Eronen, U. Hager, A. Jokinen, A. Kankainen, I. D. Moore, H. Penttilä, S. Rinta-Antila, J. Rissanen, A. Saastamoinen, T. Sonoda, C. Weber, and J. Äystö. Evolution of the $N = 50$ Shell Gap Energy towards ^{78}Ni. *Phys. Rev. Lett.*, 101:052502, 2008.

[135] G. Audi, A. H. Wapstra, and C. Thibault. The AME2003 atomic mass evaluation. II. Tables, graphs and references. *Nucl. Phys. A*, 729:337–676, 2003.

[136] A. Jokinen. Private communication, 2008.

[137] R. B. Firestone. *Table of Isotopes*. Wiley, 1996.